Plasma speed optimization for improved tokamak plasma confinement

Anna Krupka

INSTITUT POLYTECHNIQUE DE PARIS

NNT : 2024IPPAX092

Thèse de doctorat

Plasma speed optimization for improved tokamak plasma confinement

Thèse de doctorat de l'Institut Polytechnique de Paris
préparée à l'École polytechnique

École doctorale n°626 École doctorale de l'Institut Polytechnique de Paris (EDIPP)
Spécialité de doctorat : Optique, laser et plasma

Thèse présentée et soutenue à Palaiseau, le 22 Novembre 2024, par

ANNA KRUPKA

Composition du Jury :

Xavier Leoncini Professeur, Aix-Marseille Université	Président
Alain Ghizzo Professeur, Université de Lorraine	Rapporteur
Alessandro Biancalani - absent lors de la soutenance Professeur, Ecole Supérieure d'Ingénieurs Léonard de Vinci	Rapporteur
Wouter Bos Directeur de Recherche, École Centrale de Lyon	Examinateur
Jean-Marcel Rax Professeur, Université Paris-Saclay	Examinateur
Luca Guazzotto Professor, Auburn University	Examinateur
Marie-Christine Firpo Directrice de Recherche, École polytechnique	Directrice de thèse

Institut Polytechnique de Paris
École doctorale №626 Institut Polytechnique de Paris (IPP)
Laboratoire de Physique des Plasmas (LPP)

Plasma speed optimization for improved tokamak plasma confinement

Par Anna KRUPKA

Spécialité de doctorat : Optique, laser et plasma

Dirigée par Marie-Christine FIRPO

Thèse présentée et soutenue à Palaiseau, le 22 Novembre 2024

Composition du Jury :

Prof. Xavier LEONCINI Président	Aix-Marseille Université
Prof. Alain GHIZZO Rapporteur	Université de Lorraine
Prof. Alessandro BIANCALANI Rapporteur	École Supérieure d'Ingénieurs Léonard de Vinci
Dr. Wouter BOS Examinateur	École Centrale de Lyon
Prof. Jean-Marcel RAX Examinateur	Université Paris-Saclay
Prof. Luca GUAZZOTTO Examinateur	Auburn University
Dr. Marie-Christine FIRPO Directrice de thèse	École polytechnique

Optimisation de la vitesse du plasma pour l'amélioration du confinement des tokamaks

Résumé : Pour rendre performants les réacteurs à fusion par confinement magnétique, il est impératif de maximiser le confinement du plasma. Cela représente un enjeu crucial dans le développement des futurs tokamaks, qui sont envisagés comme une solution pour produire une énergie propre et quasi illimitée. En effet, un bon confinement permet de maintenir les températures et densités élevées nécessaires pour que les réactions de fusion se produisent de manière efficace. L'un des aspects fondamentaux pour atteindre cet objectif est la maîtrise de la dynamique du plasma, notamment la possibilité de jouer sur la vitesse du plasma. Une rotation contrôlée du plasma peut non seulement stabiliser les instabilités magnétohydrodynamiques (MHD), mais également réduire la turbulence, améliorant ainsi le confinement et, par conséquent, les performances globales du réacteur.

Dans cette perspective, comprendre les mécanismes qui permettent de mettre en rotation un plasma dans un tokamak est un défi de première importance. Cela implique de considérer les interactions complexes entre les forces magnétiques, électriques, visqueuses et inertielle. Pour répondre à cet enjeu, il est nécessaire de modéliser le comportement du plasma dans des conditions réalistes. Les modèles basés sur la magnétohydrodynamique visco-résistive offrent un cadre adapté pour étudier ces phénomènes, notamment en intégrant le terme non-linéaire $(\boldsymbol{v} \cdot \nabla)\boldsymbol{v}$ dans l'équation de Navier-Stokes stationnaire. Ce terme, qui représente les effets inertiels, joue un rôle crucial dans la description des états stationnaires du plasma en rotation.

Une des particularités des tokamaks est leur géométrie toroïdale complexe, qui nécessite une modélisation sophistiquée pour capturer les détails de la dynamique du plasma. En utilisant le logiciel FreeFem++, qui est un outil open-source basé sur la méthode des éléments finis, il a été possible de résoudre numériquement les équations MHD dans des configurations réalistes de tokamaks comme celles du JET (Joint European Torus). Ce type de simulation offre une plateforme puissante pour explorer les états stationnaires axisymétriques du plasma et étudier leur dépendance aux paramètres physiques tels que la viscosité ν, la résistivité η, et le champ magnétique.

Dans ce travail, nous nous sommes concentrés sur un modèle MHD visco-résistif avec des coefficients constants de résistivité et de viscosité, afin de mieux comprendre les mécanismes fondamentaux influençant la rotation du plasma. Une des découvertes principales de cette étude est que la vitesse moyenne quadratique du plasma dépend de manière critique du nombre de Hartmann, défini comme $H \equiv (\eta\nu)^{-1/2}$. Lorsque le terme inertiel est négligeable, cette vitesse suit une loi en $\eta f(H)$, où $f(H)$ présente un comportement en loi de puissance. Plus précisément, dans la limite des faibles nombres de Hartmann ($H \ll 1$), $f(H)$ suit une dépendance proportionnelle à H, tandis que pour les grands nombres

de Hartmann ($H \gg 1$), une dépendance asymptotique en $H^{1/4}$ est observée. Ces résultats théoriques sont cohérents avec les simulations numériques, renforçant ainsi la validité du modèle proposé.

Par ailleurs, le profil de pression dans le plasma est gouverné par une équation de Poisson. Dans ce contexte, nous avons démontré que l'hypothèse simplificatrice selon laquelle la densité de courant toroïdale découle uniquement de la loi d'Ohm en réponse à un champ électrique toroïdal uniforme et constant dans le temps ne permet pas de reproduire des profils de pression réalistes. Cette simplification conduit à des écarts significatifs par rapport aux observations expérimentales. Pour surmonter cette limitation, nous avons introduit des termes de courant non inductifs supplémentaires, représentant des mécanismes tels que l'injection de faisceaux neutres. Ces termes modifient le courant toroïdal et améliorent considérablement les profils de pression obtenus par les simulations numériques.

Une autre découverte importante concerne l'impact de ces entraînements de courant non inductifs sur les profils de vitesse du plasma. Dans la plupart des cas étudiés, l'effet sur la rotation est modéré. Cependant, lorsque ces entraînements induisent des inversions dans la densité de courant toroïdal totale, des phénomènes plus complexes apparaissent. En particulier, des surfaces de flux non imbriquées avec des séparatrices internes peuvent se former, modifiant la topologie magnétique et influençant les propriétés du confinement du plasma.

Enfin, nous avons exploré l'effet de profils de densité de courant imposés sur la dynamique du plasma. Cette étude a révélé l'existence d'un nouveau régime asymptotique où les vitesses toroïdales et poloïdales croissent proportionnellement à H^2, soulignant ainsi la richesse des comportements dynamiques possibles dans un plasma de tokamak. Ce second régime offre des perspectives intéressantes pour le contrôle de la rotation et pourrait avoir des implications significatives pour le design des futurs réacteurs à fusion.

Ce travail ouvre la voie à de nouvelles recherches pour optimiser les performances des tokamaks en régime stationnaire. Les résultats obtenus soulignent l'importance de considérer les effets inertiels et les contributions non inductives au courant toroïdal dans les modèles de plasma. De plus, ils mettent en évidence la nécessité d'approches numériques avancées pour explorer les comportements complexes des plasmas confinés magnétiquement. Ces efforts contribueront à établir les bases scientifiques et techniques pour la conception de réacteurs à fusion opérationnels, capables de fournir une énergie sûre et durable à grande échelle.

Plasma speed optimization for improved tokamak plasma confinement

Abstract: Maximizing plasma confinement is essential to the performance of future magnetic fusion reactors. Playing with plasma speed can be a way to stabilize possible instabilities and control turbulence with a very beneficial impact on fusion yield. It is essential to understand how a tokamak plasma can be rotated.

Ideally, the tokamak should work in a stationary state as a fusion reactor. It is, therefore, reasonable to determine the steady states of a tokamak plasma in full generality without imposing the nullity of the plasma velocity field. In the visco-resistive magnetohydrodynamics (MHD) framework, this amounts in particular to retaining the non-linear term $(\boldsymbol{v} \cdot \nabla)\boldsymbol{v}$ in the stationary Navier-Stokes equation. Using the FreeFem++ open-source software for solving partial differential equations using the finite element method, we numerically determined the axisymmetric stationary states of a tokamak plasma in realistic JET parameters.

This thesis shows that the plasma velocity root-mean-square behaves as $\eta f(H)$ as long as the inertial term remains negligible, where H stands for the Hartmann number $H \equiv (\eta\nu)^{-1/2}$, and that $f(H)$ exhibits power-law behaviours in the limits $H \ll 1$ and $H \gg 1$. In the latter limit, we establish that $f(H)$ scales as $H^{1/4}$, which is consistent with numerical results. Additionally, this work establishes Poisson's equation governing the pressure profile. It is shown that the simplifying assumption of a toroidal current density component arising solely from Ohm's law in response to a time-independent, curl-free toroidal electric field fails to produce realistic pressure levels. To overcome this, we introduce additional non-inductive current drives, comparable to those from neutral beam injection, modeled as modifications to the toroidal current. The new model is validated using numerical simulations, showing significant pressure profile improvements. For the examples considered, the effect of these current drives on the velocity profiles is moderate except in the case where the drives induce some reversals in the total toroidal current density, producing non-nested flux surfaces with internal separatrices. Finally, the effect of fixed current density profiles is examined, revealing a new second regime, where toroidal and poloidal velocities scale with Hartmann number as H^2, yielding higher plasma rotation.

I must not fear. Fear is the mind-killer. Fear is the little-death that brings total obliteration. I will face my fear. I will permit it to pass over me and through me. And when it has gone past I will turn the inner eye to see its path. Where the fear has gone there will be nothing. Only I will remain.

Frank Herbert, Dune

Aknowledgements

With the end of my PhD journey, I want to express my gratitude to all the people who have supported me along the way. This thesis would not have been possible without the help and encouragement of many people, and I am deeply thankful for their contributions.

First, I would like to express my sincere gratitude to the reviewers, Alain Ghizzo and Alessandro Biancalani, for their time and effort in reviewing this thesis. I am also deeply grateful to the jury members Xavier Leoncini, Wouter Bos, Luca Guazzotto, and Jean-Marcel Rax for taking the time to participate in the committee and for their valuable feedback during the defense. A special thanks to Wouter and Xavier for their support during this challenging and stressful moment.

I would like to thank my supervisor, Marie-Christine Firpo, for her guidance and support throughout my PhD. Thank you for giving me the opportunity to work under your supervision. I cherish your mentorship, knowledge, and perspective on the subject. I am especially grateful for your patience and the freedom you gave me to explore my ideas.

I would also like to extend my thanks to the fusion group at LPP, particularly Pierre and Özgür, for their constant help and support during my PhD. Your organization of rehearsals and words of encouragement meant so much to me. Furthermore, I want to thank the space plasma group at LPP. We shared many enjoyable lunches that I will always cherish, and you made me feel like a part of your group. A special mention goes to Nico, who kindly agreed to join my comité de suivi during the second year of my PhD but has been my unofficial mentor from the very first day we met. I am deeply grateful that I could always count on you to help me with any challenge and stand by my side. Thanks also to Alexis for rescuing me by fixing my computer when I thought I had lost all my simulation data.

Thanks to the administrative team, especially Cherifa, for helping me with my numerous trips during the PhD and so much more. I am also thankful to the IT team, particularly Nicolas, for helping me countless times with technical issues.

During my PhD, I had the pleasure of meeting many amazing people, but Bayane and Tarek are the best among them. I am so grateful for your friendship

and support during difficult moments (BAT forever). I would also like to thank my officemate Ayah for all the candies and kind words; Nadj for your help and ping-pong sessions; Giulio for sharing this journey with me and for all the laughs; and so many great people I met at LPP: Ambre, Paco, Xue, Davide, Thershi, Carolina, Vincent, Benoit, Dihya, and many others. I am grateful to everyone at LPP for welcoming me and making me feel at home. I am thankful to all who created this friendly atmosphere and made my PhD a great experience.

Next, I would like to thank my best friend Denys for our long Friday evening talks, your incredible support, and your ability to turn difficult situations into something we could laugh about afterwards. Thanks to Andrii for our after-work evenings and so much more. Thanks to Kateryna for always believing in me and for your encouragement.

I would also like to thank my family for their support throughout my PhD. I am incredibly grateful to my brother Heorhii and sister-in-law Hanna for always being there for me, and to my mom and dad for their unconditional love and support.

To my husband, Yaroslav: thank you for your incredible support and love, for all the sacrifices you made for me, for all the times you listened to me talk about my thesis, and for standing by my side. I am so grateful to have you in my life and for the love and encouragement you gave me throughout this journey. We finally made it!

Lastly, I would like to thank all the brave people of Ukraine for their fight for our freedom, and my friend Mykhailo, who gave his life defending our country. I am so proud of you, and I will always remember you.

Contents

List of Figures

List of Acronyms

CPU	central processing unit 22, 84
DEMO	DEMOnstration power plant 4, 5
EAST	The Experimental Advanced Superconducting Tokamak 65
ECCD	Electron Cyclotron Current Drive 65
EFDA	European Fusion Development Agreement 3
ELMs	Edge-Localized Modes 4
FEM	finite element method xvi, xvii, 18, 19, 21, 36, 37
GPU	graphics processing unit 84
H-mode	high-confinement mode 5
ITER	International Thermonuclear Experimental Reactor 3–5
JET	Joint European Torus xvi, xvii, 3, 16, 21, 28, 36, 37, 51, 52, 65
JT-60U	Japan Torus-60 (Upgrade) 5
L-mode	low-confinement mode 5
LHCD	Lower Hybrid Current Drive 65
LHS	left-hand-side 91
MHD	magnetohydrodynamic xiv, 5, 6, 11, 26, 27, 40, 43, 57, 61, 64, 65, 67, 80, 81, 83
NBI	Neutral Beam Injection 43, 65
NIF	National Ignition Facility xvi, 3

NSTX	National Spherical Torus Experiment 5
PDE	partial differential equations xiii, xiv, 6, 10, 11, 16, 18, 19, 26, 42, 44, 45
RF	radio-frequency 43
RHS	right-hand-side 91, 93

List of Symbols

Throughout the manuscript, certain symbols may appear with the following notations:

- a hat (e.g., $\hat{x}$) to denote their dimensionless form;
- a lower index φ (e.g., B_φ) to denote their toroidal component;
- a lower index *pol* (e.g., v_{pol}) to denote their poloidal component;
- a lower index x (e.g., v_x) to denote their component in the x direction;
- a lower index y (e.g., v_y) to denote their component in the y direction;
- a lower index rms (e.g., V_{rms}) to denote their root-mean-square.

A	Magnitude of the current drive
B_c	Characteristic magnetic field
B_0	External toroidal magnetic field
B	Offset of the current drive
E_0	Toroidal electric field
H	Hartmann number
L	Characteristic length
N	Number of triangles
R_e	Reynolds number
V_c	Characteristic plasma speed
Z	Atomic number

Ω	Cross-section plasma domain
Φ	Potential
$\boldsymbol{J}$	Current density vector
$\boldsymbol{\omega}$	Vorticity vector
χ	Magnetic flux
δ_0	Triangularity parameter
δ	Boundary layer thickness
ϵ	Tolerance parameter
η	Resistivity
$\mathbf{i}_\varphi$	Unit vector in toroidal direction
$\mathbf{v}_e$	Flow velocity of electrons
$\mathbf{v}_i$	Flow velocity of ions
$\mathbf{v}$	Velocity vector
μ_0	Permeability of free space
∇	Nabla operator
ν	Kinematic viscosity
ρ_m	Total mass density of plasma
ρ	Electric charge density
$\mathbf{B}$	Magnetic field vector
$\mathbf{E}$	Radial electric field
θ	Angular parameter
$\triangle$	Laplacian operator
e	Elementary charge
j_D	Second family of current drive
j_d	First family of current drive
j_{fixed}	Fixed toroidal current density
k	Plasma elongation
m_e	Mass of electron

m_i	Mass of ion
n_e	Density of electrons
n_i	Density of ions
p^*	Total pressure
p_e	Electron pressure
p_i	Ion pressure
p	Plasma pressure
r_0	Tokamak major radius
r_1	Semi-minor axis of the cross-section
u	Dimensionless variable of the system of parabolic PDE
$v_{A0} = b_0$	Alfvén velocity
x	Horizontal coordinate
y	Vertical coordinate

Chapter 1

General introduction

The power of the Sun, in the palm of my hand.

Dr. Otto Octavius

Contents

1.1 Fusion energy

Fusion energy is essential for addressing modern global energy challenges. The growth of the population increases energy demands even further. Figure 1.1 shows that by the year 2070, conventional energy sources will only be able to meet about 50 % of energy needs of humanity. Luckily, nuclear fusion offers a potential source of safe, clean, and renewable energy by replicating the processes that power the Sun [Conn et al., 1990]. This can address problems such as the exhaustion of fossil fuels, environmental pollution, and greenhouse gas emissions that contribute to climate change [Toschi, 1997]. There are two main methods to confine plasma for fusion on Earth: inertial confinement and magnetic confinement.

Inertial confinement achieves nuclear fusion by rapidly compressing and heating a small pellet of fuel, usually deuterium and tritium, to extremely high temperatures and pressures. It can be achieved by focusing intense laser or ion beams on the target, causing it to implode. This method has the potential for high energy yield from a relatively small amount of fuel. However, it poses significant technical

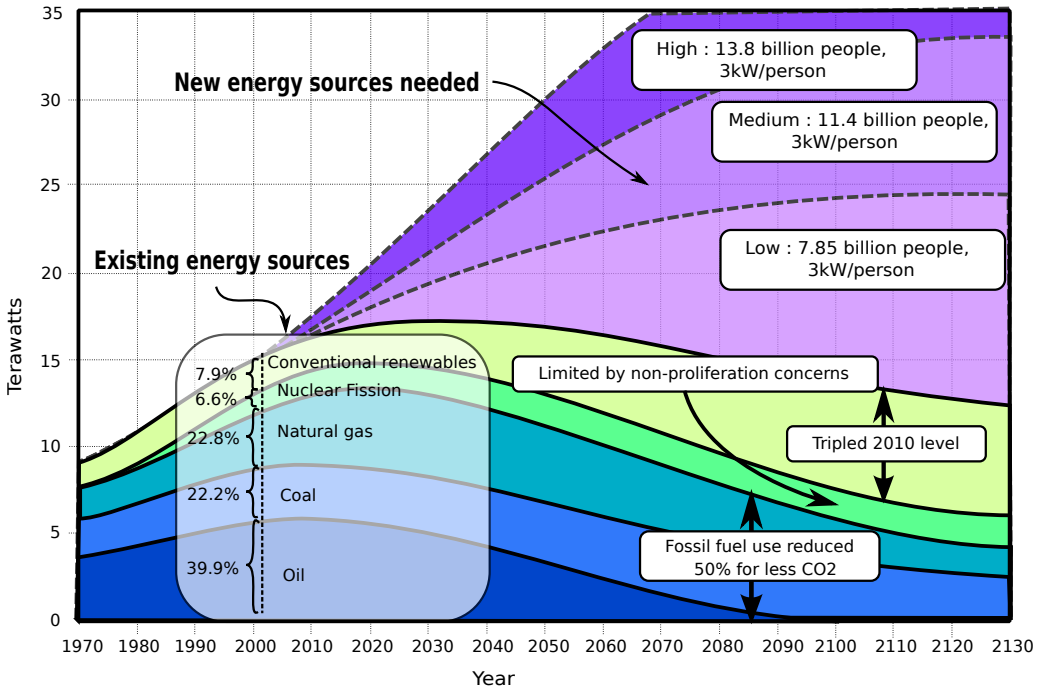

Figure 1.1: Energy supply and demand projection based on population growth, world energy consumption, and energy conservation. The violet-coloured regions indicate the need for new energy sources, such as fusion. Image source: [Vallet, 2014], originally adapted from [McLean, 2002].

challenges, which require precise control over the compression process [Nuckolls, 1982].

Magnetic confinement achieves nuclear fusion by using powerful magnetic fields to contain and control the plasma. There are several devices designed for this purpose. The most common device is the tokamak, which combines a strong doughnut-shaped magnetic field and a weaker poloidal magnetic field. This configuration keeps the plasma stable and confined in a toroidal shape [Artsimovich, 1972]. Stellarators use a similar approach but employ complex, twisted magnetic fields that do not require the plasma current needed in a tokamak [Spitzer, 1958]. Figure 1.2 shows examples of fusion devices based on the two described methods.

The magnetic field is vital in confining and keeping the plasma stable in a tokamak. It consists of two components: the toroidal magnetic field generated by a series of coils around the torus and the poloidal magnetic field induced by the plasma current. The relatively simple toroidal shape of the device is advantageous over intricately-shaped stellarators. It allows tokamaks to reach higher plasma densities and temperatures essential for achieving the conditions required for nuclear fusion. Figure 1.3 shows the structure of the device.

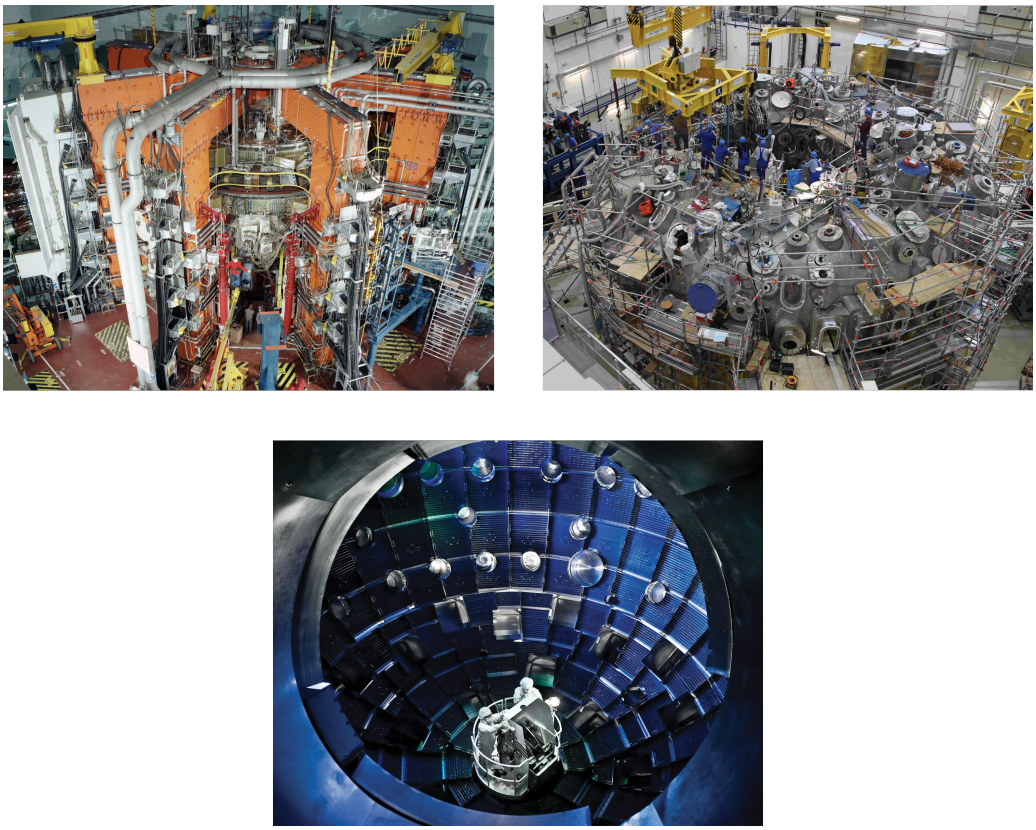

Figure 1.2: Different fusion devices. The upper-left photo shows the tokamak experiment Joint European Torus (JET) in 1991 (credit: EFDA JET). The upper-right photo shows the stellarator experiment Wendelstein 7-X in 2011 (credit: Max-Planck-Institut für Plasmaphysik). The bottom photo shows the National Ignition Facility (NIF) Target Chamber in 2008 (credit: United States Department of Energy). Upper images licensed under CC BY-SA 3.0.

The International Thermonuclear Experimental Reactor (ITER) represents state-of-the-art international collaborations in fusion research [Rebut et al., 1993]. It is the world's largest tokamak, aiming to achieve "net positive energy". This means producing more energy from fusion reactions than required to sustain the plasma, marking a significant step towards practical fusion power. This project highlights the significant focus on tokamaks within major fusion research initiatives like ITER. This leads to considerable advancements in understanding and improving the performance of tokamaks. Despite these advancements and the cutting-edge technology of ITER, a commercial fusion reactor still needs to be achieved. Although fusion research has been ongoing for over 60 years, developing a functional thermonuclear power plant is still a future prospect [Ball, 2021].

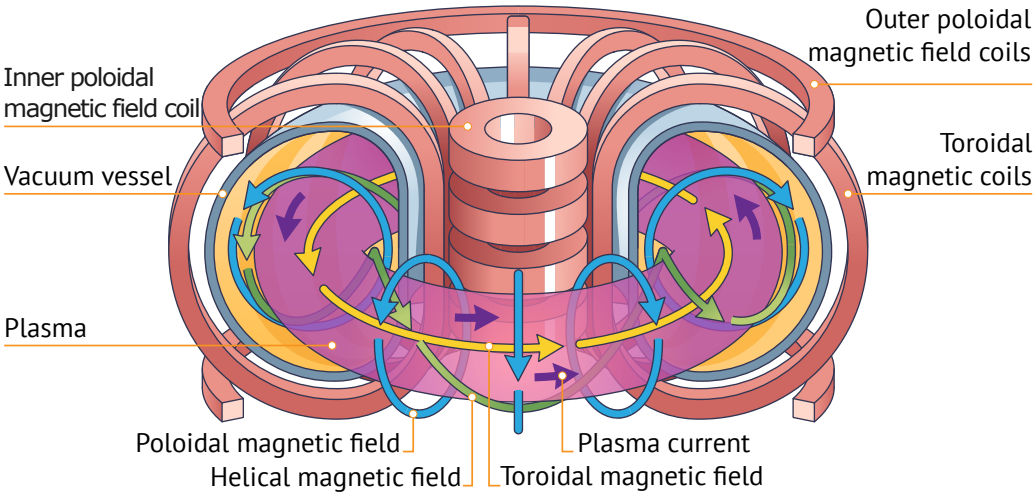

Figure 1.3: Tokamak structure and operation principle. Image source: Vector Mine/stock.adobe.com.

Finally, the DEMOnstration power plant (DEMO) project embodies the next generation of international fusion research initiatives [Federici et al., 2016]. Building upon the foundation of ITER, DEMO aims to become the first demonstration fusion power plant to produce between 300 MW to 500 MW net electricity for the electrical grid. Despite decades of research and development, achieving a commercial fusion reactor remains challenging, with the objective of electricity production around 2050.

1.2 Plasma rotation

The challenge of the magnetic confinement method lies in maintaining a stable magnetic field to control plasma. Its turbulence and instabilities, such as Edge-Localized Modes (ELMs) [Wagner et al., 1990], ballooning modes [Connor et al., 1978], and kink instabilities [von Goeler et al., 1974], are among the most significant issues within a tokamak. Unpredictable plasma disruptions [Wesson et al., 1989] lead to substantial heat losses and potential damage to the reactor walls [Boozer, 2012]. This makes the control and stabilization of plasma a critical aspect of fusion research.

Plasma rotation is an essential factor that significantly impacts the heat and particle confinement properties in tokamaks. It can stabilize the plasma by mitigating or even quenching instabilities. High-velocity rotation, when the plasma rotates at a fraction of the sound speed, can stabilize external modes [Bondeson and Ward, 1994] — disturbances or instabilities driven by external influences or boundary conditions. This rotation alters the stability thresholds of these modes, potentially preventing disruptions that compromise plasma confinement.

Experimental studies confirm the importance of plasma rotation. In certain experimental conditions, notably in large-scale tokamaks like the National Spherical Torus Experiment (NSTX) and Japan Torus-60 (Upgrade) (JT-60U), the stabilization threshold turns out to be lower than expected and achievable with low-rotation plasmas [Sabbagh et al., 2006; Takechi et al., 2007]. This indicates the relationship between plasma rotation and stability is more complex than initially thought. The plasma's magnetic configuration, temperature gradients, and collisionality significantly contribute to this intricate interaction.

The study of high-confinement mode (H-mode) plasmas indicates that the plasma rotation has an intrinsic nature [Rice et al., 2007]. This rotation, which occurs even without external momentum input, is primarily associated with the presence of $\mathbf{E} \times \mathbf{B}$ velocity induced by a radial electric field. Yet, this phenomenon is not limited by H-mode plasmas and is also present in low-confinement mode (L-mode) plasmas [Angioni et al., 2011]. These observations suggest that intrinsic rotation might be a more universal phenomenon in tokamaks, potentially playing a role in various confinement regimes.

Numerical simulations provide additional insights into the effects of toroidal and poloidal flows on tokamak plasma equilibrium. These flows can significantly impact the distribution of pressure and magnetic fields within the plasma [Guazzotto et al., 2004; Guazzotto and Betti, 2005]. Moreover, the axisymmetric steady-state plasma velocity may play a critical role in separating magnetic and current density channels, as suggested by modifying the static Grad-Shafranov equilibrium condition [Firpo, 2024]. This separation could have important implications for the stability and control of the plasma, particularly in the context of advanced tokamak scenarios where current profile control is essential for maintaining long-duration plasma discharges.

Building upon these considerations, understanding and enhancing plasma rotation velocity are vital goals in magnetic confinement fusion research. Achieving this could lead to better control over plasma instabilities, improved confinement, and a more reliable path toward achieving sustained nuclear fusion. The role of rotation in the broader context of plasma turbulence, transport, and confinement must be further explored, particularly as we move toward the next generation of fusion devices like ITER and DEMO.

1.3 Thesis overview

Ideally, the tokamak should work stationary as a fusion reactor. It is, therefore, reasonable to determine the steady states of a tokamak plasma in full generality without imposing the nullity of the plasma velocity field. This work will address the problem of plasma rotation in the tokamaks by considering the visco-resistive magnetohydrodynamic (MHD) framework.

The thesis consists of the following chapters:

- Chapter 2 introduces MHD framework with the derivation of the system of axisymmetric steady-states of the visco-resistive MHD equations. It then moves on to the numerical simulations conducted using the finite element method via the open-source platform FreeFem++ for solving partial differential equations (PDE). The chapter concludes with the preliminary results obtained from this model and simulations.

- Chapter 3 focuses on the behaviour of the system for a constant toroidal current drive and derives scaling laws for the velocity. These scaling laws are expected to be valid if the magnitude of the inertial $\boldsymbol{\omega} \times \mathbf{v}$ term is small enough. This prediction is tested and validated using numerical simulations. This scaling law is expressed as a function of the resistivity, η, and the Hartmann number, H, where H is defined as $H \equiv (\eta\nu)^{-1/2}$, with ν denoting viscosity. The observed behaviour indicates that the velocity scales as $\eta f(H)$, where f is a specific function. This scaling law remains valid under the condition that the inertial term $\boldsymbol{\omega} \times \mathbf{v}$ remains negligible, which happens to be the case up to the largest numerically accessible values of the Hartmann number. Within this general scaling law, this chapter numerically uncovers, for a given, order-one, E_0/η drive, two limiting regimes at low and high H where the function f behaves as a power law.

- Chapter 4 discusses the limitations of the model proposed by [Kamp and Montgomery, 2003, 2004; Kamp et al., 1998] for describing tokamak plasmas within a MHD visco-resistive framework. It is predicted that this system yields zero pressure in the ideal and motionless limit, which makes it necessary to reconsider using $\hat{E}_0/\eta$ as the sole drive in the system. I establish a Poisson's equation for the pressure of the system to verify the pressure profiles without additional heating methods. Therefore, this chapter proposes the application of an additional drive to model heating methods applied in real tokamaks, verified through pressure profiles.

- Chapter 5 introduces an alternative model to address the dependence of the toroidal current on the Hartmann number. Proposing a model with fixed current profiles reveals a new scaling regime in toroidal velocity when the toroidal current profiles are fixed. It also investigates the effect of non-nested magnetic field lines on the scaling of the first and second regimes, as well as non-linear effects on the system.

- Chaper 6 concludes the thesis with key findings and contributions in this work and outlines perspectives for future research.

Bibliography

Angioni, C., McDermott, R. M., Casson, F. J., Fable, E., Bottino, A., Dux, R., Fischer, R., Podoba, Y., Pütterich, T., Ryter, F., and Viezzer, E. (2011). Intrinsic toroidal rotation, density peaking, and turbulence regimes in the core of tokamak plasmas. *Physical Review Letters*, 107(21):215003, DOI: 10.1103/PhysRevLett.107.215003.

Artsimovich, L. (1972). Tokamak devices. *Nuclear Fusion*, 12(2):215–252, ISSN: 0029-5515, 1741-4326, DOI: 10.1088/0029-5515/12/2/012.

Ball, P. (2021). The chase for fusion energy. https://www.nature.com/immersive/d41586-021-03401-w/index.html.

Bondeson, A. and Ward, D. J. (1994). Stabilization of external modes in tokamaks by resistive walls and plasma rotation. *Physical Review Letters*, 72(17):2709–2712, DOI: 10.1103/PhysRevLett.72.2709.

Boozer, A. H. (2012). Theory of tokamak disruptions. *Physics of Plasmas*, 19(5):058101, ISSN: 1070-664X, DOI: 10.1063/1.3703327.

Conn, R., Holdren, J., Sharafat, S., Steiner, D., Ehst, D., Hogan, W., Krakowski, R., Miller, R., Najmabadi, F., and Schultz, K. (1990). Economic, safety and environmental prospects of fusion reactors. *Nuclear Fusion*, 30(9):1919–1934, ISSN: 0029-5515, 1741-4326, DOI: 10.1088/0029-5515/30/9/015.

Connor, J. W., Hastie, R. J., and Taylor, J. B. (1978). Shear, Periodicity, and Plasma Ballooning Modes. *Physical Review Letters*, 40(6):396–399, DOI: 10.1103/PhysRevLett.40.396.

Federici, G., Bachmann, C., Biel, W., Boccaccini, L., Cismondi, F., Ciattaglia, S., Coleman, M., Day, C., Diegele, E., Franke, T., Grattarola, M., Hurzlmeier, H., Ibarra, A., Loving, A., Maviglia, F., Meszaros, B., Morlock, C., Rieth, M., Shannon, M., Taylor, N., Tran, M., You, J., Wenninger, R., and Zani, L. (2016). Overview of the design approach and prioritization of R&D activities towards an EU DEMO. *Fusion Engineering and Design*, 109–111:1464–1474, ISSN: 09203796, DOI: 10.1016/j.fusengdes.2015.11.050.

Firpo, M.-C. (2024). Interplay of the magnetic and current density field topologies in axisymmetric devices for magnetic confinement fusion.

Guazzotto, L. and Betti, R. (2005). Magnetohydrodynamics equilibria with toroidal and poloidal flowa). *Physics of Plasmas*, 12(5):056107, ISSN: 1070-664X, DOI: 10.1063/1.1869502.

Guazzotto, L., Betti, R., Manickam, J., and Kaye, S. (2004). Numerical study of tokamak equilibria with arbitrary flow. *Physics of Plasmas*, 11(2):604–614, ISSN: 1070-664X, DOI: 10.1063/1.1637918.

Kamp, L. P. and Montgomery, D. C. (2003). Toroidal flows in resistive magnetohydrodynamic steady states. *Physics of Plasmas*, 10:157–167, DOI: 10.1063/1.1524629.

Kamp, L. P. and Montgomery, D. C. (2004). Toroidal steady states in visco-resistive magnetohydrodynamics. *Journal of Plasma Physics*, 70(2):113–142, DOI: 10.1017/S0022377803002629.

Kamp, L. P., Montgomery, D. C., and Bates, J. W. (1998). Toroidal flows in resistive magnetohydrodynamic steady states. *Physics of Fluids*, 10(7):1757–1766, ISSN: 1070-6631, DOI: 10.1063/1.869692.

McLean, A. (2002). The ITER fusion reactor and its role in the development of a fusion power plant. *Canadian Nuclear Society Bulletin*, 23(2):13–18, ISSN: 0714-7074.

Nuckolls, J. H. (1982). The feasibility of inertial-confinement fusion. *Physics Today*, 35(9):24–31, ISSN: 0031-9228, 1945-0699, DOI: 10.1063/1.2915258.

Rebut, P.-H., Boucher, D., Gambier, D., Keen, B., and Watkins, M. (1993). The ITER challenge. *Fusion Engineering and Design*, 22(1-2):7–18, ISSN: 09203796, DOI: 10.1016/S0920-3796(05)80004-3.

Rice, J., Ince-Cushman, A., deGrassie, J., Eriksson, L.-G., Sakamoto, Y., Scarabosio, A., Bortolon, A., Burrell, K., Duval, B., Fenzi-Bonizec, C., Greenwald, M., Groebner, R., Hoang, G., Koide, Y., Marmar, E., Pochelon, A., and Podpaly, Y. (2007). Inter-machine comparison of intrinsic toroidal rotation in tokamaks. *Nuclear Fusion*, 47(11):1618, DOI: 10.1088/0029-5515/47/11/025.

Sabbagh, S. A., Bell, R. E., Menard, J. E., Gates, D. A., Sontag, A. C., Bialek, J. M., LeBlanc, B. P., Levinton, F. M., Tritz, K., and Yuh, H. (2006). Active stabilization of the resistive-wall mode in high-beta, low-rotation plasmas. *Physical Review Letters*, 97(4):045004, DOI: 10.1103/PhysRevLett.97.045004.

Spitzer, L. (1958). The Stellarator Concept. *The Physics of Fluids*, 1(4):253–264, ISSN: 0031-9171, DOI: 10.1063/1.1705883.

Takechi, M., Matsunaga, G., Aiba, N., Fujita, T., Ozeki, T., Koide, Y., Sakamoto, Y., Kurita, G., Isayama, A., and Kamada, Y. (2007). Identification of a low plasma-rotation threshold for stabilization of the resistive-wall mode. *Physical Review Letters*, 98(5):055002, DOI: 10.1103/PhysRevLett.98.055002.

Toschi, R. (1997). Nuclear fusion, an energy source. *Fusion Engineering and Design*, 36(1):1–8, ISSN: 09203796, DOI: 10.1016/S0920-3796(97)00007-0.

Vallet, A. (2014). *Hydrodynamic Modelling of the Shock Ignition Scheme for Inertial Confinement Fusion*. PhD thesis, Université de Bordeaux.

von Goeler, S., Stodiek, W., and Sauthoff, N. (1974). Studies of Internal Disruptions and $m=1$ Oscillations in Tokamak Discharges with Soft—X-Ray Tecniques. *Physical Review Letters*, 33(20):1201–1203, DOI: 10.1103/PhysRevLett.33.1201.

Wagner, F., Field, A. R., Fussmann, G., Hofmann, J. V., Manso, M. E., Vollmer, O., and Matias, J. (1990). Recent results of H-mode studies on Asdex. *13th International Conference on Plasma Physics and Controlled Nuclear Fusion*, pages 277–290.

Wesson, J. A., Gill, R. D., Hugon, M., Schüller, F. C., Snipes, J. A., Ward, D. J., Bartlett, D. V., Campbell, D. J., Duperrex, P. A., Edwards, A. W., Granetz, R. S., Gottardi, N. A. O., Hender, T. C., Lazzaro, E., Lomas, P. J., Cardozo, N. L., Mast, K. F., Nave, M. F. F., Salmon, N. A., Smeulders, P., Thomas, P. R., Tubbing, B. J. D., Turner, M. F., and Weller, A. (1989). Disruptions in JET. *Nuclear Fusion*, 29(4):641, ISSN: 0029-5515, DOI: 10.1088/0029-5515/29/4/009.

Chapter 2

Methodology

The essence of science is its method: to question, to experiment, and to learn.

Richard Feynman

Contents

2.1 Introduction

Understanding and controlling plasma rotation is an essential research objective for achieving enhanced plasma performance and sustainable fusion reactions in

tokamak devices. To address this matter, we reconsider the derivation of the axisymmetric steady-states of the visco-resistive magnetohydrodynamic equations without making a no-flow hypothesis. This means that we reintroduce in the traditional Grad-Shafranov equation the dissipative viscous term and the non-linear $(\mathbf{v}\cdot\nabla)\mathbf{v}$ term coming from the steady-state Navier-Stokes equation [Kamp and Montgomery, 2003; Kamp et al., 1998; Morales et al., 2012; Holst et al., 2022; Oueslati et al., 2019; Oueslati and Firpo, 2020; Roverc'h et al., 2021; Krupka and Firpo, 2024]. In Section 2.2, we propose a step-by-step derivation of the dimensionless closed system of partial differential equations, first introduced in [Kamp and Montgomery, 2003] to model tokamak plasmas within a MHD visco-resistive setting. Section 2.3 is dedicated to the performance of numerical simulations, including discussion on the computational domain, boundary conditions used, weak formulation of the equations and the Newton-Raphson method. These simulations use the finite element method through the open-source platform FreeFem++ for solving PDE [Hecht, 2012]. This chapter concludes with the first numerical results and the discussion of the computational time.

2.2 Axisymmetric steady-states

2.2.1 Derivation of the dimensionless system of PDE

Let us first propose a step-by-step derivation of the single fluid MHD description of steady-state tokamak plasmas without proceeding to a zero velocity assumption. Denoting by ρ_m, the total mass density of plasma, by n_i the number density of ions, by n_e the number density of electrons, by ρ the electric charge density, by p the plasma pressure, by $\mathbf{v}$ the flow velocity of plasma and by $\mathbf{j}$ the current density, one obtains the following identities

$$\begin{aligned}
\rho_m &= n_i m_i \left(1+\frac{m_e}{m_i Z}\right), \\
\rho &= -e\left(n_e - Z n_i\right), \\
p &= p_i + p_e, \\
\mathbf{v} &= \mathbf{v}_i + \frac{m_e}{m_i} Z\left(\mathbf{v}_e - \mathbf{v}_i\right), \\
\mathbf{j} &= -e n_e \left(\mathbf{v}_e - \mathbf{v}_i\right).
\end{aligned}$$

The steady-state equation of motion ($\partial/\partial t = 0$) for the one-fluid model is

$$\rho_m \left(\mathbf{v}\cdot\nabla\right)\mathbf{v} = -\nabla p + \rho\mathbf{E} + \mathbf{j}\times\mathbf{B} + \mu\nabla^2\mathbf{v}. \tag{2.1}$$

with

$$\left(\mathbf{v}\cdot\nabla\right)\mathbf{v} = \nabla\left(\frac{v^2}{2}\right) + \boldsymbol{\omega}\times\mathbf{v} \tag{2.2}$$

where $\boldsymbol{\omega}$ is the vorticity vector that $\boldsymbol{\omega} = \nabla \times \mathbf{v}$.
Assuming electroneutrality ($\rho = 0$), this gives

$$\rho_m \boldsymbol{\omega} \times \mathbf{v} = -\nabla p^* + \mathbf{j} \times \mathbf{B} + \mu \nabla^2 \mathbf{v} \tag{2.3}$$

with

$$p^* = p + \rho_m \frac{v^2}{2}. \tag{2.4}$$

Introducing the kinematic viscosity $\nu = \mu/\rho_m$, this amounts to

$$\boldsymbol{\omega} \times \mathbf{v} = -\nabla \left(\frac{p^*}{\rho_m} \right) + \rho_m^{-1} \mathbf{j} \times \mathbf{B} + \nu \nabla^2 \mathbf{v} \tag{2.5}$$

with

$$\nabla \times \mathbf{B} = \mu_0 \mathbf{j}. \tag{2.6}$$

Ohm's law reads

$$\mathbf{E} + \mathbf{v} \times \mathbf{B} = \eta \mathbf{j}. \tag{2.7}$$

Let us assume that the plasma is incompressible, meaning its mass density is constant $\rho = \rho_{m0}$. Let us introduce the dimensionless variables $\hat{\mathbf{v}} = \mathbf{v}/v_{A0} = \mathbf{v}/b_0$ and $\hat{\mathbf{b}} = \mathbf{b}/b_0$, where $\mathbf{b} = \mathbf{v}_A = \mathbf{B}/\sqrt{\mu_0 \rho_{m0}}$ with the Alfvén velocity $v_{A0} = b_0$ defined by

$$b_0 = \frac{B_0}{\sqrt{\mu_0 \rho_{m0}}} \tag{2.8}$$

and $\hat{\nabla} = r_0 \nabla$, where r_0 denotes the tokamak major radius. Let us then also define the spatial variables rescaled by r_0, so that the horizontal and vertical coordinates are $x = r/r_0$ and $y = z/r_0$. As we focus on axisymmetric toroidal-invariant steady-states, all spatial dependence can be expressed in the variables x and y. The integration domain will be the tokamak plasma poloidal cross-section (see Sect. 2.3.1). This gives

$$\left(\hat{\nabla} \times \hat{\mathbf{v}} \right) \times \hat{\mathbf{v}} = -\hat{\nabla} \left(\hat{p^*} \right) + \left(\hat{\nabla} \times \hat{\mathbf{b}} \right) \times \hat{\mathbf{b}} + \hat{\nu} \hat{\nabla}^2 \hat{\mathbf{v}} \tag{2.9}$$

with the dimensionless viscosity

$$\hat{\nu} = \frac{\nu}{b_0 r_0}, \tag{2.10}$$

and dimensionless total pressure

$$\hat{p^*} = \frac{p^*}{b_0^2 \rho_m}. \tag{2.11}$$

As for the Ohm's law, we have

$$\frac{E_0}{x} \mathbf{i}_\varphi - \nabla \Phi + b_0^2 \sqrt{\mu_0 \rho_{m0}} \hat{\mathbf{v}} \times \hat{\mathbf{b}} = \frac{\eta \sqrt{\mu_0 \rho_{m0}}}{\mu_0} b_0 r_0 \hat{\nabla} \times \hat{\mathbf{b}} \tag{2.12}$$

with $\mathbf{E} = \frac{E_0}{x}\mathbf{i}_\varphi - \nabla\Phi$ (so that $\nabla \times \mathbf{E} = 0$). Taking the curl of the Ohm's law, we get

$$b_0^2\sqrt{\mu_0\rho_{m0}}\hat{\nabla} \times \left(\hat{\mathbf{v}} \times \hat{\mathbf{b}}\right) = \frac{\eta\sqrt{\mu_0\rho_{m0}}}{\mu_0} b_0 r_0^{-1}\hat{\nabla} \times \left(\hat{\nabla} \times \hat{\mathbf{b}}\right). \tag{2.13}$$

Consequently, the rescaled resistivity $\hat{\eta}$ should be such that

$$\hat{\eta} = \frac{\eta}{\mu_0 r_0 b_0}. \tag{2.14}$$

The full Ohm's law reads, then

$$\left(b_0^2\sqrt{\mu_0\rho_{m0}}\right)^{-1}\left(\frac{E_0}{x}\mathbf{i}_\varphi - \nabla\Phi\right) + \hat{\mathbf{v}} \times \hat{\mathbf{b}} = \hat{\eta}\hat{\nabla} \times \hat{\mathbf{b}} \tag{2.15}$$

so that the rescaled, dimensionless electric field is such that

$$\hat{E}_0 = \frac{E_0}{b_0^2\sqrt{\mu_0\rho_{m0}}} \tag{2.16}$$

with

$$\frac{\hat{E}_0}{x}\mathbf{i}_\varphi - \hat{\nabla}\hat{\Phi} + \hat{\mathbf{v}} \times \hat{\mathbf{b}} = \hat{\eta}\hat{\nabla} \times \hat{\mathbf{b}}. \tag{2.17}$$

Summarizing, we have with $\hat{\omega} = \hat{\nabla} \times \hat{\mathbf{v}}$ and $\hat{\mathbf{j}} = \hat{\nabla} \times \hat{\mathbf{b}}$,

$$\hat{\omega} \times \hat{\mathbf{v}} = -\hat{\nabla}\left(\frac{p^*}{b_0^2\rho_m}\right) + \hat{\mathbf{j}} \times \hat{\mathbf{b}} + \hat{\nu}\hat{\nabla}^2\hat{\mathbf{v}} \tag{2.18}$$

$$\frac{\hat{E}_0}{x}\mathbf{i}_\varphi - \hat{\nabla}\hat{\Phi} + \hat{\mathbf{v}} \times \hat{\mathbf{b}} = \hat{\eta}\hat{\mathbf{j}} \tag{2.19}$$

with

$$\hat{\nabla} \cdot \hat{\mathbf{v}} = 0,$$
$$\hat{\nabla} \cdot \hat{\mathbf{b}} = 0.$$

Writing

$$\mathbf{B} = \hat{\nabla}\frac{\chi}{r_0} \times \frac{1}{r_0 x}\mathbf{i}_\varphi + \left(B_0\frac{r_0}{r} + B_\varphi\right)\mathbf{i}_\varphi \tag{2.20}$$

so that

$$\hat{\mathbf{b}} = \frac{1}{x}\hat{\nabla}\hat{\chi} \times \mathbf{i}_\varphi + \left(\frac{1}{x} + \hat{b}_\varphi\right)\mathbf{i}_\varphi, \tag{2.21}$$

where the rescaled magnetic flux is

$$\hat{\chi} = \frac{\chi}{B_0 r_0^2}, \tag{2.22}$$

ensures that Gauss's equation is satisfied. Ampère's law gives

$$\hat{\mathbf{j}} = \frac{1}{x}\hat{\nabla}\left(x\hat{b}_\varphi\right) \times \mathbf{i}_\varphi - \frac{1}{x}\left(\hat{\triangle}^*\hat{\chi}\right)\mathbf{i}_\varphi \tag{2.23}$$

where the operator $\hat{\triangle}^*$ is defined by

$$\hat{\triangle}^* A = \hat{\nabla}^2 A - \frac{2}{x}\frac{\partial A}{\partial x} = \frac{\partial^2 A}{\partial x^2} - \frac{1}{x}\frac{\partial A}{\partial x} + \frac{\partial^2 A}{\partial y^2}. \tag{2.24}$$

We have

$$\mathbf{v} = \hat{\nabla}\frac{\psi}{r_0} \times \frac{1}{r_0 x}\mathbf{i}_\varphi + v_\varphi \mathbf{i}_\varphi \tag{2.25}$$

so that

$$\hat{\mathbf{v}} = \frac{1}{x}\hat{\nabla}\hat{\psi} \times \mathbf{i}_\varphi + \hat{v}_\varphi \mathbf{i}_\varphi \tag{2.26}$$

with

$$\hat{\psi} = \frac{\psi}{b_0 r_0^2}. \tag{2.27}$$

And the dimensionless vorticity reads

$$\hat{\boldsymbol{\omega}} = \frac{1}{x}\hat{\nabla}\left(x\hat{v}_\varphi\right) \times \mathbf{i}_\varphi - \frac{1}{x}\left(\hat{\triangle}^*\hat{\psi}\right)\mathbf{i}_\varphi. \tag{2.28}$$

The toroidal part of Equation (2.28) gives

$$\hat{\triangle}^*\hat{\psi} = -x\hat{\omega}_\varphi. \tag{2.29}$$

Taking the curl of the force balance, one obtains

$$\hat{\nabla} \times \left(\hat{\omega} \times \hat{\mathbf{v}} - \hat{\mathbf{j}} \times \hat{\mathbf{b}}\right) = \hat{\nu}\hat{\nabla}^2\hat{\omega}. \tag{2.30}$$

Defining $\tilde{u}_1 = \hat{\psi}$, $u_2 = x\hat{\omega}_\varphi$, $\tilde{u}_3 = x\hat{b}_\varphi + 1$, $\tilde{u}_4 = x\hat{v}_\varphi$, $\tilde{u}_5 = \hat{\chi}$, $\tilde{u}_6 = x\hat{j}_\varphi$, Equation (2.29) reads

$$\hat{\triangle}^*\tilde{u}_1 = -u_2. \tag{2.31}$$

Here we would like to introduce the Poisson bracket $\{u, v\}$ for any space functions u and v by

$$\{u, v\} \equiv \frac{\partial u}{\partial x}\frac{\partial v}{\partial y} - \frac{\partial v}{\partial x}\frac{\partial u}{\partial y}. \tag{2.32}$$

We get from the toroidal part of the curl of the force balance (2.30)

$$\hat{\nu}\hat{\triangle}^* u_2 = \frac{1}{x^2}\frac{\partial}{\partial y}(\tilde{u}_3^2 - \tilde{u}_4^2) + \frac{1}{x}\{\tilde{u}_6, \tilde{u}_5\} + \frac{1}{x}\{\tilde{u}_1, u_2\} + \frac{2u_2}{x^2}\frac{\partial \tilde{u}_1}{\partial y} - \frac{2\tilde{u}_6}{x^2}\frac{\partial \tilde{u}_5}{\partial y}. \tag{2.33}$$

The curl of Ohm's law gives

$$\hat{\nabla} \times \left(\hat{\mathbf{v}} \times \hat{\mathbf{b}}\right) = \hat{\eta}\hat{\nabla} \times \hat{\mathbf{j}} \tag{2.34}$$

which yields along the toroidal direction

$$\hat{\eta}\hat{\triangle}^* u_3 = \frac{1}{x}\{\tilde{u}_1, \tilde{u}_3\} + \frac{1}{x}\{\tilde{u}_4, \tilde{u}_5\} + \frac{2\tilde{u}_3}{x^2}\frac{\partial \tilde{u}_1}{\partial y} - \frac{2\tilde{u}_4}{x^2}\frac{\partial \tilde{u}_5}{\partial y}. \tag{2.35}$$

The toroidal part of the force balance equation (2.18) under the axisymmetric hypothesis yields

$$\left(\hat{\nu}\hat{\nabla}^2\hat{\mathbf{v}}\right)\cdot\mathbf{i}_\varphi=\left(\hat{\omega}\times\hat{\mathbf{v}}-\hat{\mathbf{j}}\times\hat{\mathbf{b}}\right)\cdot\mathbf{i}_\varphi \tag{2.36}$$

giving

$$\hat{\nu}\hat{\triangle}^*\tilde{u}_4=\frac{1}{x}\left\{\tilde{u}_1,\tilde{u}_4\right\}+\frac{1}{x}\left\{\tilde{u}_3,\tilde{u}_5\right\}. \tag{2.37}$$

And finally, we have the counterpart of Equation (2.31) for the magnetics, namely

$$\hat{\triangle}^*\tilde{u}_5=-\tilde{u}_6. \tag{2.38}$$

The toroidal part of Ohm's law finally gives

$$\frac{\hat{E}_0}{x}+\left(\hat{\mathbf{v}}\times\hat{\mathbf{b}}\right)\cdot\mathbf{i}_\varphi=\hat{\eta}\hat{\mathbf{j}}\cdot\mathbf{i}_\varphi \tag{2.39}$$

that is

$$\hat{\eta}\tilde{u}_6=\hat{E}_0+\frac{1}{x}\left\{\tilde{u}_5,\tilde{u}_1\right\}. \tag{2.40}$$

2.2.2 Toroidal current drive

To be consistent with the notations of [Kamp and Montgomery, 2003], let us introduce two current characteristic scales, namely the order of magnitude of the current that would be needed in a vertical infinite wire to produce the toroidal magnetic field at the center of the plasma column

$$I_b=\frac{r_0B_0}{\mu_0} \tag{2.41}$$

and the order of magnitude of the current involved in Joule heating of the plasma under the loop voltage E_0

$$I_e=\frac{r_0^2E_0}{\eta}. \tag{2.42}$$

Using the expressions of the dimensionless resistivity, $\hat{\eta}$ from Equation (2.14), and dimensionless toroidal electric field, $\hat{E}_0$ (2.16), one obtains the following relation

$$\frac{\hat{E}_0}{\hat{\eta}}=\frac{I_e}{I_b}. \tag{2.43}$$

The calculations of Section 2.2.1 have just shown that it is not necessary to introduce explicitly these two current characteristic scales in the system of equations. However, in the present study, we are interested in the behaviour of the system for a given ratio of these currents in Equation (2.43), namely for a given $\hat{E}_0/\hat{\eta}$. This quantity may be viewed as the only explicit drive appearing in the dimensionless system of equations as written in the following Section 2.2.3. Equation (2.43) shows that this control parameter amounts to the ratio of the electric current involved for plasma Ohmic heating over that needed for generating the external toroidal magnetic field.

2.2.3 Final set of equations

Summarizing the above calculations and dropping some tildes to improve readability, one is left with the system of parabolic PDE of [Kamp and Montgomery, 2003]

$$\triangle^* u_1 = -u_2, \tag{2.44}$$

$$\hat{\nu}\triangle^* u_2 = \frac{1}{x^2}\frac{\partial}{\partial y}(u_3^2 - u_4^2) + \frac{1}{x}\{u_6, u_5\} + \frac{1}{x}\{u_1, u_2\} + \frac{2u_2}{x^2}\frac{\partial u_1}{\partial y} - \frac{2u_6}{x^2}\frac{\partial u_5}{\partial y}, \tag{2.45}$$

$$\hat{\eta}\triangle^* u_3 = \frac{1}{x}\{u_1, u_3\} + \frac{1}{x}\{u_4, u_5\} + \frac{2u_3}{x^2}\frac{\partial u_1}{\partial y} - \frac{2u_4}{x^2}\frac{\partial u_5}{\partial y}, \tag{2.46}$$

$$\hat{\nu}\triangle^* u_4 = \frac{1}{x}\{u_1, u_4\} + \frac{1}{x}\{u_3, u_5\}, \tag{2.47}$$

$$\triangle^* u_5 = -u_6, \tag{2.48}$$

with

$$\hat{\eta}u_6 = \hat{E}_0 + \frac{1}{x}\{u_5, u_1\}, \tag{2.49}$$

where all the dimensionless variables have been defined in Section 2.2.1. From now on, only dimensionless variables will be used, and to simplify notation, we will denote them without the hat symbol.

2.3 Numerical Simulations

2.3.1 Domain and boundary conditions

We need to establish and define the computational cross-section plasma domain Ω to solve the system of equations (2.44)-(2.49). In this work, all simulations are carried out within a 2D JET geometry, meaning that the parametric equations define the plasma border

$$\begin{cases} x = 1 + \dfrac{r_1}{r_0}\cos\left(\theta + \arcsin\delta_0 \sin\theta\right) \\ y = k\dfrac{r_1}{r_0}\sin(\theta) \end{cases} \tag{2.50}$$

Here $\theta \in [0, 2\pi]$, r_0 is the major radius, r_1 is the semi-minor axis of the cross-section, δ_0 is the triangularity parameter, and k is the plasma elongation. For our simulations, we use typical JET parameters: the major radius is $r_0 = 3$ m, the semi-minor axis radius is $r_1 = 1.25$ m, the plasma elongation $k = 1.55$, and finally $\arcsin\delta_0 = 0.5$. With these parameters, we can visualize the cross-section plasma domain Ω. Figure 2.1 illustrates the geometry of the problem. The external toroidal magnetic field value, denoted as B_0, is set at 2.8 Tesla (T), a setting consistent with the conditions in the JET experiment [JET Team, 1992]. We chose the toroidal loop voltage equal to 1 V. This is a reasonable assumption since the

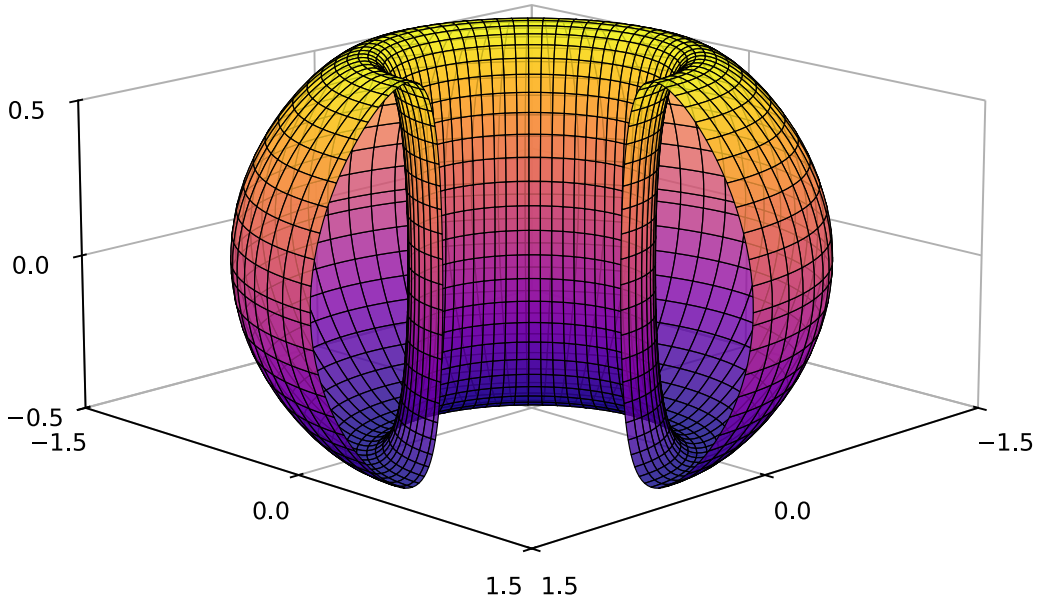

Figure 2.1: Three-fourth of the full plasma domain. Due to assumed axisymmetry, the problem is invariant under rotation along the toroidal angle, allowing us to focus on the 2D (x, y) cross-section Ω.

toroidal electric field is of the order of some V/m in the current devices. The velocities are scaled using Alfvénic units, where the Alfvén velocity, represented as b_0, is estimated to be approximately 5.5×10^6 meters per second (m/s) according to Equation (2.8). Similarly, based on Equation (2.16), the normalized electric field, denoted by E_0, is approximated to be of the order of 3.5×10^{-9}.

We now introduce the boundary conditions on $\partial\Omega$. The elliptic system (2.44)-(2.48) requires five boundary conditions. The four associated with the divergence-free properties of the magnetic field ($\mathbf{b}$), current density ($\mathbf{j}$), velocity ($\mathbf{v}$), and vorticity (ω) vector fields can be determined by ensuring the continuity of their normal components along the plasma boundary. In the numerical simulations, the following boundary conditions have been selected: $u_1 = u_5 = 0$ and $u_3 = 1$. Concerning u_2 and u_4, a toroidal "no-slip" condition is imposed, with $u_2 = u_4 = 0$. Alternatively, three additional boundary conditions will be chosen apart from the toroidal no-slip boundary condition. In the toroidal direction, a free-slip condition known as shear-stress free is represented by the condition $\partial_n(u_4/r^2) = 0, u_2 = 0$. A normal component of toroidal velocity equal to 0 is represented by the condition $\partial_n(u_4/x) = 0, u_2 = 0$. Finally, we shall enforce Neumann boundary conditions on toroidal velocity and vorticity through $\partial_n(u_4/x) = \partial_n(u_2/x) = 0$. The enforcement of the Neumann boundary conditions in this system is presented in Appendix A.

2.3.2 Finite element method

To solve the system of equations (2.44)-(2.49) on the cross-section plasma domain Ω together with boundary conditions, we use the finite element method (FEM). The FEM is a numerical technique that finds an approximate solution to boundary value problems for PDE. To solve a problem, the FEM breaks down a large system into smaller, simpler components known as finite elements. This is done through a specific discretization of the spatial dimensions. It can be achieved by constructing a mesh over the object, creating a numerical domain with a finite set of points. The FEM formulation of a boundary value problem ultimately leads to a system of algebraic equations. Then, it approximates the unknown function across the domain. The simple equations governing these finite elements combine to form a larger system representing the entire problem. The FEM then finds an approximate solution by minimizing an associated error function using the calculus of variations. The example of how a finite element works on the problem is shown in Figure 2.2

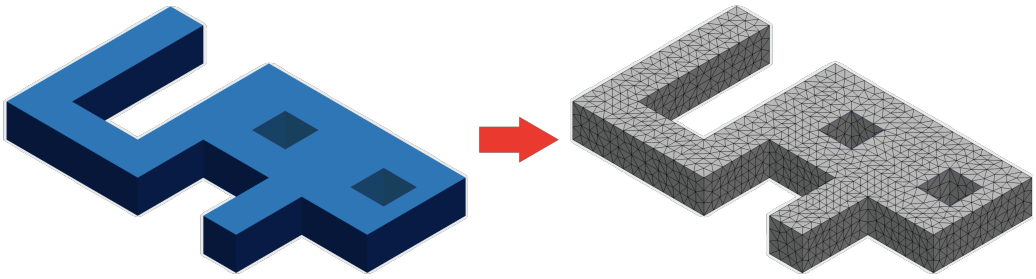

Figure 2.2: Visualization of FEM. The image shows the transformation of a 3D geometric model (on the left) into a finite element mesh (on the right), where the structure is discretized into smaller, triangular elements.

2.3.3 Weak formulation

To use FEM, we need to have our system of equations in the weak form. The weak formulation is a mathematical technique to solve PDE by transforming the problem into an equivalent variational form. The system of equations (2.44)-(2.49) needs to be derived by multiplying each equation by a test function and integrating over the domain Ω. This method is beneficial for solving problems with complex geometries and boundary conditions. Let us consider an example of Poisson's equation to illustrate the weak formulation. Let Poisson's equation be defined over a domain $\Omega \subset \mathbb{R}^2$:

$$-\Delta u = f \text{ in } \Omega, \tag{2.51}$$

with Dirichlet boundary conditions:

$$u = 0 \text{ on } \partial\Omega. \tag{2.52}$$

To derive the weak formulation, we need to multiply the Poisson's equation on a test function v and integrate over the computational domain Ω:

$$\int_\Omega (-\Delta u) v dx = \int_\Omega f v dx. \tag{2.53}$$

Applying integration by parts and using the boundary condition $u = 0$ on $\partial\Omega$, we obtain:

$$\int_\Omega \nabla u \cdot \nabla v dx = \int_\Omega f v dx. \tag{2.54}$$

The weak formulation of the problem is to find u. With this form, we can now discretize the domain and solve the problem using the FEM.

2.3.4 FreeFem++ and Mesh

The FEM is implemented in the open-source platform FreeFem++ for solving PDE [Hecht, 2012]. FreeFem++ is written in C++ and developed and maintained by Université Pierre et Marie Curie and Laboratoire Jacques-Louis Lions. I performed all the numerical simulations presented in this manuscript using FreeFem++. The final step of this chapter will be to introduce the mesh of the problem. I used a triangular mesh for the simulations, which is the most common type typically employed in FEM. The mesh is generated using the built-in mesh generator in FreeFem++. Figure 2.3 presents the mesh of the system.

The figure here presents the smallest mesh resolution with 40000 triangles. All the results presented in the following chapters are obtained with a much higher number of triangles, around 200000, except for cases comparing different mesh resolutions. This choice of mesh balances computational time with the desired accuracy. We also note that we produce the mesh with P1 elements, which are linear elements. The selection of P1 elements is made to simplify the calculations and to reduce the computational time, even though FreeFem++ supports higher-order elements. We verified that the results obtained with P1 elements correspond to those obtained with P2 elements, which are quadratic elements, and P1b elements, which are linear elements with bubble functions. However, the computational time is significantly reduced with P1 elements, so all the simulations in the thesis are performed with P1 elements.

2.3.5 Newton–Raphson method

As we have defined the mesh, we need to establish the numerical method; in our case, it is the Newton-Raphson method. For a non-linear equation $f(x) = 0$, we can use an iterative formula to approximate the root:

$$x_{n+1} = x_n - \frac{f(x_n)}{f'(x_n)}, \tag{2.55}$$

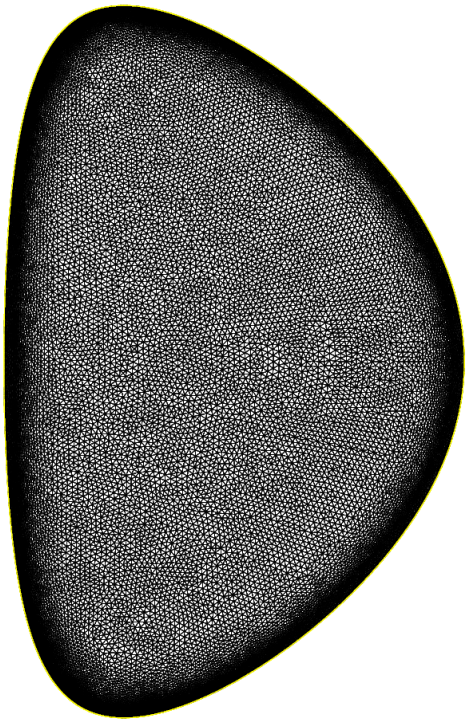

Figure 2.3: Triangular mesh of the domain Ω generated with FreeFem++ with 40000 triangles. Mesh is adapted to have a higher density of triangles near the boundary.

where x_n is the current approximation and $f'(x_n)$ is the derivative of the function at x_n.

This method assumes that the function $f(x)$ can be approximated by a linear function around the current estimate, and the following estimate is obtained by finding the root of this linear function. Let us consider a simple example to illustrate the Newton-Raphson method. Let us look at the non-linear equation $f(x) = x^2 - 2 = 0$. The derivative of the function is $f'(x) = 2x$. Starting with an initial guess $x_0 = 1$, we can apply the Newton-Raphson iteration as follows:

$$
\begin{aligned}
x_1 &= x_0 - \frac{f(x_0)}{f'(x_0)} = 1 - \frac{1-2}{2} = 1.5, \\
x_2 &= x_1 - \frac{f(x_1)}{f'(x_1)} \approx 1.4167, \\
x_3 &\approx 1.4142.
\end{aligned}
$$

After just a few iterations, the method converges to the approximate root of the equation $f(x) = 0$, which is $x \approx 1.4142$.

In our system, this method requires calculating $f'(x)$ for each equation in the system (2.44)-(2.49) and the initial guess is set as $u = 1$ for all variables.

In iterative methods like the Newton-Raphson method, it is essential to define a stopping criterion to decide when the process has converged sufficiently close to the actual root. This is typically done using a tolerance parameter ϵ. For all our calculations, we use $\epsilon = 10^{-10}$, which means that the iterative process will stop when the absolute difference between successive approximations $|x_{n+1} - x_n|$ is less than 10^{-10}.

2.3.6 First numerical results

We now present the first numerical results with the necessary elements in place. By solving the system of equations (2.44)-(2.49) and by applying boundary conditions from 2.3.1 with typical JET parameters, we can compute the steady-state toroidal velocity fields. Figure 3.1 depicts the computed toroidal velocity for two different Hartmann numbers: $H = 10$ and $H = 10^5$ at a given resistivity η.

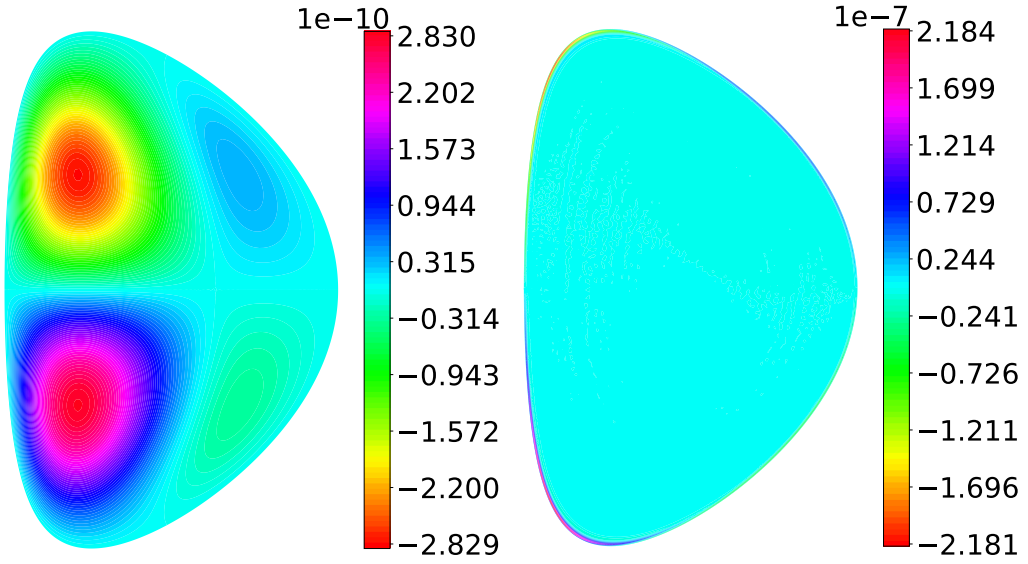

Figure 2.4: Toroidal velocity field computed with the FEM using FreeFem++ with P1 elements for $H = 10$ (on the left) and $H = 10^5$ (on the right) in JET geometry with no-slip boundary condition for toroidal velocity.

In the simulations, we vary the Hartmann number, which with fixed resistivity η means that we vary the viscosity ν value. We typically start with $H = 1$ and find a solution for each H by iterating through the Newton-Raphson method. Figure 2.5 presents the root-mean-square of the toroidal velocity field in Alfvén velocity units as a function of the Hartmann number. By root-mean-square here, we mean spatial average on the cross-section plasma domain Ω of the velocity field, which

is calculated as

$$< v >_{rms} = \left(\frac{\int_\Omega v^2 ds}{\int_\Omega ds} \right)^{1/2} . \tag{2.56}$$

The figure also illustrates the typical data points collected throughout the simulation process.

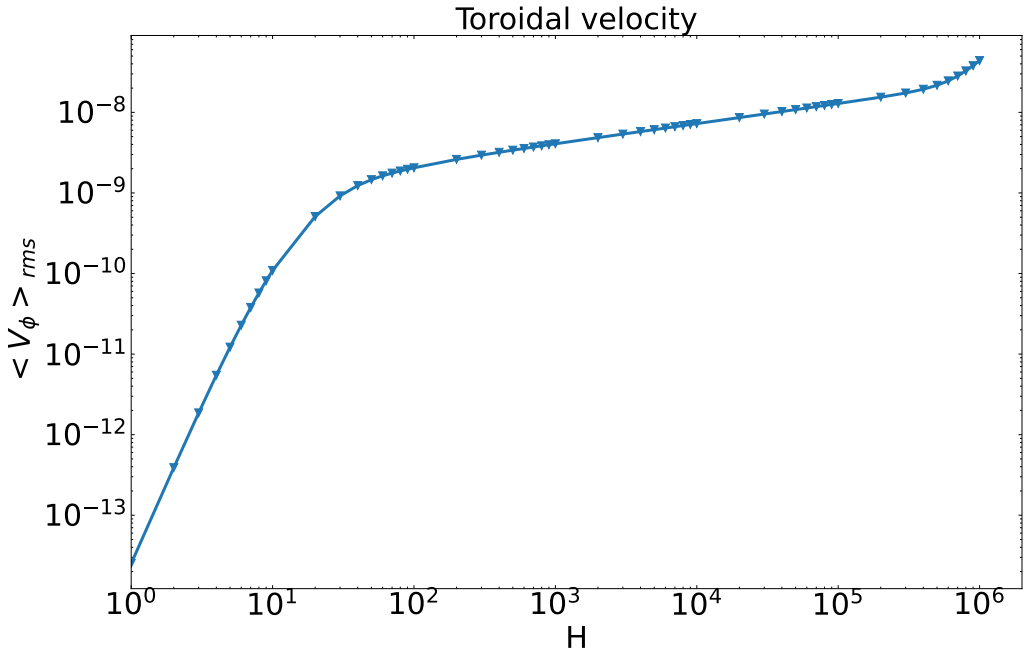

Figure 2.5: Root-mean-square of the toroidal velocity field in Alfvén velocity units as a function of the Hartmann number in log-log scale with no-slip boundary condition for toroidal velocity.

2.3.7 Computational time

The simulations were conducted on personal computers, using the central processing unit (CPU) for calculations. The computer efficiency, mesh resolution, and complexity of the problem influence the computational time. A typical run takes about one day to complete for the simulations performed in this thesis. However, simulations can take several days with the finest mesh (200000 triangles) and complex problems. Simulations are stopped when the Newton-Raphson method fails to converge within the maximum allowed iterations (around 200).

2.4 Summary

In this chapter, we have derived the system of axisymmetric steady-state equations that will be used to simulate the plasma. It introduced the computational domain and boundary conditions, followed by a detailed discussion of the numerical methods employed: the finite element method, weak formulation, mesh generation using FreeFem++, the Newton-Raphson method, and the first results. With this being said, we are now ready to present the results of the simulations in the following chapters.

Bibliography

Hecht, F. (2012). New development in FreeFem++. *Journal of Numerical Mathematics*, 20(3-4):251–265, DOI: 10.1515/jnum-2012-0013.

Holst, M., Kungurtsev, V., and Mukherjee, S. (2022). A note on optimal tokamak control for fusion power simulation. *arXiv e-prints*, (arXiv:2211.08984):arXiv:2211.08984, DOI: 10.48550/arXiv.2211.08984.

JET Team (1992). Fusion energy production from a deuterium-tritium plasma in the jet tokamak. *Nuclear Fusion*, 32(2):187, DOI: 10.1088/0029-5515/32/2/I01, https://dx.doi.org/10.1088/0029-5515/32/2/I01.

Kamp, L. P. and Montgomery, D. C. (2003). Toroidal flows in resistive magnetohydrodynamic steady states. *Physics of Plasmas*, 10:157–167, DOI: 10.1063/1.1524629.

Kamp, L. P., Montgomery, D. C., and Bates, J. W. (1998). Toroidal flows in resistive magnetohydrodynamic steady states. *Physics of Fluids*, 10(7):1757–1766, ISSN: 1070-6631, DOI: 10.1063/1.869692.

Krupka, A. and Firpo, M.-C. (2024). Scaling laws of the plasma velocity in visco-resistive magnetohydrodynamic systems. *Fundamental Plasma Physics*, 10:100044, ISSN: 2772-8285, DOI: 10.1016/j.fpp.2024.100044.

Morales, J. A., Bos, W. J. T., Schneider, K., and Montgomery, D. C. (2012). Intrinsic rotation of toroidally confined magnetohydrodynamics. *Physical Review Letters*, 109(17):175002, DOI: 10.1103/PhysRevLett.109.175002.

Oueslati, H., Bonnet, T., Minesi, N., Firpo, M.-C., and Salhi, A. (2019). Numerical derivation of steady flows in visco-resistive magnetohydrodynamics for JET and ITER-like geometries with no symmetry breaking. *AIP Conference Proceedings*, 2179:020009, DOI: 10.1063/1.5135482.

Oueslati, H. and Firpo, M.-C. (2020). Breaking up-down symmetry with magnetic perturbations in tokamak plasmas: Increase of axisymmetric steady-state velocities. *Physics of Plasmas*, 27(10):102501, DOI: 10.1063/5.0016566.

Roverc'h, E., Oueslati, H., and Firpo, M.-C. (2021). Steady-state flows in a visco-resistive magnetohydrodynamic model of tokamak plasmas with inhomogeneous heating. *Journal of Plasma Physics*, 87(2):905870217, DOI: 10.1017/S0022377821000313.

Chapter 3

Scaling laws of the plasma velocity

The best way to predict the future is to invent it.

Alan Kay

Contents

3.1 Introduction

Plasma rotation plays a vital role in the heat and particle confinement properties of the tokamak. Understanding and controlling plasma rotation is a crucial research objective towards magnetic confinement. This chapter will be devoted to understanding the plasma rotation and its scaling laws in the context of a visco-resistive magnetohydrodynamic system. In Chapter 2, we proposed a step-by-step

derivation of the dimensionless closed system of PDE to model tokamak plasmas within a MHD visco-resistive setting. Following the derivation of this system, coupling the steady-state Maxwell equations to the steady-state Navier-Stokes equation with Ohm's law closure, we focus on the behaviour of the system for a constant toroidal current drive. In Section 3.2, we derive a scaling law for the velocity that is expected to be valid as long as the magnitude of the inertial $\boldsymbol{\omega} \times \mathbf{v}$ term is small enough. This prediction is tested on numerical simulations in Sections 3.3 and 3.4. A conclusive Section 3.5 summarizes the outcomes of this chapter.

3.2 Behaviour of the plasma velocity

Let us now focus on the behaviour of plasma velocity within a visco-resistive MHD setting. In the present study, we consider the axisymmetric steady-states of the (dimensionless) Navier-Stokes equation

$$\boldsymbol{\omega} \times \mathbf{v} = -\nabla p^* + \mathbf{j} \times \mathbf{b} + \nu \nabla^2 \mathbf{v}, \tag{3.1}$$

self-consistently satisfying the steady-state Maxwell equations with Ohm's law coupling

$$\mathbf{E} + \mathbf{v} \times \mathbf{b} = \eta \mathbf{j}. \tag{3.2}$$

In magnetic confinement fusion, resistivity η and viscosity ν are two small parameters. Combining the Equations (3.1) and (3.2) yields

$$\boldsymbol{\omega} \times \mathbf{v} = -\nabla p^* + \left(\frac{\mathbf{E}}{\eta} + \eta^{-1} \mathbf{v} \times \mathbf{b} \right) \times \mathbf{b} + \nu \nabla^2 \mathbf{v}. \tag{3.3}$$

Let us put velocity to be $\mathbf{v} = (\eta/\nu)^{1/2} \, \widetilde{\mathbf{v}}$ and, consistently, vorticity then $\boldsymbol{\omega} = (\eta/\nu)^{1/2} \, \widetilde{\boldsymbol{\omega}}$. By making this change of variable, Equation (3.3) becomes

$$\frac{\eta}{\nu} \widetilde{\boldsymbol{\omega}} \times \widetilde{\mathbf{v}} = -\nabla p^* + \left(\frac{\mathbf{E}}{\eta} + (\eta\nu)^{-1/2} \, \widetilde{\mathbf{v}} \times \mathbf{b} \right) \times \mathbf{b} + (\eta\nu)^{1/2} \, \nabla^2 \widetilde{\mathbf{v}}. \tag{3.4}$$

Using the Hartmann number, H, defined as $H = (\eta\nu)^{-1/2}$, this reads

$$\eta^2 H^2 \widetilde{\boldsymbol{\omega}} \times \widetilde{\mathbf{v}} = -\nabla p^* + \left(\frac{\mathbf{E}}{\eta} + H \widetilde{\mathbf{v}} \times \mathbf{b} \right) \times \mathbf{b} + H^{-1} \nabla^2 \widetilde{\mathbf{v}}. \tag{3.5}$$

The pressure term can be eliminated by taking the curl of the equation. Let us discuss this equation for a given drive $\mathbf{E}/\eta$. *If* we can neglect the left-hand side inertial term in Equation (3.5), then we are left with

$$\nabla \times \left[\left(\frac{\mathbf{E}}{\eta} + H \widetilde{\mathbf{v}} \times \mathbf{b} \right) \times \mathbf{b} + H^{-1} \nabla^2 \widetilde{\mathbf{v}} \right] = \mathbf{0} \tag{3.6}$$

and, at given $\mathbf{E}/\eta$, plasma velocity $\widetilde{\mathbf{v}}$ must be a function of H only, meaning that $\mathbf{v}/\eta = H\widetilde{\mathbf{v}}$ is a function of H only. This prevalence of the Hartmann number was

already inferred in the Reverse Field Pinch [Cappello and Escande, 2000], where visco-resistive MHD simulations showed that the Hartmann number controls the transition from multiple to quasi-single helicity states. Section 3.3 will be devoted to the numerical exploration of $\mathbf{v}/\eta$ dependence on H only and its validity domain. Using different values of the resistivity η while keeping constant the drive $\mathbf{E}/\eta$, any change of behaviour in the form of the components of $\mathbf{v}/\eta$, if non-numerical, might be considered as a signal of the onset of non-linear effects.

Let us briefly consider the neutral fluid case to discuss the onset of inertial effects in Equation (3.5). If we introduce the Reynolds number, R_e, as the ratio between the order of magnitude of the inertial over the viscous forces and assume that the characteristic length of the variation of $\mathbf{v}$ is r_0, then we have

$$R_e = \eta H^2 v. \tag{3.7}$$

To fix ideas, let us remind you that, in a circular pipe, the usual (neutral) fluid turbulence sets in for $R_e \geq R_{ec} \simeq 3.10^3$. Consequently, if we take the fusion relevant value $\eta = 10^{-8}$, this (qualitative) threshold would be attained for a velocity Mach number as large as $v_c = 0.3$ at $H = 10^6$, or as low as $v_c = 0.3 \times 10^{-4}$ if $H = 10^8$. This could be an incentive to estimate viscosity better, and thus the Hartmann number, in magnetized plasma flows. However, in the case of a tokamak plasma, the initiation of inertial effects is anticipated to be much different as it is governed by its balance with the Laplace force rather than the dissipative force.

3.3 Preliminary results

Now, let us look at the numerical results for our system. The simulations shown in Figures 3.1, 3.2 and 3.3 admit a toroidal no-slip boundary condition for the toroidal velocity and a constant ratio E_0/η of order 1. First, let us consider the toroidal velocity distribution on the cross-section plasma domain: Figure 3.1 depicts the computed steady-state toroidal velocity fields for two different Hartmann numbers: $H = 10$ and $H = 10^5$ at a given resistivity η. It can be seen on the left that at low Hartmann number H so that the viscosity of the system ν is very high, the toroidal velocity develops structures that seem segmented into distinct zones. Here, the dominant force is viscous, which homogenizes the velocity across the plasma. However, at a high Hartmann number on the right, the plasma becomes more sensitive to the magnetic force that causes the formation of the boundary layer.

In Figures 3.2 and 3.3, the root-mean-squares of the toroidal and poloidal velocity fields are computed for different resistivity values. It seems that the numerical results can be separated into three distinct "regimes". The first regime is in the limit of small Hartmann numbers $H \ll 1$; it finishes at around $H \approx 10$. The second regime starts around $H \approx 80$ and remains across almost all Hartman numbers until $H \approx 10^5$. The third regime appears to begin at $H \approx 10^6$; however, it never starts at the upper curve with η=6.9e-5. The behaviour of the plasma

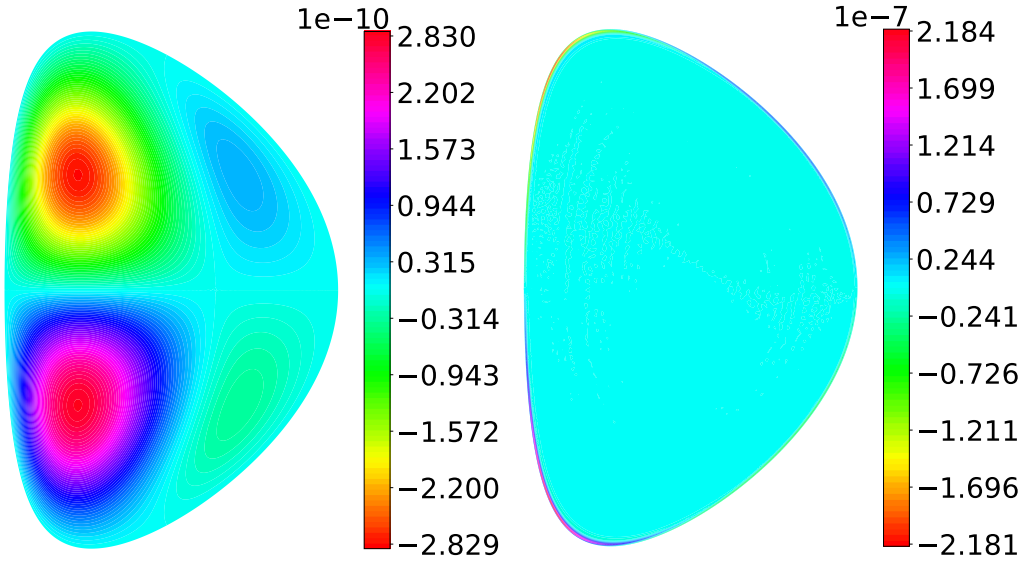

Figure 3.1: Toroidal velocity field for $H = 10$ (on the left) and $H = 10^5$ (on the right) in JET geometry with no-slip boundary condition for toroidal velocity with η=6.9e-9 and $E_0/\eta = 0.43$.

velocity in the third regime needs to be investigated thoroughly. This section will discuss the third regime and its validity in detail.

The log-log plots of Figures 3.2 and 3.3 demonstrate that at a given E_0/η ratio, the velocity is proportional to the resistivity and some function depending solely on the Hartmann number. If we normalize each velocity curve on each resistivity η value, we would see a single curve at the first and the second regime. However, the emergence of a third regime at H-values above 10^6, resulting in slight variations of the velocity behaviour for different resistivity values, suggests that non-linear effects may be increasingly significant. In all the figures, the plotted results are, by default, those obtained with the highest resolution (the maximum number of triangles). Let us now verify how the systems behave with variation on the mesh. Figure 3.4 illustrates the evolution of numerical results as a function of the number of triangles used, N. It appears that the results depend on the mesh for values of the Hartmann number beyond 10^6. This is easily interpreted in light of the large-H cross-section plots of the toroidal velocity field (see Figure 3.1).

To obtain robust results, it is necessary to finely resolve the boundary layer appearing at the edge of the domain that characterizes this second regime. With $N = 163508$ triangles, we are approaching the maximum accessible resolution. It is probable, but not certain, based on the simulations in Figure 3.4, that the end of the scaling law of the second regime is a numerical artifact due to a resolution deficiency.

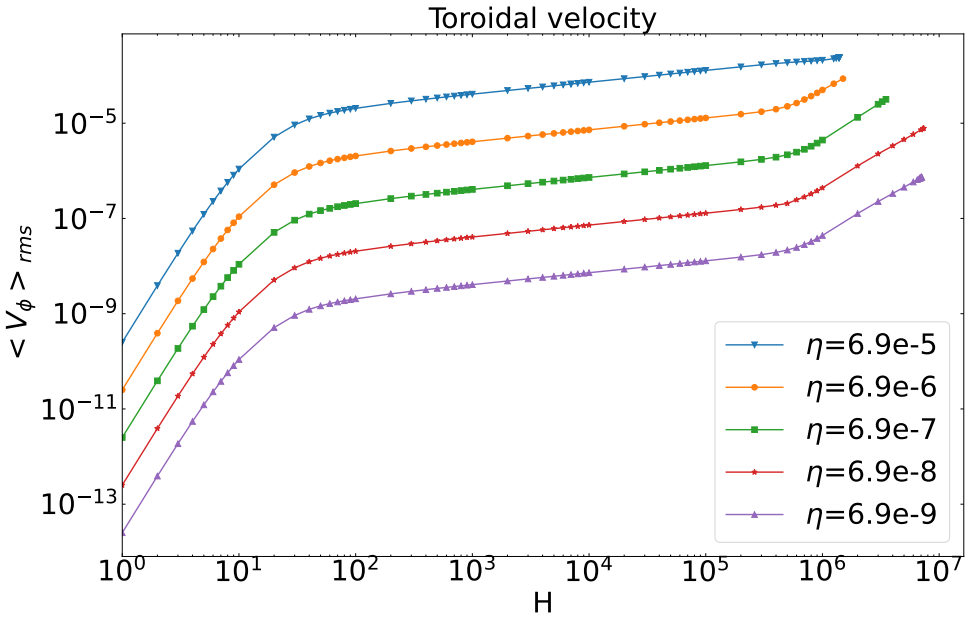

Figure 3.2: Root-mean-square of the toroidal velocity field in Alfvén velocity units as a function of the Hartmann number in log-log scale for different values of the resistivity with no-slip boundary condition for toroidal velocity with $E_0/\eta = 0.43$.

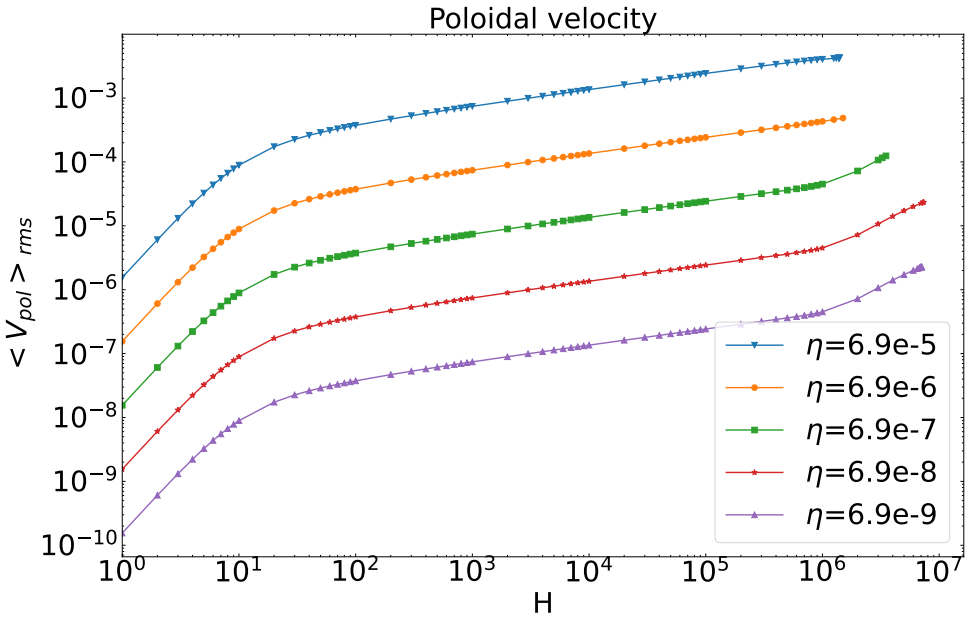

Figure 3.3: Root-mean-square of the poloidal velocity field in Alfvén velocity units as a function of the Hartmann number in log-log scale for different values of the resistivity with no-slip boundary condition for toroidal velocity with $E_0/\eta = 0.43$.

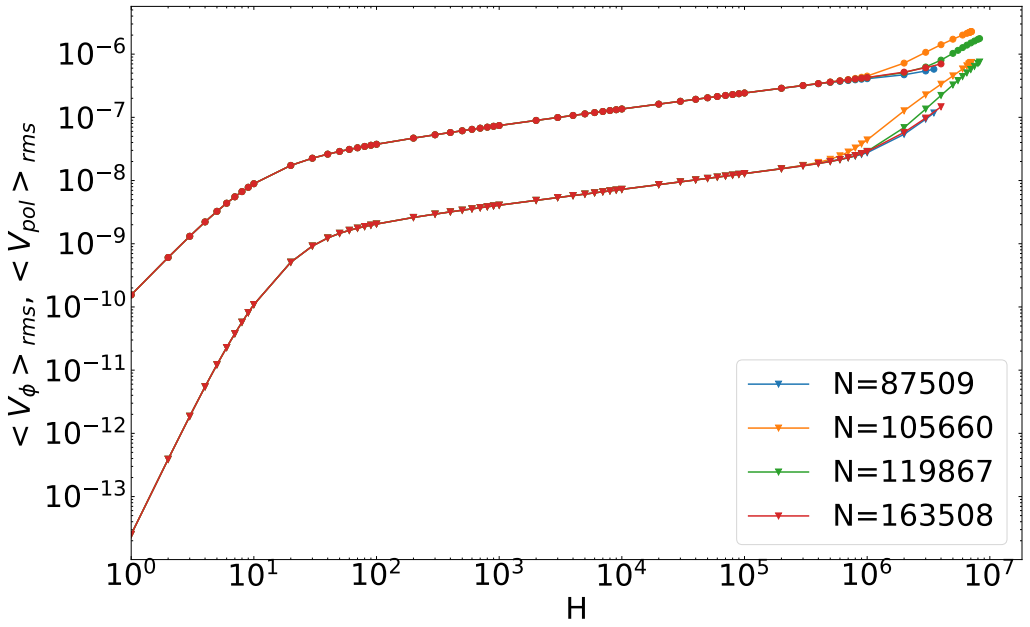

Figure 3.4: Root-mean-square of toroidal and poloidal velocities as a function of the Hartmann number in Alfvén velocity units with η=6.9e-9 for different numbers of triangles with no-slip boundary condition for toroidal velocity.

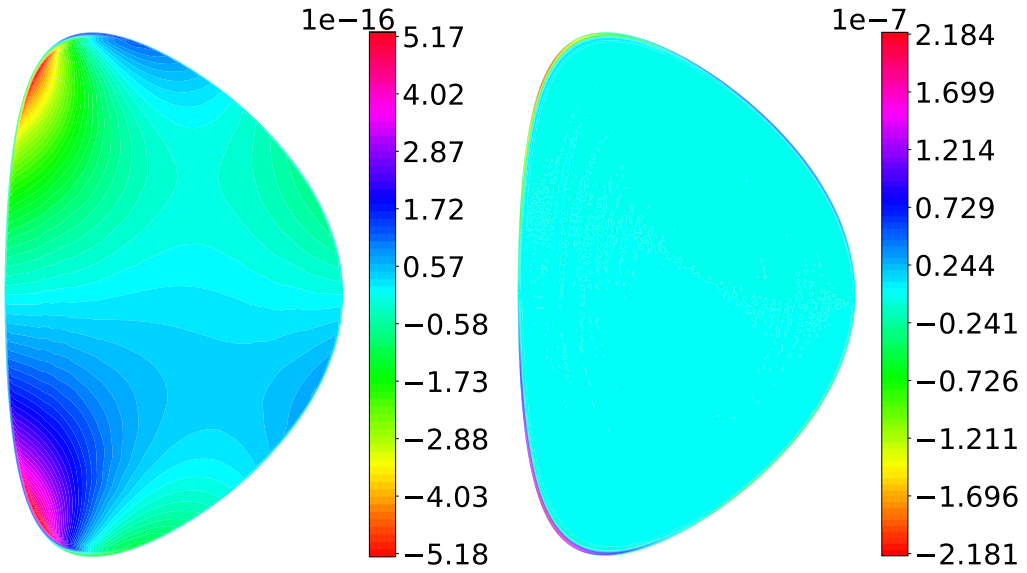

Figure 3.5: Contribution of $(\boldsymbol{\omega} \times \mathbf{v}) \cdot \mathbf{i}_\varphi$ term (on the left) and $(\mathbf{j} \times \mathbf{b}) \cdot \mathbf{i}_\varphi$ term (on the right) to the total toroidal velocity for $H = 10^5$.

To verify if inertial effects could be involved in this regime shift at high Hartmann numbers, let us quantify the impact of the non-linear term on the overall velocity. In Figure 3.5, we depict the contributions of the $(\boldsymbol{\omega} \times \mathbf{v}) \cdot \mathbf{i}_\varphi$ and $(\mathbf{j} \times \mathbf{b}) \cdot \mathbf{i}_\varphi$ terms to the total toroidal velocity in Equation (2.36) for $H = 10^5$. Here, two assumptions are made: firstly, we set the $(\mathbf{j} \times \mathbf{b}) \cdot \mathbf{i}_\varphi$ term to zero. Consequently, Equation (2.37) is modified to

$$\hat{\nu}\hat{\triangle}^* \tilde{u}_4 = \frac{1}{x}\{\tilde{u}_1, \tilde{u}_4\} \tag{3.8}$$

Similarly, for the distribution on the right in Figure 3.5, we make a similar assumption, but this time for the non-linear term

$$\hat{\nu}\hat{\triangle}^* \tilde{u}_4 = \frac{1}{x}\{\tilde{u}_3, \tilde{u}_5\} \tag{3.9}$$

It is worth noting that, even for high Hartmann numbers, the non-linear term is observed to be significantly smaller than the $(\mathbf{j} \times \mathbf{b}) \cdot \mathbf{i}_\varphi$ term. The distribution on the right in Figure 3.5 precisely corresponds to the toroidal velocity in Figure 3.1, indicating that the non-linear term's contribution to the total velocity is negligible. Figure 3.6 shows a comparison of the toroidal and poloidal parts of $\boldsymbol{\omega} \times \mathbf{v}$ and $\mathbf{j} \times \mathbf{b}$ terms as a function of the Hartmann number. Expressing these terms in new variables, the toroidal part of $\boldsymbol{\omega} \times \mathbf{v}$ becomes $\{u_1, u_4\}/x^2$, while the poloidal part is given by $u_2 \nabla u_1/x^2 - u_4 \nabla u_4/x^2$. Similarly, for $\mathbf{j} \times \mathbf{b}$, the toroidal component is $\{u_5, u_3\}/x^2$, and the poloidal one is $-u_3 \nabla u_3/x^2 + u_6 \nabla u_5/x^2$. It can be seen that the non-linear term grows with the increase of the Hartmann number, yet it remains sufficiently small not to impact the total toroidal and poloidal velocity. We conclude that the third regime is numerical.

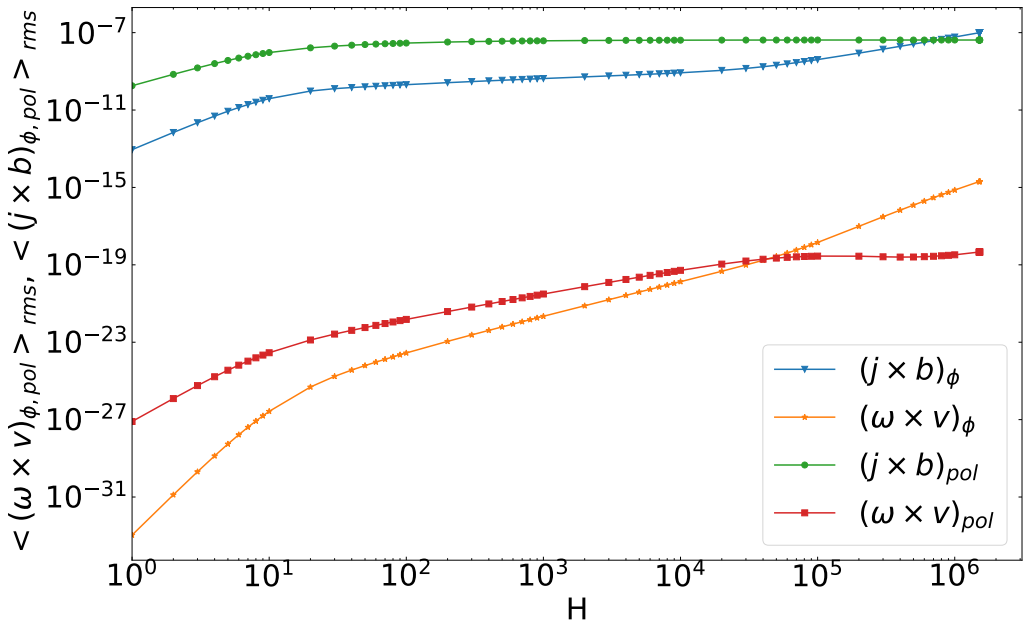

Figure 3.6: Root-mean-square of toroidal and poloidal parts of $\boldsymbol{\omega} \times \mathbf{v}$ and $\mathbf{j} \times \mathbf{b}$ terms as a function of the Hartmann number in Alfvén velocity v_{A0} units with η=6.9e-9.

3.4 Scaling laws

3.4.1 Prediction of the scaling laws with $H \ll 1$ and $H \gg 1$

Here, we would like to shift our focus to the first and second regimes and predict their scaling laws. The scaling of velocity in the first regime where $H \ll 1$ can be deduced analytically and is already documented in the literature [Kamp et al., 1998]. According to [Kamp et al., 1998; Kamp and Montgomery, 2003], the toroidal velocity in this limit scales with H^4 while the poloidal velocity scales with H^2. A detailed derivation of the velocities scaling laws is presented in Appendix C.

As depicted in Figure 3.1, the second regime exhibits a distinct boundary layer that becomes thinner with the increase of the Hartmann number. It is necessary to consider the boundary layer equations to predict the velocity behaviour in this regime where $H \gg 1$ while the effects of inertial terms remain negligible. We aim to estimate the boundary layer thickness δ as a function of the Hartmann number, denoted as $\delta = \delta(H)$. We start from Equation (3.5), at a given $\mathbf{E}/\eta$ and by neglecting the inertial term we have

$$-\mathbf{j} \times \mathbf{b} = -\nabla p^* + H^{-1} \nabla^2 \tilde{\mathbf{v}}. \tag{3.10}$$

Using $\mathbf{j} \times \mathbf{b} = (\mathbf{b} \cdot \nabla)\mathbf{b} - \nabla(b^2/2)$, Equation (3.10) takes the form

$$-(\mathbf{b} \cdot \nabla)\mathbf{b} = -\nabla \widetilde{p}^* + H^{-1}\nabla^2 \widetilde{\mathbf{v}} \tag{3.11}$$

where $\widetilde{p}^* = p^* + b^2/2$. To facilitate the writing of equations within the boundary layer, we introduce a new coordinate system in which the plasma boundary $\partial\Omega$ aligns with the y-axis while x denotes the transverse direction. We introduce the characteristic length, L, in the y-direction and the boundary layer thickness δ in the x-direction ($\delta \ll L$) (see Figure 3.7). V_c and B_c represent the characteristic

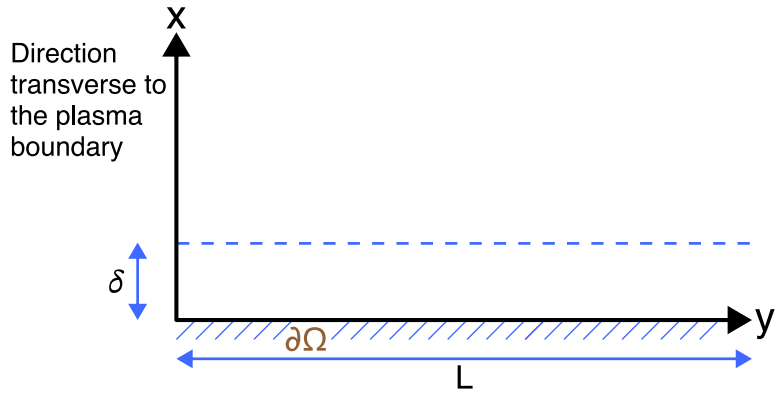

Figure 3.7: Sketch of the slab geometry used in the boundary layer equations.

plasma speed and magnetic field along y. Let $\widetilde{v}_x$ and $\widetilde{v}_y$ denote the velocity components in the x and y directions respectively, and b_x and b_y the magnetic field components. From Equation (3.11) we derive

$$-b_x \frac{\partial b_x}{\partial x} - b_y \frac{\partial b_x}{\partial y} = -\frac{\partial \widetilde{p}^*}{\partial x} + H^{-1}\left(\frac{\partial^2 \widetilde{v}_x}{\partial x^2} + \frac{\partial^2 \widetilde{v}_x}{\partial y^2}\right), \tag{3.12}$$

$$-b_x \frac{\partial b_y}{\partial x} - b_y \frac{\partial b_y}{\partial y} = -\frac{\partial \widetilde{p}^*}{\partial y} + H^{-1}\left(\frac{\partial^2 \widetilde{v}_y}{\partial x^2} + \frac{\partial^2 \widetilde{v}_y}{\partial y^2}\right), \tag{3.13}$$

where, in Equation (3.13), we can anticipate that the pressure gradient along y is negligible. By assuming $\widetilde{v}_y \sim V_c$, $y \sim L$, $x \sim \delta$, $b_y \sim B_c$, we estimate $\widetilde{v}_x$ from the incompressibility condition

$$\frac{\partial \widetilde{v}_x}{\partial x} + \frac{\partial \widetilde{v}_y}{\partial y} = 0 \tag{3.14}$$

and similarly b_x from the zero-divergence of the magnetic field

$$\frac{\partial b_x}{\partial x} + \frac{\partial b_y}{\partial y} = 0 \tag{3.15}$$

as $\widetilde{v}_x \sim \delta V_c/L$ and $b_x \sim \delta B_c/L$. Now the Equation (3.13) yields

$$\frac{B_c^2}{L} + \frac{B_c^2}{L} \sim H^{-1}\frac{V_c}{\delta^2} + H^{-1}\frac{V_c}{L^2}. \tag{3.16}$$

The largest viscous term should be comparable in magnitude to the left-hand terms, that is

$$\frac{B_c^2}{L} \sim H^{-1}\frac{V_c}{\delta^2} \tag{3.17}$$

which gives the boundary layer thickness scaling with Hartmann number as

$$\delta \sim \frac{1}{\sqrt{H}}. \tag{3.18}$$

Let us note that this is in agreement with the numerical estimate of the boundary layer thickness obtained in [Kamp and Montgomery, 2004] as a function of the viscosity as $\delta \sim \nu^{1/4}$ (assuming there η constant). Let us now estimate the behaviour of the velocity root-mean-square with the Hartmann number. Let us focus on the velocity $\widetilde{v}$ in the poloidal direction. By definition, its root-mean-square is

$$< \widetilde{v}_{pol} >_{rms} = \left(\frac{\int_\Omega \widetilde{v}_{pol}^2 ds}{\int_\Omega ds} \right)^{1/2}. \tag{3.19}$$

In the boundary layer (BL), using the expression of the poloidal velocity in terms of the stream function (2.26) yields $\widetilde{v}_{pol}^{BL} \sim H/(\eta\delta)$. At the same time, in the rest of the plasma, the contribution of the transverse gradient should be of order one yielding $\widetilde{v}_{pol}^{core} \sim H/(\eta\delta)$. This yields

$$\int_\Omega \widetilde{v}_{pol}^2 ds = \int_{BL} \widetilde{v}_{pol}^2 ds + \int_{\Omega core} \widetilde{v}_{pol}^2 ds \sim \frac{L\delta H^2}{\eta^2\delta^2} + \frac{L^2H^2}{\eta^2} \sim \frac{LH^2}{\eta^2\delta}. \tag{3.20}$$

Consequently, $< \widetilde{v}_{pol} >_{rms} \sim H/\eta\delta^{-1/2}$, so that in the original velocity variable and using (3.18), one obtains the scaling

$$< v_{pol} >_{rms} \sim \eta H^{1/4}. \tag{3.21}$$

The root-mean-square of the toroidal velocity should follow the same scaling as the poloidal velocity because poloidal and toroidal components are interchangeable from the perspective of the boundary layer analysis and can both align with the y-axis of Figure 3.7. By this argument, we can conclude that $< v_{pol} >_{rms}$ and $< v_\phi >_{rms}$ scales with $\eta H^{1/4}$ for $H \gg 1$. Finally, we have used the incompressibility assumption in Equation (3.14) to derive this scaling law so that we do not expect these results to be transferable to the case of compressible flow.

3.4.2 Numerical estimation of the scaling laws

Let us estimate the scaling laws of the velocity in these two regimes by using a power-law fitting. In Figure 3.8, it can be seen that in the limit, as the Hartmann number H approaches zero for the first regime, the velocity follows the pattern $\eta f(H)$, with f approximately equal to H^4 for toroidal velocity and H^2 for poloidal velocity. The velocities scale as $H^{1/4}$ in the second regime. It corresponds to the analytical predictions made in Section 3.4.1.

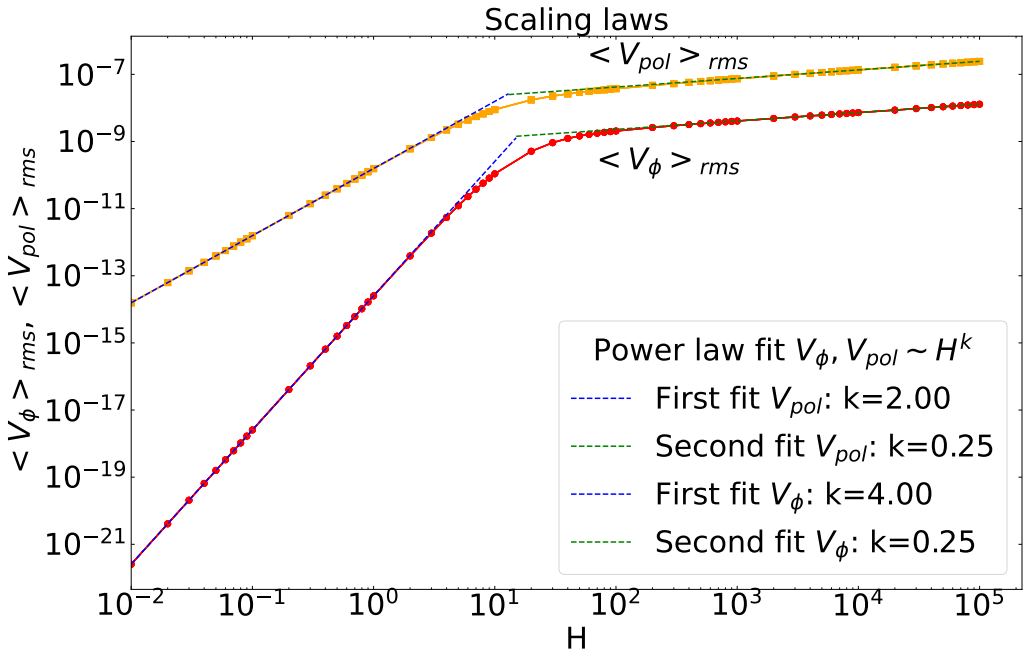

Figure 3.8: Root-mean-square of toroidal and poloidal velocities in Alfvén velocity units as a function of the Hartmann number in log-log scale with power-law fitting curves.

3.4.3 Effect of boundary conditions

It is necessary to investigate the impact of the boundary conditions on the scaling laws. To do so, let us take a closer look at the behaviour of the toroidal velocity field with different boundary conditions: Figure 3.9 presents the same as Figure 3.1 for $H = 10$ and $H = 10^4$ but with the "free-slip" boundary conditions for the toroidal velocity ($\partial_n(u_4/r^2) = 0, u_2 = 0$). Figure 3.10 presents the application of Neumann $\partial_n(u_4/x) = 0, u_2 = 0$ boundary conditions and finally Figure 3.11 illustrates the zero normal derivative of the toroidal velocity and vorticity ($\partial_n(u_4/x) = \partial_n(u_2/x) = 0$) boundary conditions.

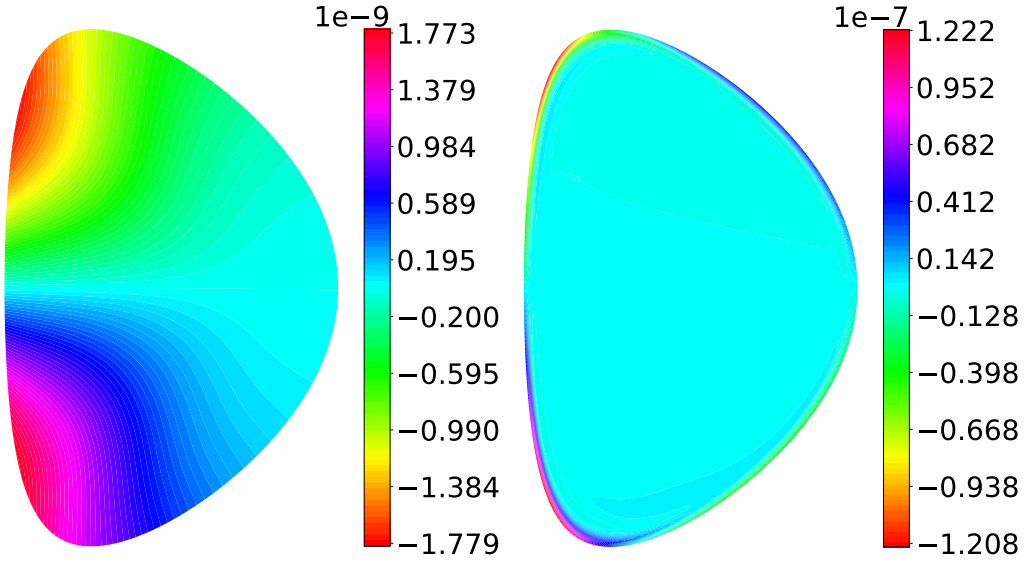

Figure 3.9: Toroidal velocity field computed with the FEM using FreeFem++ with P1 elements for $H = 10$ (on the left) and $H = 10^4$ (on the right) in JET geometry with free-slip boundary condition for toroidal velocity with η=6.9e-9 and E_0=3e-9.

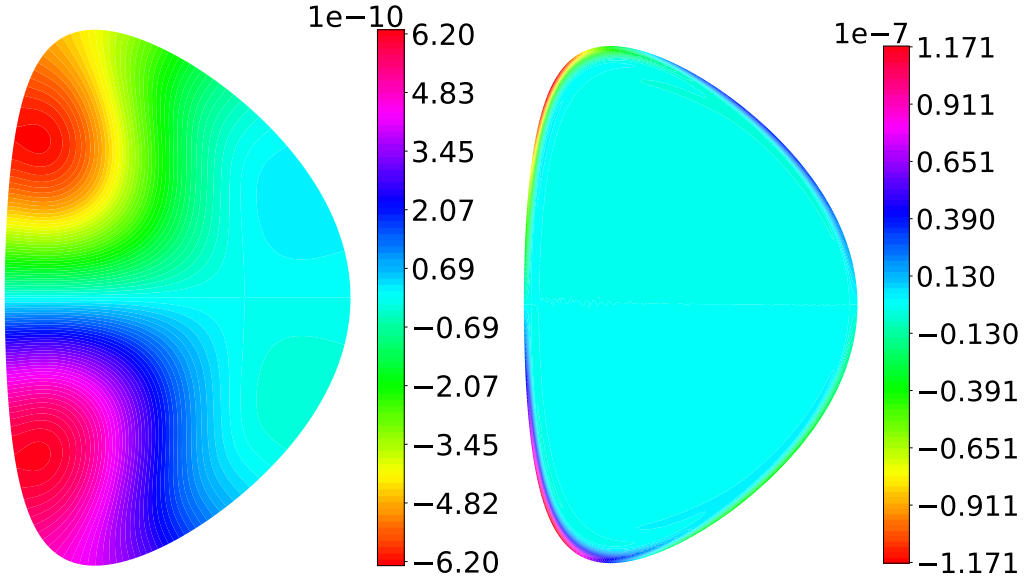

Figure 3.10: Toroidal velocity field computed with the FEM using FreeFem++ with P1 elements for $H = 10$ (on the left) and $H = 10^4$ (on the right) in JET geometry with $\partial_n(u_4/x) = 0, u_2 = 0$ boundary conditions with η=6.9e-9 and E_0=3e-9.

At all this variation of the boundary conditions, velocity distribution also slightly varies, especially at small Hartmann numbers. In the case of big Hartmanns, velocities still develop a boundary layer, which seems almost the same as in the case of no-slip boundary conditions. Let us now look at the root-mean-square to verify the behaviour of the plasma velocity under the different boundary conditions. In Figure 3.12, we compare the diverse boundary conditions described above in Section 2.3.1, applied to the toroidal velocity and vorticity. To facilitate interpretation, we have normalized the root-mean-square of the toroidal velocity field for the corresponding resistivity values. Notably, this normalization leads to the convergence of the curves across the resistivity values.

It can be seen that the scaling law for the toroidal velocity in the first regime of small Hartmanns remains consistent; the scaling law in the second regime of big Hartmanns slightly varies with the application of different boundary conditions. Yet, this variation is slight enough to state that the scaling maintains the same order. The characteristics of the first and second slopes now reveal that, at a fixed E_0/η ratio, the velocity is dependent on the Hartmann number only, and this scaling remains even when considering different boundary conditions.

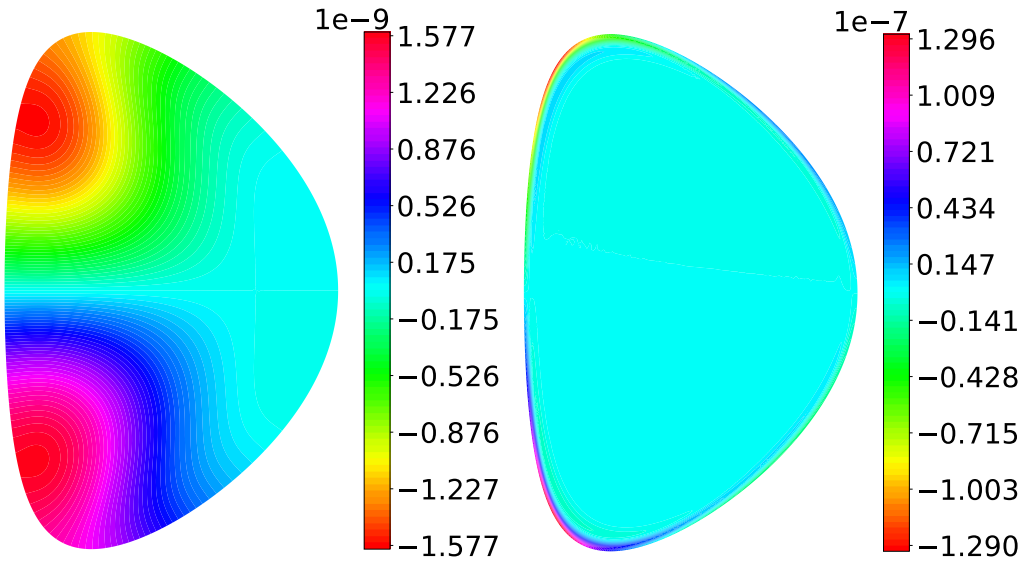

Figure 3.11: Toroidal velocity field computed with the FEM using FreeFem++ with P1 elements for $H = 10$ (on the left) and $H = 10^4$ (on the right) in JET geometry with $\partial_n(u_4/x) = \partial_n(u_2/x) = 0$ boundary conditions with η=6.9e-9 and E_0=3e-9.

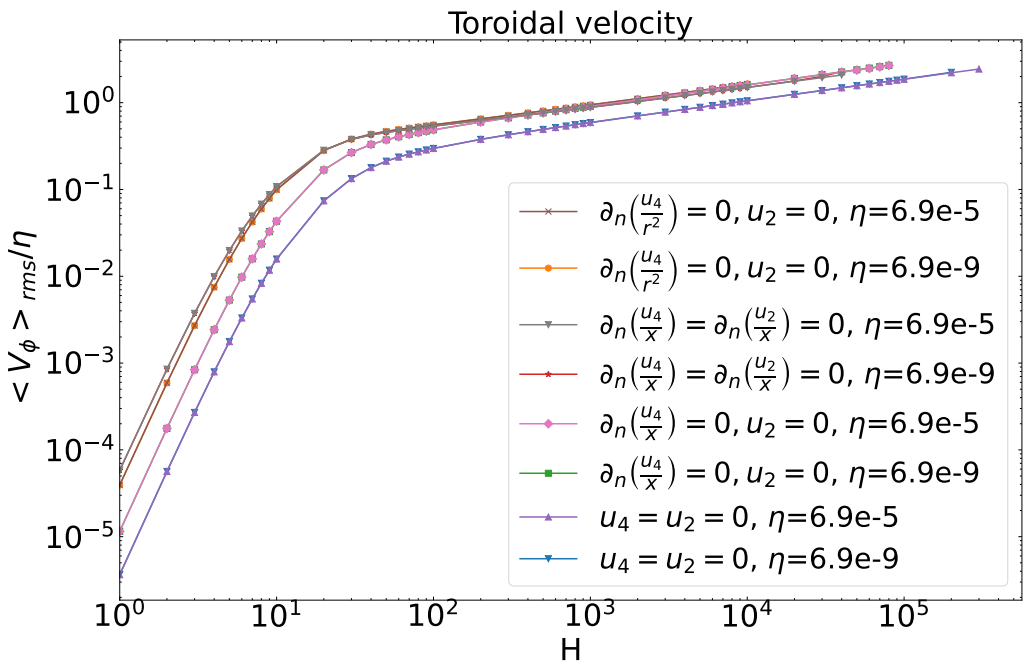

Figure 3.12: Root-mean-square of the toroidal velocity field (in Alfvén velocity units) over η as a function of the Hartmann number in log-log scale for different boundary conditions for the toroidal velocity and vorticity, for different values of the resistivity and a given $E_0/\eta = 0.43$.

3.4.4 Effect of the control parameter

In the present study, we are interested in the behaviour of the system for a given ratio of E_0/η. This quantity may be viewed as the only explicit drive appearing in the dimensionless system of equations (2.44)-(2.49), being the dominant term of $u_6 = xj_\varphi$, that is the toroidal current source term of the Grad-Shafranov equation (2.49). The behaviour $v/\eta \propto H^4$ in the limit of small H was numerically derived in Section 3.4 for E_0/η of order 1. If E_0/η is allowed to vary, then we have a problem with two parameters, H and E_0/η. Let us now consider different values of E_0/η. Figure 3.13 shows the root-mean-square of the toroidal velocity field divided by η, divided by $(E_0/\eta)^3$. This normalization makes all the curves collapse in the $H \to 0$ limit.

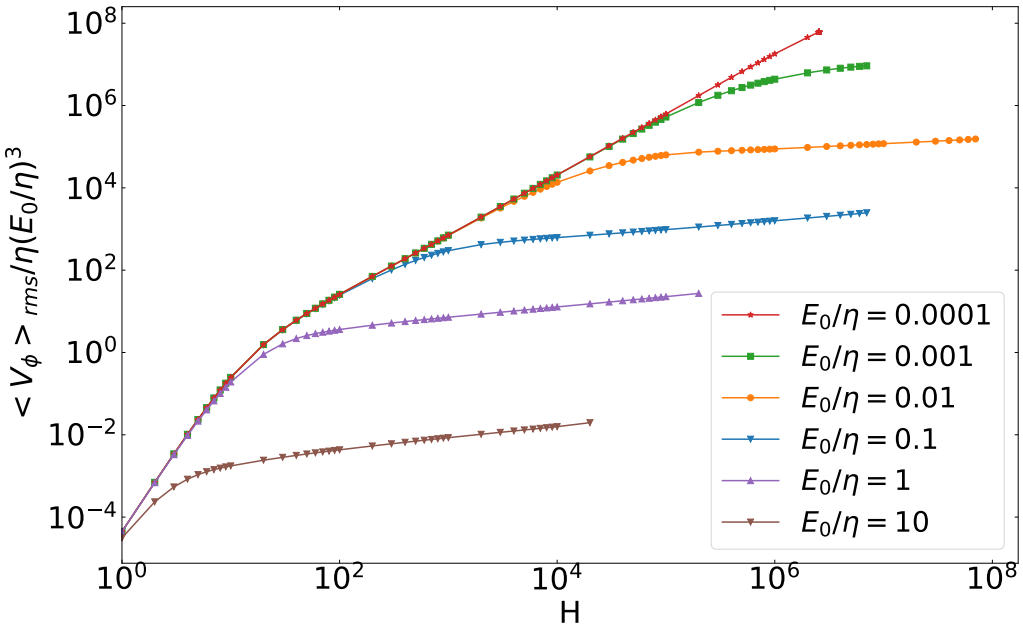

Figure 3.13: Root-mean-square of toroidal velocity field normalized on $\eta(E_0/\eta)^3$ as a function of the Hartmann number in Alfvén velocity v_{A0} units for the different values of the ratio E_0/η.

When E_0/η is small but H is no longer small, we observe the emergence of a new scaling law in H, coming between the previous small H scaling (that we called the first regime) and the large H boundary-layer governed scaling (that we called the second regime). This new intermediary regime is all the more extensive as E_0/η is small and does not involve a boundary layer. These results emphasize the critical role of the E_0/η ratio in influencing the toroidal velocity regimes, scaling and boundary layer formation. That being said, the relevant order of magnitude for E_0/η in tokamaks is about one.

3.5 Conclusions

In the chapter, we investigated the behavior of plasma velocity using a visco-resistive MHD model. Within this framework applied to a tokamak plasma with a prescribed toroidal current drive, we have successfully predicted and numerically validated a scaling law for the velocity. This scaling law is expressed as a function of the resistivity, η, and the Hartmann number, H, where H is defined as $H \equiv (\eta\nu)^{-1/2}$, with ν denoting viscosity. The observed behaviour indicates that the velocity scales as $\eta f(H)$, where f is a specific function. Notably, this scaling law remains valid under the condition that the inertial term $\boldsymbol{\omega} \times \mathbf{v}$ remains negligible, which happens to be the case up to the largest numerically accessible values of the Hartmann number. Within this general scaling law, we have numerically uncovered, for a given, order-one, E_0/η drive, two limiting regimes at low and high H where the function f behaves as a power law.

Various boundary conditions applied to the toroidal velocity and vorticity did not affect the scaling laws. The variation of the drive of the system E_0/η revealed the emergence of a new scaling law in H for small E_0/η values. This new scaling law is an intermediary between the low and high H regimes and does not involve a boundary layer. The critical role of the E_0/η ratio in influencing the toroidal velocity regimes, scaling and boundary layer formation was emphasized.

Overall, the order of magnitude of the plasma velocity remains low compared to experimental measurements and to the expected velocities necessary for taming instabilities. It is possible to attribute this to the absence of turbulence in this axisymmetric and thus 2D model, the lack of symmetry breaking, or the use of a MHD, rather than kinetic modeling. An additional explanation may lie in some insufficiency in the description of the plasma heating drive. This will be the subject of the next chapter. Let us finally emphasize that we are here deliberately exploring scenarios of plasma rotation within the axisymmetric framework since this could 'nip in the bud' 3D instabilities.

Bibliography

Cappello, S. and Escande, D. F. (2000). Bifurcation in Viscoresistive MHD: The Hartmann Number and the Reversed Field Pinch. *Physical Review Letters*, 85(18):3838–3841, DOI: 10.1103/PhysRevLett.85.3838.

Kamp, L. P. and Montgomery, D. C. (2003). Toroidal flows in resistive magnetohydrodynamic steady states. *Physics of Plasmas*, 10:157–167, DOI: 10.1063/1.1524629.

Kamp, L. P. and Montgomery, D. C. (2004). Toroidal steady states in visco-resistive magnetohydrodynamics. *Journal of Plasma Physics*, 70(2):113–142, DOI: 10.1017/S0022377803002629.

Kamp, L. P., Montgomery, D. C., and Bates, J. W. (1998). Toroidal flows in resistive magnetohydrodynamic steady states. *Physics of Fluids*, 10(7):1757–1766, ISSN: 1070-6631, DOI: 10.1063/1.869692.

Chapter 4

Non-inductive current drives

You put this kid behind the wheel,
there's nothing he can't do.

Drive (2011)

Contents

4.1 Introduction

In tokamak plasmas, a critical parameter is the drive that initiates plasma rotation. As demonstrated in the previous chapter, the drive significantly influences toroidal velocity regimes, scaling, and boundary layer formation. Using non-inductive

currents improves the feasibility of the tokamak fusion reactor concept in several ways. They enable steady-state operation and enhance tokamak performance. It has been shown that confinement properties and stability limits can also be improved by controlling the current profile [Ferron et al., 1993; Kessel et al., 1994; Turnbull et al., 1995]. Non-inductive maintenance of the tokamak current is possible by applying unidirectional radio-frequency (RF) waves or Neutral Beam Injection (NBI). [Forest et al., 1994] demonstrated that significant non-inductive currents exist in certain plasma scenarios where neutral beam current drive and pressure-induced bootstrap currents are expected. This study extends the visco-resistive MHD model by incorporating additional non-inductive current drives. By modifying the toroidal current to simulate the effects of NBI and RF heating, we aim to overcome the limitations of traditional models. We employ numerical simulations to analyze the pressure profiles and plasma behaviour.

In Section 4.2, we discuss the limitations of the model proposed by [Kamp and Montgomery, 2003] for describing tokamak plasmas within a MHD visco-resistive framework. It is predicted that this system yields zero pressure in the ideal and motionless limit, which makes us reconsider using $\hat{E}_0/\eta$ as the sole drive in the system. Therefore, we propose the application of an additional drive in Section 4.2.4 to model heating methods applied in real tokamaks, verified through pressure profiles in Section 4.3. Section 4.4 discusses numerical simulations with toroidal current drives. A conclusive Section 4.5 summarizes the study's outcomes.

4.2 The necessity of non-inductive current drive

4.2.1 Self-consistent system of vector equations

The framework employed in this study is MHD. In more precise terms, building on the research initiated by Montgomery and his collaborators, we assume that the axisymmetric steady-states of the plasma are governed by the incompressible visco-resistive MHD. This is consistent with the customary reconstruction of 2D equilibria using the Grad-Shafranov equation, except that we do not assume the velocity field to be zero and reintroduce self-consistency in the model as we do not have free functions. Then, to describe a tokamak plasma, an essential aspect is to model the external drives involved in the system. One inherent drive in this magnetic confinement fusion device is the external magnetic field. Additionally, the need to wind the magnetic field lines and create a macroscopic poloidal component of the magnetic field requires a second forcing mechanism. Following previous references [Kamp and Montgomery, 2003, 2004; Oueslati et al., 2019; Krupka and Firpo, 2024], we assume that this magnetic poloidal component is enabled by a toroidal electric field, which in turn generates a toroidal current density via Ohm's law. The computation of visco-resistive axisymmetric steady states involves then solving the steady-state incompressible Navier–Stokes equation (4.1)-(4.2) along with the solenoidal condition (4.3), Faraday's law (4.4), Ampère law (4.5) and

Ohm's law (4.6) on a tokamak poloidal plasma cross-section Ω. The equations are as follows:

$$(\boldsymbol{v}\cdot\nabla)\boldsymbol{v} = \boldsymbol{J}\times\boldsymbol{B} - \nabla p + \nu\nabla^2\boldsymbol{v}, \tag{4.1}$$
$$\nabla\cdot\boldsymbol{v} = 0, \tag{4.2}$$
$$\nabla\cdot\boldsymbol{B} = 0 \tag{4.3}$$
$$\nabla\times\boldsymbol{E} = 0 \tag{4.4}$$
$$\nabla\times\boldsymbol{B} = \boldsymbol{J} \tag{4.5}$$
$$\boldsymbol{E} + \boldsymbol{v}\times\boldsymbol{B} = \eta\boldsymbol{J}. \tag{4.6}$$

With respect to the drives, both the externally applied (vacuum) toroidal magnetic field and the steady-state toroidal electric field required to drive the toroidal current are curl-free. We have

$$\boldsymbol{B}_{\text{ext}} = \frac{1}{x}\boldsymbol{i}_\varphi, \tag{4.7}$$
$$\boldsymbol{E}_{\text{ext}} = \frac{\hat{E}_0}{x}\boldsymbol{i}_\varphi, \tag{4.8}$$

with $\boldsymbol{i}_\varphi$ a unit vector in the toroidal (azimuthal) direction. The magnetic and electric fields in Equations (4.1)-(4.6) are the sum of these external contributions and of the self-consistent plasma fields. This system of equations needs to be solved on the plasma cross-section Ω with suitable boundary conditions. From a computational perspective, we solve the system of PDE we are now presenting.

4.2.2 Scalar PDE formulation

One can eliminate the unknown pressure term by taking the curl of Equation (4.1). This signifies that the pressure is a passive variable and not an actuator. Moreover, the velocity $\boldsymbol{v}$, vorticity $\boldsymbol{\omega} \equiv \nabla\times\boldsymbol{v}$, magnetic $\boldsymbol{B}$ and current density $\boldsymbol{J}$ vector fields are divergence-free. They admit then the following representations defining the scalar functions u_1, ..., u_6 of $(x, y) \in \Omega$ through the relationships

$$\boldsymbol{v} = \frac{1}{x}\nabla u_1\times\boldsymbol{i}_\varphi + \frac{u_4}{x}\boldsymbol{i}_\varphi, \tag{4.9}$$
$$\boldsymbol{\omega} = \frac{1}{x}\nabla u_4\times\boldsymbol{i}_\varphi + \frac{u_2}{x}\boldsymbol{i}_\varphi, \tag{4.10}$$
$$\boldsymbol{B} = \frac{1}{x}\nabla u_5\times\boldsymbol{i}_\varphi + \frac{u_3}{x}\boldsymbol{i}_\varphi, \tag{4.11}$$
$$\boldsymbol{J} = \frac{1}{x}\nabla u_3\times\boldsymbol{i}_\varphi + \frac{u_6}{x}\boldsymbol{i}_\varphi. \tag{4.12}$$

The above system of equations (4.1)-(4.6) with the external drives (4.7)-(4.8) is amenable [Kamp and Montgomery, 2003; Kamp et al., 1998; Kamp and Montgomery, 2004; Krupka and Firpo, 2024; Roverc'h et al., 2021] to the following set of five scalar elliptic PDE

$$\triangle^* u_1 = -u_2, \tag{4.13}$$

$$\nu\triangle^* u_2 = \frac{1}{x^2}\frac{\partial}{\partial y}(u_3^2 - u_4^2) + \frac{1}{x}\{u_6, u_5\} + \frac{1}{x}\{u_1, u_2\} + \tag{4.14}$$

$$+ \frac{2u_2}{x^2}\frac{\partial u_1}{\partial y} - \frac{2u_6}{x^2}\frac{\partial u_5}{\partial y}, \tag{4.15}$$

$$\eta\triangle^* u_3 = \frac{1}{x}\{u_1, u_3\} + \frac{1}{x}\{u_4, u_5\} + \frac{2u_3}{x^2}\frac{\partial u_1}{\partial y} - \frac{2u_4}{x^2}\frac{\partial u_5}{\partial y}, \tag{4.16}$$

$$\nu\triangle^* u_4 = \frac{1}{x}\{u_1, u_4\} + \frac{1}{x}\{u_3, u_5\}, \tag{4.17}$$

$$\triangle^* u_5 = -u_6 \tag{4.18}$$

with the toroidal projection of Ohm's law giving the constraint

$$\eta u_6 = \hat{E}_0 + \frac{1}{x}\{u_5, u_1\}. \tag{4.19}$$

A relevant dimensionless control parameter has been shown [Montgomery, 1993; Cappello and Escande, 2000; Krupka and Firpo, 2024] to be the Hartmann number, $H = (\eta\nu)^{-1/2}$. This is expected to be a large parameter in the range 10^6 to 10^8 in fusion-relevant conditions. Available numerical results [Kamp and Montgomery, 2003; Kamp et al., 1998; Kamp and Montgomery, 2004] for realistic inputs in the external drives (4.7) and (4.8) with constant $\hat{E}_0$ and up-down symmetric boundary conditions have produced very low values of the typical, root-mean-square, steady-state velocity components. Our next step is to investigate the cause of this outcome.

4.2.3 Examination of the pressure field

Let us now examine the pressure profile in the visco-resistive model (4.1)-(4.6) with the external drives (4.7)-(4.8). Let us assume for now that the steady-state plasma speed is negligible. Then, in the ideal limit, $\eta \to 0$ and $\nu \to 0$, the steady-state Navier-Stokes equation (4.1) takes the form of the usual Grad-Shafranov equation

$$\nabla p = \boldsymbol{J} \times \boldsymbol{B}. \tag{4.20}$$

Restricting to axisymmetric solutions, the projection of this equation on x and y gives, respectively,

$$\frac{\partial p}{\partial x} = x^{-2}\left(-u_3\frac{\partial u_3}{\partial x} + u_6\frac{\partial u_5}{\partial x}\right), \tag{4.21}$$

$$\frac{\partial p}{\partial y} = x^{-2}\left(-u_3\frac{\partial u_3}{\partial y} + u_6\frac{\partial u_5}{\partial y}\right). \tag{4.22}$$

In the toroidal direction, we get

$$0 = x^{-2}\{u_5, u_3\} \tag{4.23}$$

This amounts to the well-known property of Grad-Shafranov's theory that the diamagnetic function u_3 is a function of only the magnetic flux u_5. Moreover, writing that $\boldsymbol{J} \times \boldsymbol{B}$ is curl-free, which follows from the Grad-Shafranov equation (4.20) and projecting this on the toroidal direction yields

$$-2u_3\frac{\partial u_3}{\partial y} + x\{u_5, u_6\} + 2u_6\frac{\partial u_5}{\partial y} = 0. \tag{4.24}$$

Then, combining Equations (4.22) and (4.24), the pressure gradient along the y-axis with a zero-flow hypothesis is given by

$$\frac{\partial p}{\partial y} = \frac{1}{2x}\{u_6, u_5\}. \tag{4.25}$$

Assuming no plasma flow, the toroidal projection of Ohm's law in Equation (4.19) states simply that u_6 is a constant with $u_6 = \hat{E}_0/\eta$. Equation (4.25) indicates that the pressure field does not depend on y. Yet, from the set of equations (4.21)-(4.22)-(4.23), one can simply obtain that the pressure is a function of the magnetic flux u_5 as $\{p, u_5\} = 0$. Thus, we are left with $\partial_y p = p'(u_5)\partial_y u_5 = 0$. This means that the pressure profile is constant. As it must be equal to its value on the border of Ω, this means that the pressure, and thus the temperature of the system, is zero.

4.2.4 Implementation of non-inductive current drives

Section 4.2.3 shows that the simplifying assumption of a toroidal current density component arising solely from Ohm's law in response to a time-independent, curl-free toroidal electric field given by Equation (4.8) puts serious limitations to the model. Indeed, the effective pressure in the model is solely due to the fact that toroidal geometry and viscous dissipation force the steady-state velocity field to be not identically zero. This allows the pressure profile to be not vanishingly small as u_6 is then not exactly constant. But, we are missing in the modeling a robust way to ensure adequate heating for achieving fusion conditions. Therefore, modifications incorporating alternative heating methods are essential to achieve higher pressure. We shall see that this also tends to induce higher rotation velocities of the plasma.

In our previous analysis, we focused on the behaviour of the system for a specific ratio of $\hat{E}_0/\eta$, which was considered the only explicit drive in the dimensionless system of equations in Chapter 3. We aim to introduce an additional driving force in the current field. This will appear as an extra term in the toroidal component of Ohm's law in Equation (4.6):

$$\frac{\hat{E}_0}{x} + (\boldsymbol{v} \times \boldsymbol{B}) \cdot \mathbf{i}_\varphi + j_d = \eta \boldsymbol{J} \cdot \mathbf{i}_\varphi, \tag{4.26}$$

where j_d represents a current drive. Since $u_6 = x j_\varphi$, Equation (2.49) now becomes

$$\eta u_6 = \hat{E}_0 + \frac{1}{x} \{u_5, u_1\} + j_d x. \tag{4.27}$$

In order to investigate the impact of such a non-inductive current drive, we chose two families of functions for the current drive. This is meant as a first approach to modeling current distribution similar to that created by heating methods in tokamaks, which can be seen as "adding a bump" to the current distribution. Functions on the x-axis give the first family model as

$$j_d(x, y) = -\frac{r_0^2}{r_1^2} A (x-1)^2 + B, \tag{4.28}$$

where r_0 is the major radius, r_1 is the semi-minor axis of the cross-section, A is a magnitude of the bump and B is an offset in the current distribution. Considering the case of Equation (4.28) with $A = B = 1$, Figure 4.1 compares at $H = 10$ the toroidal current density fields computed using Equations (2.44)-(2.48) with the toroidal projection of Ohm's law (4.27) for $j_d = 0$ (original reference case) and $j_d = -\frac{r_0^2}{r_1^2}(x-1)^2 + 1$. The original system of equations with only the $\hat{E}_0/\eta$ drive ($j_d = 0$) does not produce realistic toroidal current density profiles, despite giving a realistic total current, since the $\hat{E}_0/\eta$ ratio of about 1 corresponds to the realistic total current.

To investigate this further, we considered a second family of current drive, j_D, defined as the solution to the Poisson's equation $\nabla^2 j_D = -A$ with the boundary

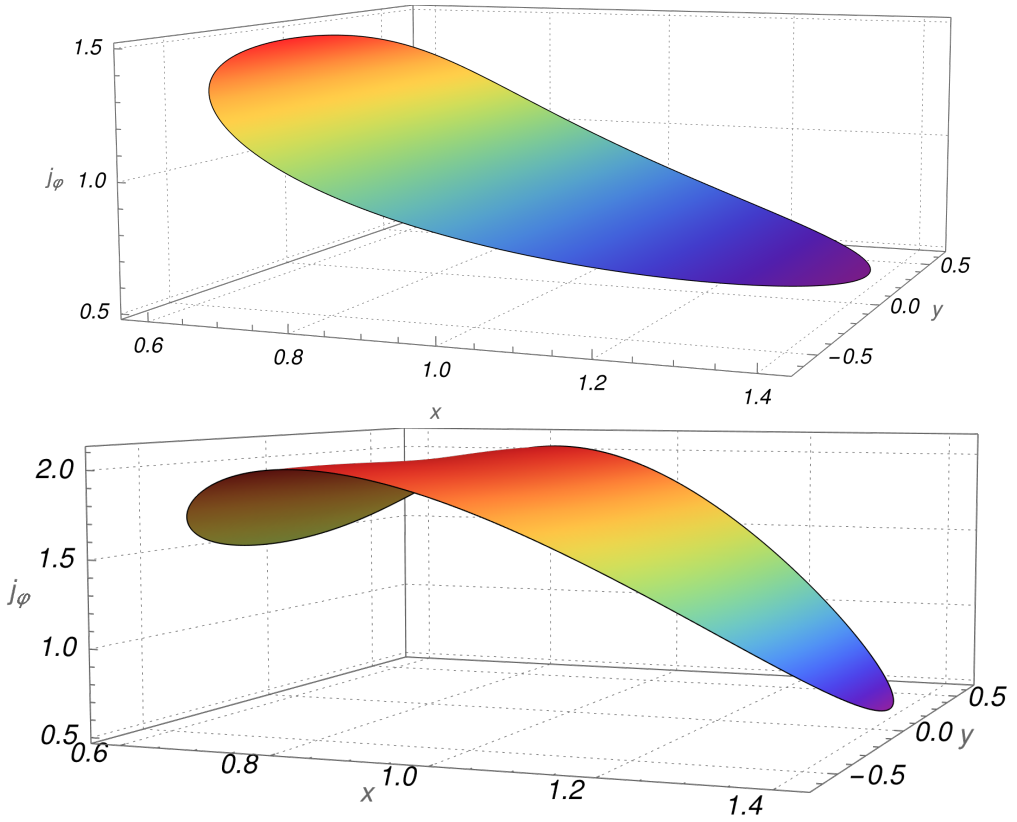

Figure 4.1: Toroidal current field without the application of the drive $j_d = 0$ (on the top) and with the application of the drive $j_d = -r_0^2/r_1^2(x-1)^2 + 1$ for $H = 10$ in dimensionless units (on the bottom).

condition $j_D = B$ on $\partial\Omega$. As before, A represents the magnitude and B the offset of the drive. Figure 4.2 shows the drive j_D with magnitude $A = 100$ and offset $B = 0$, along with the resulting toroidal current distribution when this drive is applied. We intend to test two impacts of these drives, j_d and j_D, within our

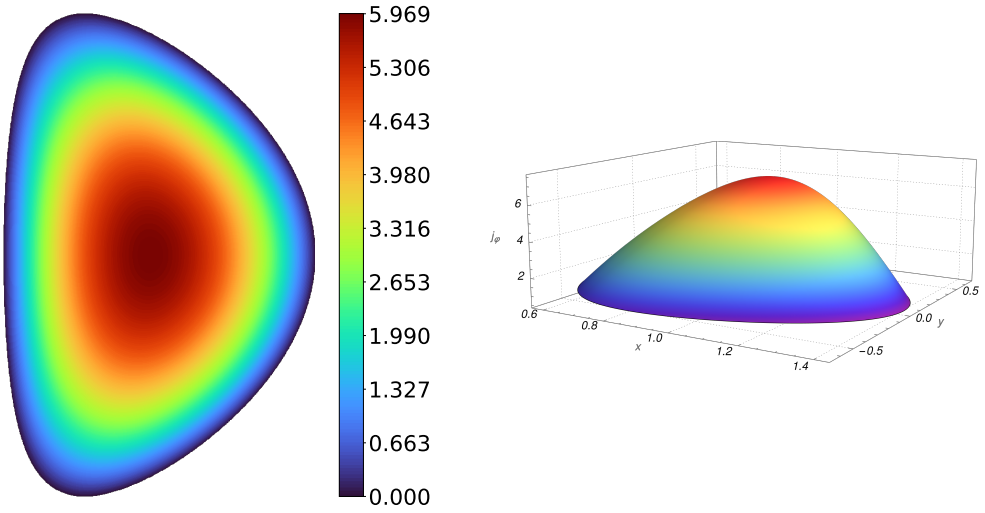

Figure 4.2: Drive on the toroidal current j_D with $A = 100, B = 0$ (on the left) and resulting toroidal current distribution j_φ at $H = 10$ (on the right).

system. We shall first assess their impact on the pressure profile. To that end, we must be able to evaluate the pressure field. The following section will be dedicated to this establishment of the pressure field.

4.3 Pressure determination

4.3.1 Establishing Poisson's equation for the pressure field

Let us go back to the steady-state Navier-Stokes equation (4.1) and rewrite it as

$$\boldsymbol{\omega} \times \boldsymbol{v} = \boldsymbol{J} \times \boldsymbol{B} - \nabla p^* + \nu \nabla^2 \boldsymbol{v} \tag{4.29}$$

with

$$p^* = p + \frac{v^2}{2}. \tag{4.30}$$

Previously, we eliminated the pressure term by taking the curl and considering the toroidal part of the force balance equation. Now, to obtain the pressure of the system, we take the divergence of Equation (4.29)

$$\nabla \cdot \nabla p^* = \nabla \cdot \left[-\boldsymbol{\omega} \times \boldsymbol{v} + \boldsymbol{J} \times \boldsymbol{B} + \nu \nabla^2 \boldsymbol{v} \right]. \tag{4.31}$$

This takes the form of Poisson's equation for the pressure p^* as the left-hand side yields the Laplacian of the pressure, $\triangle p^*$. Taking the divergence of the first term on the right-hand side gives

$$-\nabla \cdot (\boldsymbol{\omega} \times \boldsymbol{v}) = \boldsymbol{v} \cdot \nabla^2 \boldsymbol{v} + \boldsymbol{\omega}^2. \tag{4.32}$$

We can treat the $\boldsymbol{J} \times \boldsymbol{B}$ term similarly

$$\nabla \cdot (\boldsymbol{J} \times \boldsymbol{B}) = -\boldsymbol{B} \cdot \nabla^2 \boldsymbol{B} - \boldsymbol{J}^2. \tag{4.33}$$

Finally, the term $\nabla \cdot (\nu \nabla^2 \boldsymbol{v})$ equals zero due to the incompressibility condition $\nabla \cdot \boldsymbol{v} = 0$. Therefore, the complete Poisson's equation for the pressure is

$$\triangle p^* = \boldsymbol{v} \cdot \nabla^2 \boldsymbol{v} + \boldsymbol{\omega}^2 - \boldsymbol{B} \cdot \nabla^2 \boldsymbol{B} - \boldsymbol{J}^2 \tag{4.34}$$

where $\triangle$ is defined as

$$\triangle A \equiv \frac{\partial^2 A}{\partial x^2} + \frac{1}{x}\frac{\partial A}{\partial x} + \frac{\partial^2 A}{\partial y^2}. \tag{4.35}$$

Now, let us write this Poisson's equation (4.34) in terms of the functions u_1, ..., u_6 of $(x, y) \in \Omega$. To achieve this, we examine each term individually. Using the expression for the vorticity (4.10), the second term becomes

$$\boldsymbol{\omega}^2 = -\frac{u_2}{x^2}\triangle^* u_1 + \frac{1}{x^2}\frac{\partial u_4}{\partial x}\frac{\partial u_4}{\partial x} + \frac{1}{x^2}\frac{\partial u_4}{\partial y}\frac{\partial u_4}{\partial y}. \tag{4.36}$$

Similarly, for the square of the current density vector (4.12), we get

$$\boldsymbol{J}^2 = -\frac{u_6}{x^2}\triangle^* u_5 + \frac{1}{x^2}\frac{\partial u_3}{\partial x}\frac{\partial u_3}{\partial x} + \frac{1}{x^2}\frac{\partial u_3}{\partial y}\frac{\partial u_3}{\partial y}. \tag{4.37}$$

Finally, let us examine the term $\boldsymbol{B} \cdot \nabla^2 \boldsymbol{B}$. We can use the identity $\boldsymbol{B} \cdot \nabla^2 \boldsymbol{B} = -\boldsymbol{B} \cdot (\nabla \times \boldsymbol{J})$ with

$$\boldsymbol{B} \cdot (\nabla \times \boldsymbol{J}) = -\frac{u_3}{x^2}\triangle^* u_3 + \frac{1}{x^2}\frac{\partial u_5}{\partial x}\frac{\partial u_6}{\partial x} + \frac{1}{x^2}\frac{\partial u_5}{\partial y}\frac{\partial u_6}{\partial y}. \tag{4.38}$$

Similarly, we have

$$\boldsymbol{v} \cdot (\nabla \times \boldsymbol{\omega}) = -\frac{u_4}{x^2}\triangle^* u_4 + \frac{1}{x^2}\frac{\partial u_2}{\partial x}\frac{\partial u_1}{\partial x} + \frac{1}{x^2}\frac{\partial u_2}{\partial y}\frac{\partial u_1}{\partial y}. \tag{4.39}$$

Incorporating all of these contributions into the right-hand side of Poisson's equation yields

$$\begin{aligned}
\triangle p^* = {} & \frac{u_4}{x^2}\triangle^* u_4 - \frac{1}{x^2}\frac{\partial u_2}{\partial x}\frac{\partial u_1}{\partial x} - \frac{1}{x^2}\frac{\partial u_2}{\partial y}\frac{\partial u_1}{\partial y} \\
& - \frac{u_2}{x^2}\triangle^* u_1 + \frac{1}{x^2}\frac{\partial u_4}{\partial x}\frac{\partial u_4}{\partial x} + \frac{1}{x^2}\frac{\partial u_4}{\partial y}\frac{\partial u_4}{\partial y} \\
& - \frac{u_3}{x^2}\triangle^* u_3 + \frac{1}{x^2}\frac{\partial u_5}{\partial x}\frac{\partial u_6}{\partial x} + \frac{1}{x^2}\frac{\partial u_5}{\partial y}\frac{\partial u_6}{\partial y} \\
& + \frac{u_6}{x^2}\triangle^* u_5 - \frac{1}{x^2}\frac{\partial u_3}{\partial x}\frac{\partial u_3}{\partial x} - \frac{1}{x^2}\frac{\partial u_3}{\partial y}\frac{\partial u_3}{\partial y}.
\end{aligned} \tag{4.40}$$

This elliptic differential equation needs to be solved with a boundary condition and allow the pressure profiles for the different drives to be computed. In this work, we calculate pressure profiles with the assumption that the pressure on the border equals zero. Of course, it is necessary to enforce the Neumann boundary condition in the pressure calculation. According to [Kress and Montgomery, 2000], the normal component of ∇p is enough to determine p through the Neumann boundary condition. Appendix B is dedicated to the detailed derivation of the pressure together with boundary conditions. To the best of our knowledge, the derivation of Equation (4.40) within the visco-resistive system is novel.

4.3.2 Numerical solutions to Poisson's equation for the pressure

Let us now solve the above Poisson's equation for the pressure assuming a zero pressure condition at the boundary $\partial\Omega$. It is important to note that, in the absence of an additional toroidal current drive and assuming no plasma flow, we inferred a zero pressure in the limits $\eta \to 0$ and $\nu \to 0$, in Section 4.2.3. To verify the pressure distribution in the absence of the drive with plasma flow, let us examine Figure 4.3. This figure shows the pressure $p = p^* - v^2/2$ computed without the application of the drive, that is, in the original system of equations, for $H = 10$ and $H = 10^5$. The pressure profiles are presented in Pascal units (Pa). Let us remind you that the realistic pressure value is in the order of $10^5 \sim 10^6$ Pa in the JET tokamak [JET Team, 1992].

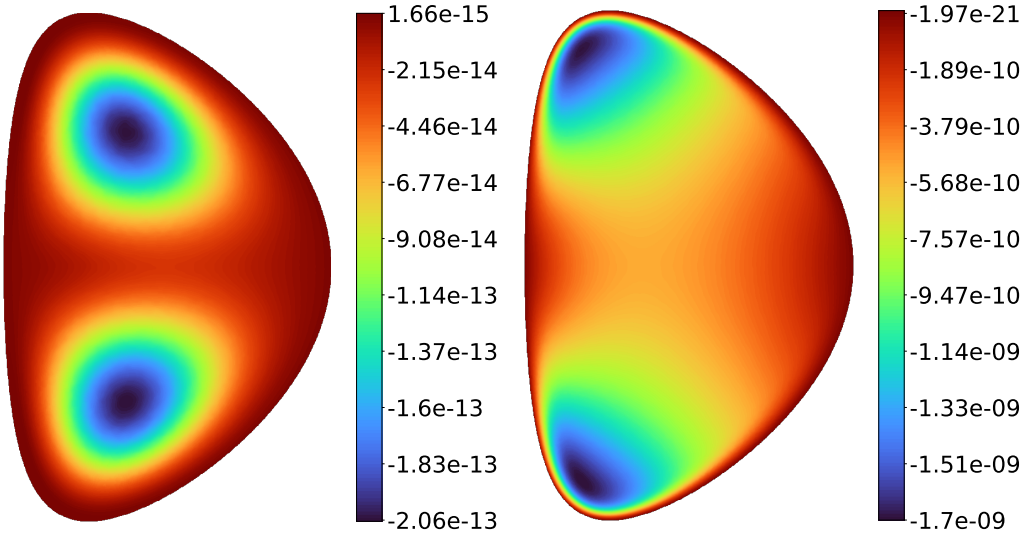

Figure 4.3: Pressure profiles computed without the application of the drive ($j_d = 0$) on the toroidal current field for $H = 10$ (on the left) and for $H = 10^5$ (on the right).

The order of magnitude of the pressure field in the absence of the current drive turns out to be unrealistically small, as predicted in Section 4.2.3. Additionally, the pressure distribution does not follow the magnetic flux profile, indicating that the pressure is solely driven by the velocity terms. Now, let us examine the pressure distributions shown in Figure 4.4 for two drives: j_d with $A = 1$ and $B = 1$, and j_D with $A = 100$ and $B = 0$. The application of these additional drives not only avoids unrealistically low-pressure levels but also achieves pressure levels comparable to those observed in the JET tokamak.

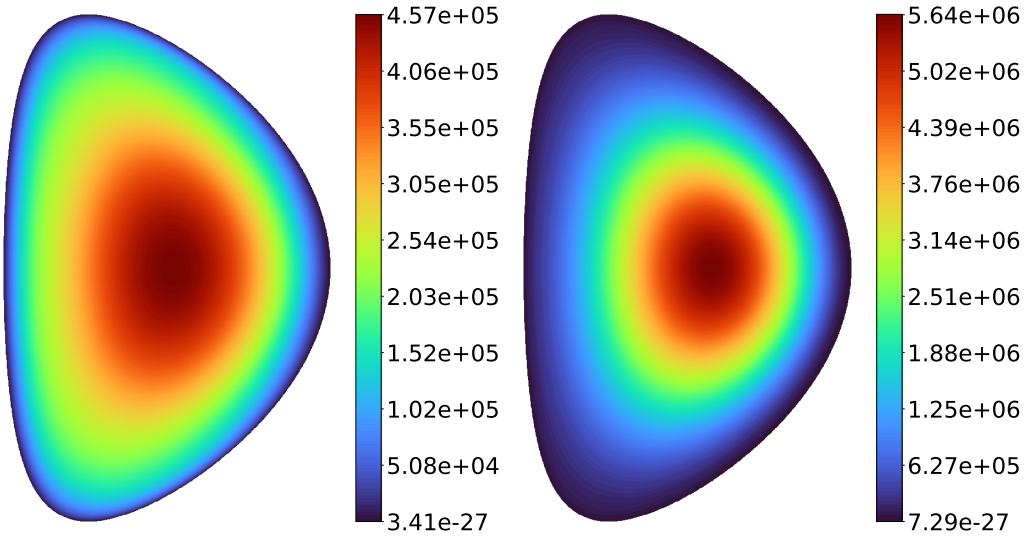

Figure 4.4: Pressure profiles computed with the application of the drive j_d with $A = 1$ and $B = 1$ (on the left) and j_D with $A = 100$ and $B = 0$ (on the right) on the toroidal current field for $H = 10^5$.

With the application of the drives, achieving a different configuration of magnetic flux surfaces is possible, including non-nested magnetic field lines with several $n = 0$ islands present. An example is given in Figure 4.5 that shows the magnetic flux surfaces and the pressure profile when the drive j_D with $A = 100$ and $B = -5$ is applied. Although the results from this drive will be discussed in more detail later, it is worth noting that the magnetic field lines generated by this drive represent an extreme case. Most drives, which will be discussed in Section 4.4, typically produce nested magnetic field lines.

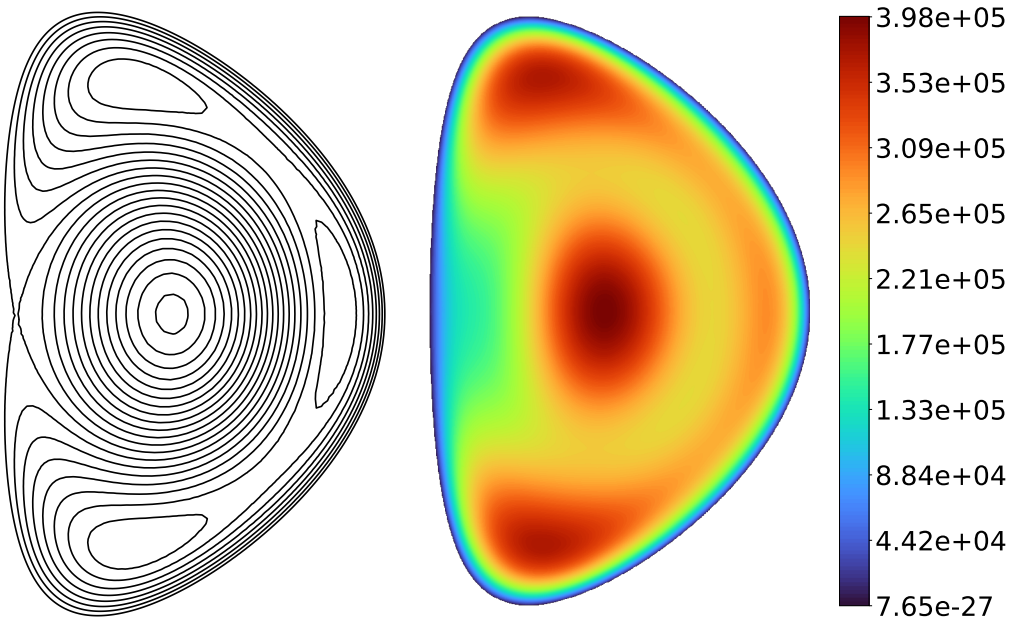

Figure 4.5: Magnetic flux surfaces with internal separatrices (on the left) and pressure profiles (on the right) computed with the application of the drive j_D with $A = 100$ and $B = -5$ on the toroidal current field for $H = 10^5$.

4.4 Numerical outcomes with toroidal current drives

4.4.1 A first test case

Let us consider the toroidal current drive j_d here with $A = 5$ and $B = 1$. Figure 4.6 shows the toroidal current distribution with this drive at two different Hartmann numbers $H = 10$ and $H = 10^5$. The total current generated by this drive is approximately 0.37 MA for $H = 10$ and 0.35 MA for $H = 10^5$, which is lower than the typical total current of 0.6 MA generated by the ratio $\hat{E}_0/\eta$.

Figure 4.7 shows the computed steady-state axisymmetric toroidal velocity fields for the same two Hartmann numbers, $H = 10$ and $H = 10^5$. Significant changes in the velocity distribution are observed compared to the case without the drive in Chapter 3. The velocity profiles exhibit an irregular shape at low Hartmann numbers. However, the up-down symmetry is preserved at both low and high Hartmann numbers, as theoretically predicted [Oueslati and Firpo, 2020], which indicates good numerical robustness.

Now, let us analyze the root-mean-square of the toroidal and poloidal velocities, as shown in Figure 4.8, while considering different numbers of triangles in the mesh N, with the application of the drive j_d with $A = 5$ and $B = 1$. The figure demonstrates that applying the drive j_d results in a significant increase in the

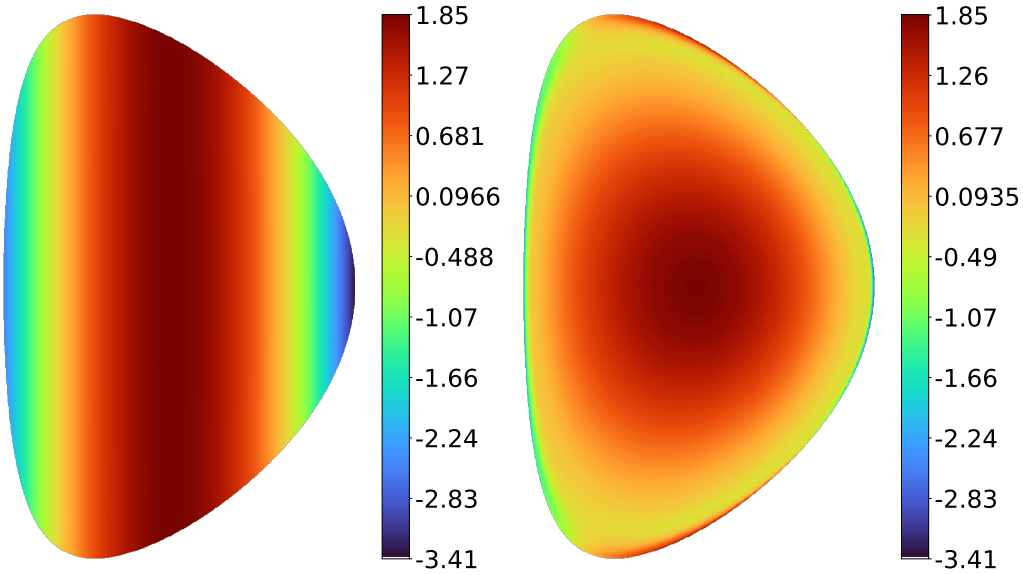

Figure 4.6: Toroidal current field with the application of the drive j_d with $A = 5$, $B = 1$ for $H = 10$ (on the left) and $H = 10^5$ (on the right).

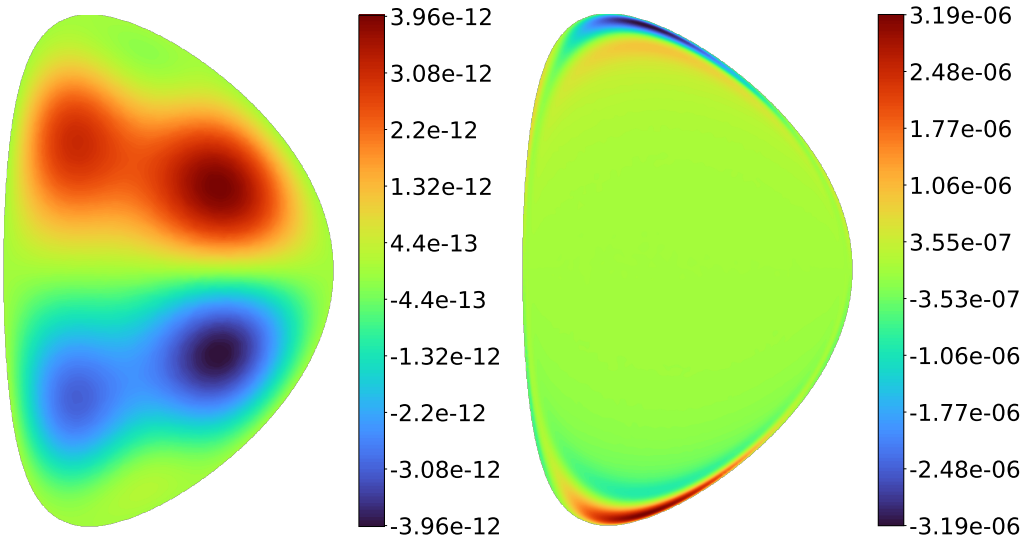

Figure 4.7: Toroidal velocity field for $H = 10$ (on the left) and $H = 10^5$ (on the right) computed with the application of the drive j_d with $A = 5$ and $B = 1$ on the toroidal current field.

toroidal velocity. Furthermore, we observe much more stable results when varying the number of triangles compared to those reported in the previous chapter.

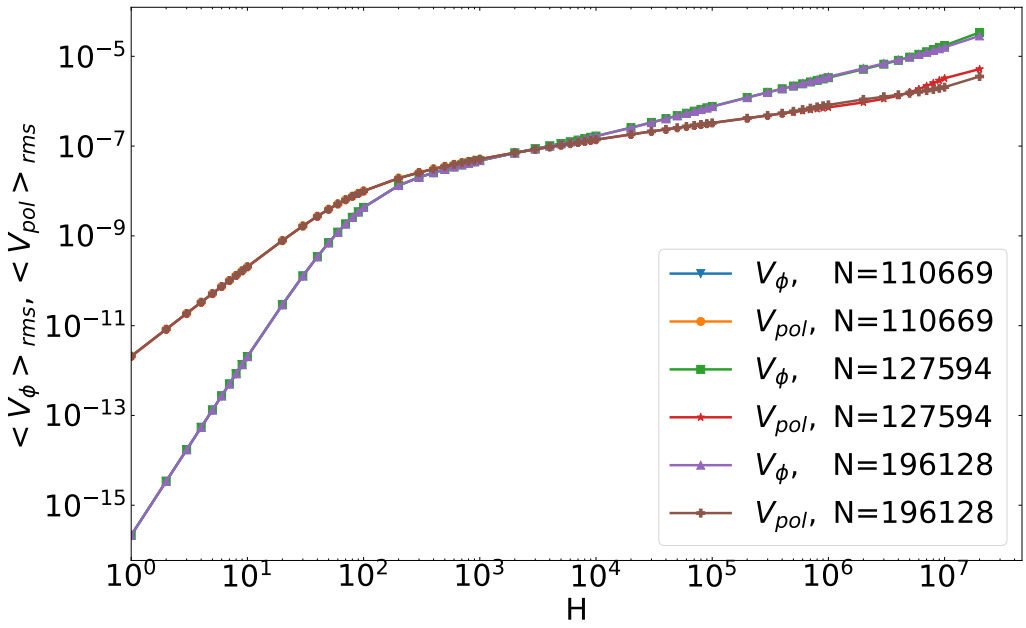

Figure 4.8: Root-mean-square of toroidal and poloidal velocities as a function of the Hartmann number in Alfvén velocity units with the application of the drive j_d with $A = 5$ and $B = 1$ on the toroidal current field for different numbers of triangles.

4.4.2 Parametric study of two current drive families

Now, let us consider different parameters of the drives, such as magnitude A and offset B, to understand the behaviour of plasma velocity under the assumption of the applied toroidal current drives. Figure 4.9 illustrates the root-mean-square of the toroidal velocity while applying the drive j_d with $B = 1$ to the toroidal current field across various values of A. Here, we aim to explore the impact of varying the magnitude of the bump. As depicted, the toroidal velocity gradually increases with the augmentation of the magnitude. Additionally, we include the reference case of the drive $j_d = 0$, which represents the main result obtained in the chapter 3 to compare the results.

Figure 4.10 also presents the root-mean-square of the toroidal velocity as in Figure 4.9, but with a fixed value of $A = 5$, while exploring different values of B. In this scenario, the situation is reversed: as the offset of the drive increases, the velocities diminish. Although all the curves appear to develop linear behaviour in the $H \to \infty$ limit, this is not actually the case. The curves for $B = 1, 2, 3$ begin

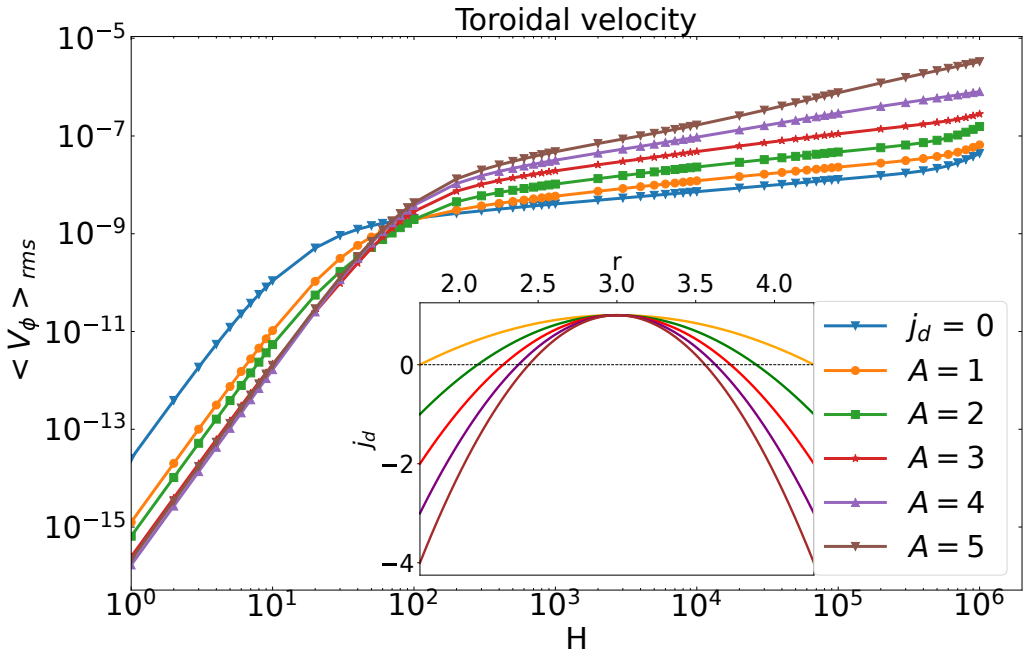

Figure 4.9: Root-mean square of toroidal velocity in Alfvèn velocity units as a function of the Hartmann number, with the application of the drive j_d with $B = 1$ on the toroidal current field, for the different values of A.

to bend in this limit, making it impossible to scale velocities with the Hartmann number. We must investigate another drive family j_D to verify this behaviour.

Let us examine the velocity distribution by applying the drive j_D. Figure 4.11 presents the toroidal velocity field computed with Hartmann numbers $H = 10$ and $H = 10^5$ with the application of the drive j_D with magnitude $A = 100$ and an offset $B = 0$ on the toroidal current field. The results show that the drive does not significantly impact the velocity distribution, as the behaviour remains nearly identical to the no-drive case, with no noticeable increase in velocity.

To verify this, we vary now the magnitude of the drive. Figure 4.12 presents the same as Figure 4.9 but for a different drive j_D applied. It can be observed that while varying the magnitude of the drive causes an increase in velocities in the first regime, the second regime (the boundary layer regime) remains almost unchanged despite the application of drives with different magnitudes. Increasing the magnitude of the drive raises the total current, but the velocities seem unaffected by the variation of the total current of the system.

Next, let us examine how the velocities change with the variation of the parameter B, which represents the offset of the drive j_D. Figure 4.13 presents the same as Figure 4.12, but with a fixed value of $A = 100$ while exploring different values of B. Shifting the drive results in the highest velocities at $B = -5$. It is

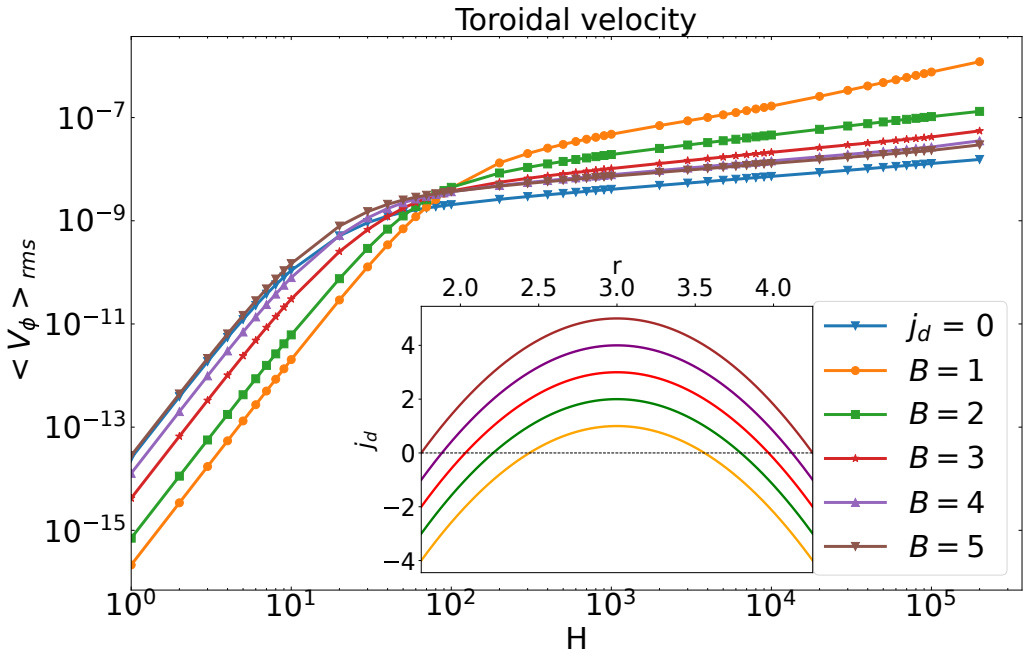

Figure 4.10: Root-mean-square of toroidal velocity in Alfvèn velocity units as a function of the Hartmann number, with the application of the drive j_d with $A = 5$ on the toroidal current field, for the different values of B .

evident that the "normal" velocity behaviour changes at certain parameters of the drive.

As described in Chapter 3, in the original visco-resistive MHD system with $j_d = 0$, two distinct regimes of scaling laws were observed. The velocities scaled with the Hartmann number, as H^4 for the toroidal velocity and H^2 for the poloidal velocity in the first regime corresponding to the $H \to 0$ limit, and as $H^{1/4}$ for both velocity components in the second regime associated with the $H \to \infty$ limit, in which a boundary layer exists. Additionally, we previously identified an "inter-regime" responsible for the boundary layer formation process. We noted that applying different $\hat{E}_0/\eta$ ratios affected the inter-regime and delayed the onset of the boundary layer formation in terms of the Hartmann number. With the application of the drives in the first regime, the velocities have the same scaling: H^4 for the toroidal velocity and H^2 for the poloidal velocity. However, in the second regime, there are two scenarios: either the boundary layer forms, as shown in Figure 4.11, maintaining the scaling law $< v_{\varphi,pol} >_{rms} \sim \eta H^{1/4}$ for j_D with $B = 0, 3$, or the velocities do not develop a linear behaviour in log-log scale for $B = -3, -5, -7$. The curves are bent, making it impossible to scale velocities with the Hartmann number. We can conclude that with the application of the drives when the expected velocity behaviour is disrupted (or the boundary layer is not

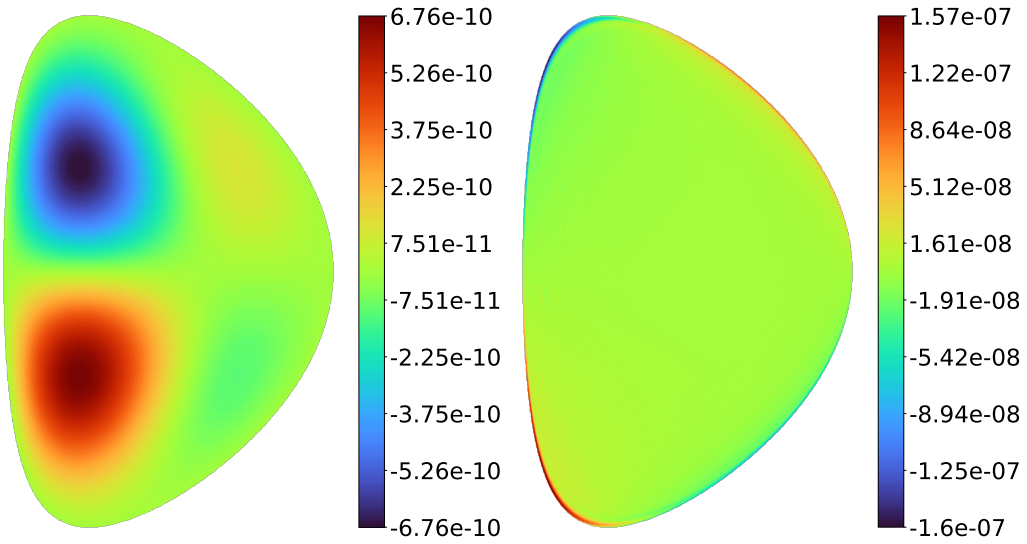

Figure 4.11: Toroidal velocity field for $H = 10$ (on the left) and $H = 10^5$ (on the right) computed with the application of the drive j_D with $A = 100$ and $B = 0$ on the toroidal current field.

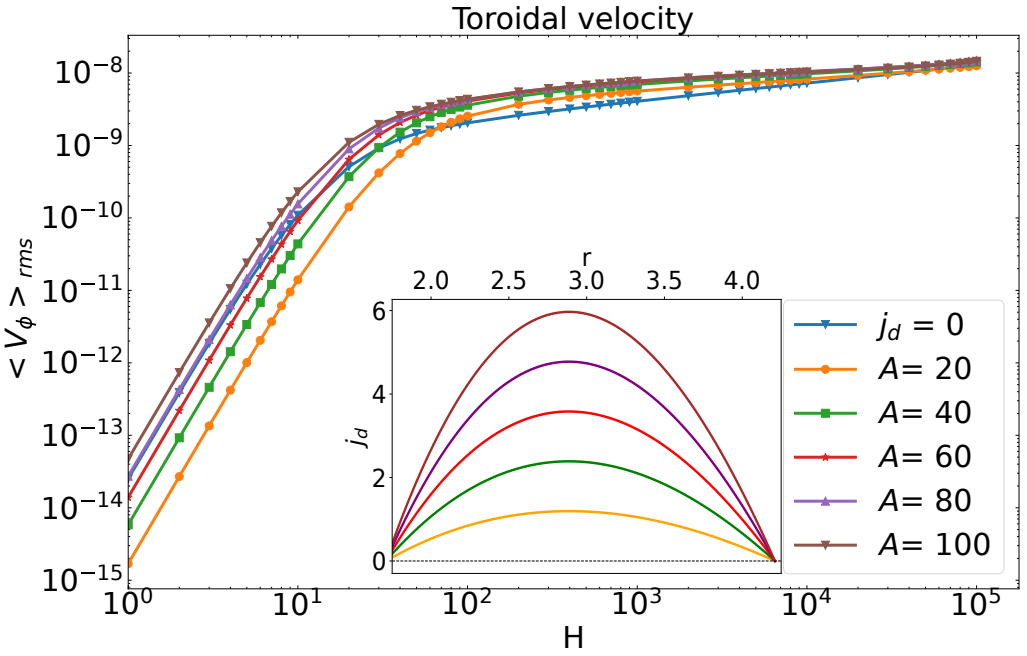

Figure 4.12: Root-mean-square of toroidal velocity in Alfvèn velocity units as a function of the Hartmann number, with the application of the drive j_D with $B = 0$ on the toroidal current field, for the different values of A.

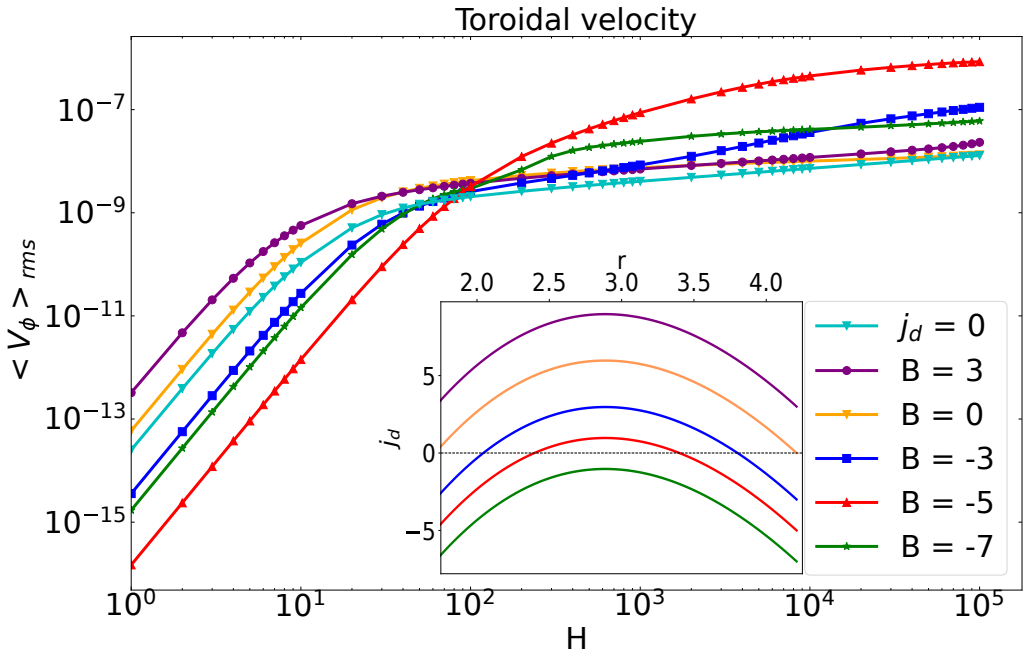

Figure 4.13: Root-mean-square of toroidal velocity in Alfvèn velocity units as a function of the Hartmann number, with the application of the drive j_D with $A = 100$ on the toroidal current field, for the different values of B .

formed), velocities can no longer be scaled with the Hartmann number.

4.4.3 Non-nested magnetic flux surfaces

Let us examine the toroidal current with the drive applied in the positive region and between the positive and negative regions. Figure 4.14 shows the toroidal current field influenced by drives j_D with $A = 100$ and $B = 0$ on the left and $B = -5$ on the right for $H = 10^5$. The second drive applied here results in non-nested magnetic flux surfaces.

Next, we examine the velocity distribution. Figure 4.15 shows the toroidal velocity field for $H = 10$ on the left and $H = 10^5$ on the right with $B = -5$, with the drive applied between the positive and negative regions. The velocity distribution for a Hartmann number $H = 10^5$ mirrors the toroidal current distribution, with the highest velocities occurring at the transition point between the positive and negative regions. When the drive is entirely in the positive or negative region, the boundary layer formation seems to be preserved, and the application of the drive does not significantly affect the velocity magnitude, but when the drive is in between positive and negative regions, we observe a completely different behaviour. Here, the positive and negative regions refer to the direction of the current inside

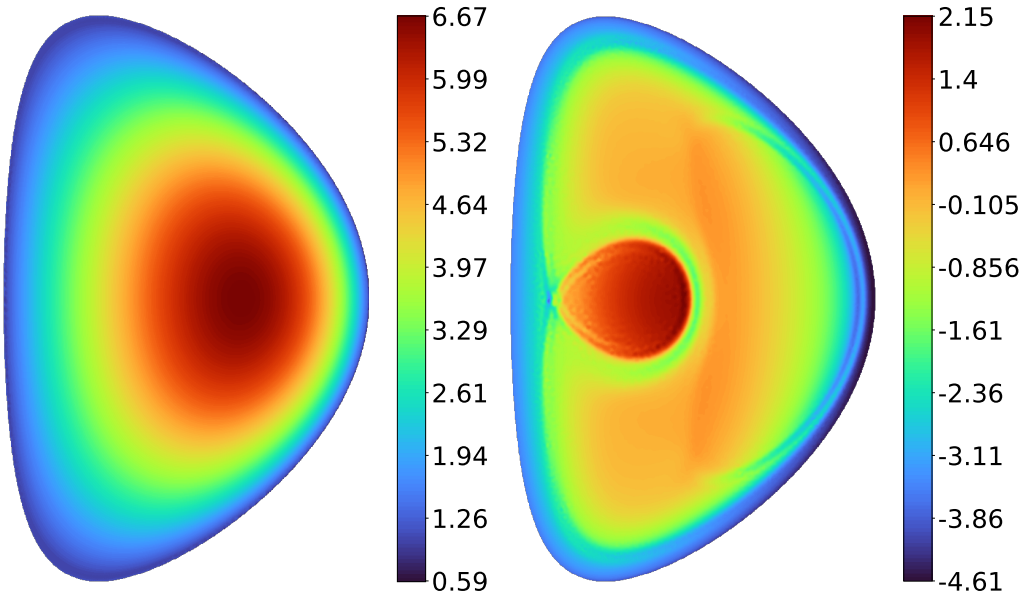

Figure 4.14: Toroidal current field with the application of the drives j_D with $A = 100$, $B = 0$ (on the left) and j_D with $A = 100$, $B = -5$ (on the right) for $H = 10^5$.

the tokamak along the toroidal direction. In these cases, part of the current flows in one direction, while another flows in the opposite direction. Different heating methods in tokamak plasma can result in scenarios where the current drive is distributed between positive and negative regions. This distribution changes the magnetic field since it is generated by the currents flowing through the plasma. Changes in the current distribution can distort the magnetic field lines, influencing plasma behaviour, including its velocity distribution. This leads to feedback effects where altered plasma dynamics further modify the magnetic field structure and current distribution, potentially amplifying the initial distribution introduced by the current drive. When the current drive is entirely in the positive or negative regions, the toroidal current drive distribution does not significantly change with an increase in the Hartmann number. However, feedback effects may cause the toroidal current to change with the Hartmann number when the drive is between positive and negative regions.

This demonstrates that the toroidal current entirely dictates the shape of the velocity. We observe no boundary layer formation with drives applied between the positive and negative regions. This is beneficial as the code appears more stable and produces robust results due to the absence of a boundary layer. However, this behaviour is challenging to predict due to the feedback effect and the various underlying processes affecting the current field, resulting in changes in the toroidal velocity distribution. There is potential to achieve much higher velocities with

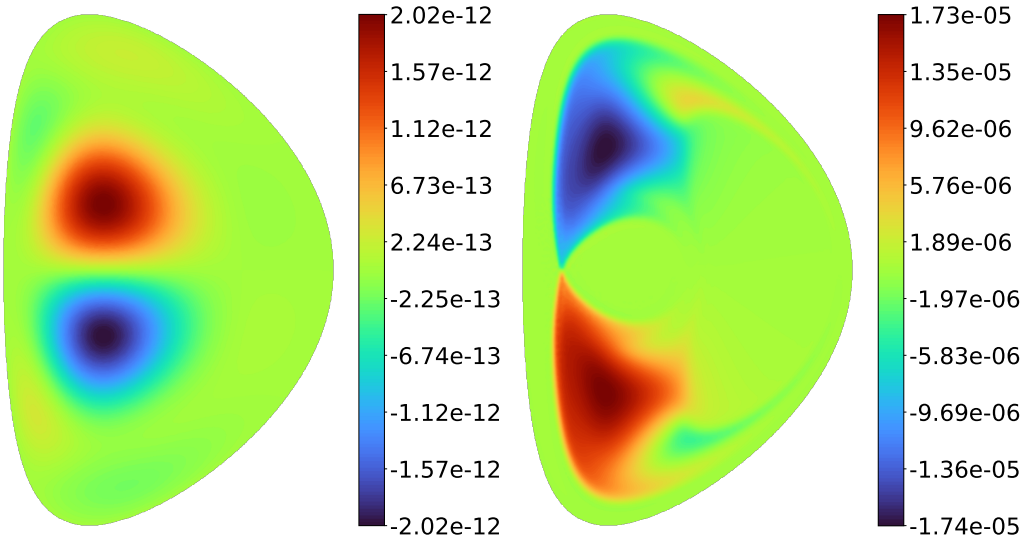

Figure 4.15: Toroidal velocity field for $H = 10$ (on the left) and $H = 10^5$ (on the right) computed with the application of the drive j_D with $A = 100$ and $B = -5$ on the toroidal current field.

such drives, but predicting precisely which drive would be optimal for maximum velocities is challenging. The nature of this feedback effect requires further study. This insight might lead to reconsidering our approach to using different heating methods for tokamak plasma and how we introduce the current drive to the system.

4.5 Conclusions

We have examined the axisymmetric steady states of tokamak plasmas using an incompressible visco-resistive MHD model. In addition to the intrinsic limitations of a MHD rather than a kinetic approach, a crucial point in the search for a relevant minimal model lies in modelling the drives at work in a tokamak device. In some previous modelings [Kamp and Montgomery, 2003, 2004; Oueslati et al., 2019; Krupka and Firpo, 2024], apart from the external, given, vacuum magnetic field, the ratio $\hat{E}_0/\eta$ was the only drive in the system. This original framework has been shown to be insufficient for achieving realistic plasma pressure levels. To address this, we have introduced additional non-inductive current drives through modifications to the toroidal current and established Poisson's equation governing the pressure profile. Our numerical simulations demonstrate that incorporating these drives enables achieving realistic orders of magnitude for the plasma pressure profiles.

We examined two families of functions for modeling tokamak drives, yet further research is needed to optimize the distribution of non-inductive current drives and

maximize their effectiveness in enhancing plasma speed and yielding fusion-relevant pressure profiles. This could involve reconsidering the application of the drive as a modification to the toroidal current due to the observed feedback effect. Toroidal current profiles were found to depend on the Hartmann number, suggesting that future implementation of these drives should involve fixed toroidal current density profiles without dependency on other system parameters. This will be addressed in the next chapter.

Bibliography

Cappello, S. and Escande, D. F. (2000). Bifurcation in Viscoresistive MHD: The Hartmann Number and the Reversed Field Pinch. *Physical Review Letters*, 85(18):3838–3841, DOI: 10.1103/PhysRevLett.85.3838.

Ferron, J. R., Lao, L. L., Taylor, T. S., Kim, Y. B., Strait, E. J., and Wroblewski, D. (1993). Improved confinement and stability in the DIII-D tokamak obtained through modification of the current profile*. *Physics of Fluids B: Plasma Physics*, 5(7):2532–2539, ISSN: 0899-8221, DOI: 10.1063/1.860740.

Forest, C. B., Kupfer, K., Luce, T. C., Politzer, P. A., Lao, L. L., Wade, M. R., Whyte, D. G., and Wròblewski, D. (1994). Determination of the noninductive current profile in tokamak plasmas. *Physical Review Letters*, 73(18):2444–2447, DOI: 10.1103/PhysRevLett.73.2444.

JET Team (1992). Fusion energy production from a deuterium-tritium plasma in the jet tokamak. *Nuclear Fusion*, 32(2):187, DOI: 10.1088/0029-5515/32/2/I01, https://dx.doi.org/10.1088/0029-5515/32/2/I01.

Kamp, L. P. and Montgomery, D. C. (2003). Toroidal flows in resistive magnetohydrodynamic steady states. *Physics of Plasmas*, 10:157–167, DOI: 10.1063/1.1524629.

Kamp, L. P. and Montgomery, D. C. (2004). Toroidal steady states in visco-resistive magnetohydrodynamics. *Journal of Plasma Physics*, 70(2):113–142, DOI: 10.1017/S0022377803002629.

Kamp, L. P., Montgomery, D. C., and Bates, J. W. (1998). Toroidal flows in resistive magnetohydrodynamic steady states. *Physics of Fluids*, 10(7):1757–1766, ISSN: 1070-6631, DOI: 10.1063/1.869692.

Kessel, C., Manickam, J., Rewoldt, G., and Tang, W. M. (1994). Improved plasma performance in tokamaks with negative magnetic shear. *Physical Review Letters*, 72(8):1212–1215, DOI: 10.1103/PhysRevLett.72.1212.

Kress, B. T. and Montgomery, D. C. (2000). Pressure determinations for incompressible fluids and magnetofluids. *Journal of Plasma Physics*, 64(4):371–377, DOI: 10.1017/S0022377800008825.

Krupka, A. and Firpo, M.-C. (2024). Scaling laws of the plasma velocity in visco-resistive magnetohydrodynamic systems. *Fundamental Plasma Physics*, 10:100044, ISSN: 2772-8285, DOI: 10.1016/j.fpp.2024.100044.

Montgomery, D. (1993). Hartmann, Lundquist, and Reynolds: The role of dimensionless numbers in nonlinear magnetofluid behavior. *Plasma Physics and Controlled Fusion*, 35(SB):B105–B113, DOI: 10.1088/0741-3335/35/SB/008.

Oueslati, H., Bonnet, T., Minesi, N., Firpo, M.-C., and Salhi, A. (2019). Numerical derivation of steady flows in visco-resistive magnetohydrodynamics for JET and ITER-like geometries with no symmetry breaking. *AIP Conference Proceedings*, 2179:020009, DOI: 10.1063/1.5135482.

Oueslati, H. and Firpo, M.-C. (2020). Breaking up-down symmetry with magnetic perturbations in tokamak plasmas: Increase of axisymmetric steady-state velocities. *Physics of Plasmas*, 27(10):102501, DOI: 10.1063/5.0016566.

Roverc'h, E., Oueslati, H., and Firpo, M.-C. (2021). Steady-state flows in a visco-resistive magnetohydrodynamic model of tokamak plasmas with inhomogeneous heating. *Journal of Plasma Physics*, 87(2):905870217, DOI: 10.1017/S0022377821000313.

Turnbull, A. D., Taylor, T. S., Lin-Liu, Y. R., and John, H. St. (1995). High beta and enhanced confinement in a second stable core VH-mode advanced tokamak. *Physical Review Letters*, 74(5):718–721, DOI: 10.1103/PhysRevLett.74.718.

Chapter 5

Effect of the fixed current profiles

> We cannot solve our problems with the same thinking we used when we created them.
>
> Albert Einstein

Contents

5.1 Introduction

The current distribution in the toroidal direction is critical to maintaining the stability and confinement of the plasma [Wesson, 2011]. Achieving a fixed toroidal current profile is a challenging but important goal in the tokamak [Taylor, 1997]. Several approaches can be used to maintain a fixed or controlled toroidal current

profile that is less dependent on plasma parameters. One of them is non-inductive current drive, which includes NBI, Electron Cyclotron Current Drive (ECCD), Lower Hybrid Current Drive (LHCD) and bootstrap current [Forest et al., 1994]. In modern tokamaks, feedback control systems actively monitor and adjust the current profile in real-time [Ravensbergen et al., 2021; Lister, 2003]. These systems rely on diagnostics to measure the current distribution. Based on these measurements, the control systems can adjust the power and localization of non-inductive current drive systems to maintain the current profile. In advanced tokamak scenarios, the goal is to achieve steady-state operation with a high fraction of the total current driven non-inductively. In experiments like JET [Romero et al., 1998], DIII-D [Ou et al., 2007], and The Experimental Advanced Superconducting Tokamak (EAST) [Wu et al., 2023], significant progress has been made in controlling the toroidal current profile using a combination of non-inductive current drive methods and feedback control systems. These experiments have demonstrated that it is possible to achieve fixed or slowly evolving current profiles, even in high-performance plasmas.

In the previous chapter, we observed that the Hartmann number affects the toroidal current profiles. To address this issue, we will introduce toroidal current profiles independent of any system parameters. In this chapter, we will assume that the toroidal current profiles are fixed, following the shape of the drive introduced earlier and serving as a solution to a simplified Poisson's equation. This can be interpreted as a model of fully non-inductive operation. The current profiles will exhibit a parabolic distribution across the plasma cross-section, independent of the Hartmann number or other system parameters. With this assumption, we will investigate a new toroidal velocity distribution that does not form a boundary layer and will establish a new scaling law in the second regime.

The chapter is organized as follows: Section 5.2 presents a new system of equations in 5.2.1 and the results obtained with the assumption of the fixed current profiles in Section 5.2.2. Then, we proceed with the prediction of the scaling law in Section 5.3.1 and its numerical estimation in Section 5.3.2. The chapter also discusses the effect of the non-nested magnetic flux surfaces in Section 5.4 and non-linear effects in Section 5.5. Finally, a conclusive Section 5.6 summarizes the outcomes of this chapter.

5.2 Visco-resistive MHD framework

5.2.1 New system of equations

As observed in the previous Chapter 4, current profile distributions can vary across different Hartmann numbers. At high Hartmanns with toroidal current drive, current distribution remains inconsistent due to the feedback effects. In this study, we ensure that the toroidal current profiles remain fixed and unaffected by other system parameters. To achieve this, we assume the toroidal current has a

parabolic distribution, derived from the solution of the simple Poisson's equation $\nabla^2 j_{fixed} = -A$ with the boundary condition $j_{fixed} = B$ on $\partial\Omega$, where A represents the magnitude of the parabolic function, and B is an offset. Thus, instead of deriving the toroidal current density as the toroidal projection of Ohm's law (as was done in previous works), we assume it to be equal to j_{fixed}.

The system of equations (4.1)-(4.6) in variables $u_1, ..., u_6$ with the new modification will read as follows:

$$\triangle^* u_1 = -u_2, \tag{5.1}$$

$$\nu\triangle^* u_2 = \frac{1}{x^2}\frac{\partial}{\partial y}(u_3^2 - u_4^2) + \frac{1}{x}\{u_6, u_5\} + \frac{1}{x}\{u_1, u_2\} + \tag{5.2}$$

$$+ \frac{2u_2}{x^2}\frac{\partial u_1}{\partial y} - \frac{2u_6}{x^2}\frac{\partial u_5}{\partial y}, \tag{5.3}$$

$$\eta\triangle^* u_3 = \frac{1}{x}\{u_1, u_3\} + \frac{1}{x}\{u_4, u_5\} + \frac{2u_3}{x^2}\frac{\partial u_1}{\partial y} - \frac{2u_4}{x^2}\frac{\partial u_5}{\partial y}, \tag{5.4}$$

$$\nu\triangle^* u_4 = \frac{1}{x}\{u_1, u_4\} + \frac{1}{x}\{u_3, u_5\}, \tag{5.5}$$

$$\triangle^* u_5 = -u_6 \tag{5.6}$$

with

$$u_6 = x j_{fixed}. \tag{5.7}$$

The following section will present the numerical results of the simulations under the new assumption of the fixed toroidal current profiles.

5.2.2 Controlled current distribution

We will now investigate the application of j_{fixed} as a toroidal current with different magnitudes A and offsets B while keeping the total current constant. The realistic current values are derived from the Kamp and Montgomery model [Kamp and Montgomery, 2004] as the choice of the drive E_0/η of order 1 produced a total current relevant to real operating tokamaks. Let us examine the toroidal current profiles with $A = 32$, $B = 0$ since this choice of magnitude and offset produces a realistic total current with the boundary condition $j_\varphi = 0$. Figure 5.1 presents the toroidal current distribution with Hartmann numbers $H = 10$ and $H = 10^5$.

Let us investigate the velocity behaviour under this assumption: Figure 5.2 presents toroidal velocity distribution with a fixed toroidal current with $A = 32$ and $B = 0$. At $H = 10$, the velocity distribution behaves similarly to the previous results with no fixed current profiles made in Chapter 3. However, at $H = 10^5$, a different behaviour is observed: the boundary layer no longer forms.

To understand the velocity behaviour in this context, we examine the root-mean-square of the toroidal velocities at various Hartmann numbers in Figure 5.3. In this analysis, we adjust the values of A and B to ensure the total current

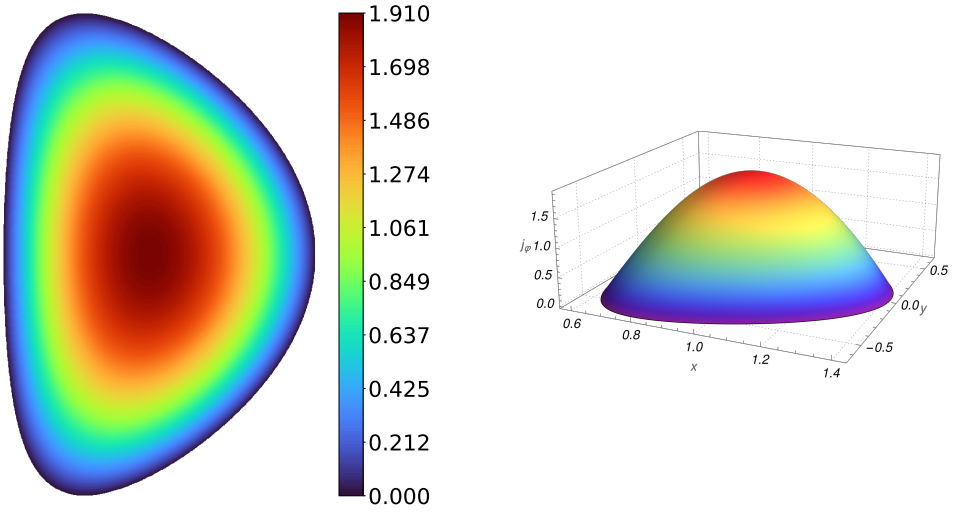

Figure 5.1: Toroidal current field for $H = 10$ (on the left) and $H = 10^5$ (on the right) computed with fixed toroidal current profiles with $A = 32$ and $B = 0$.

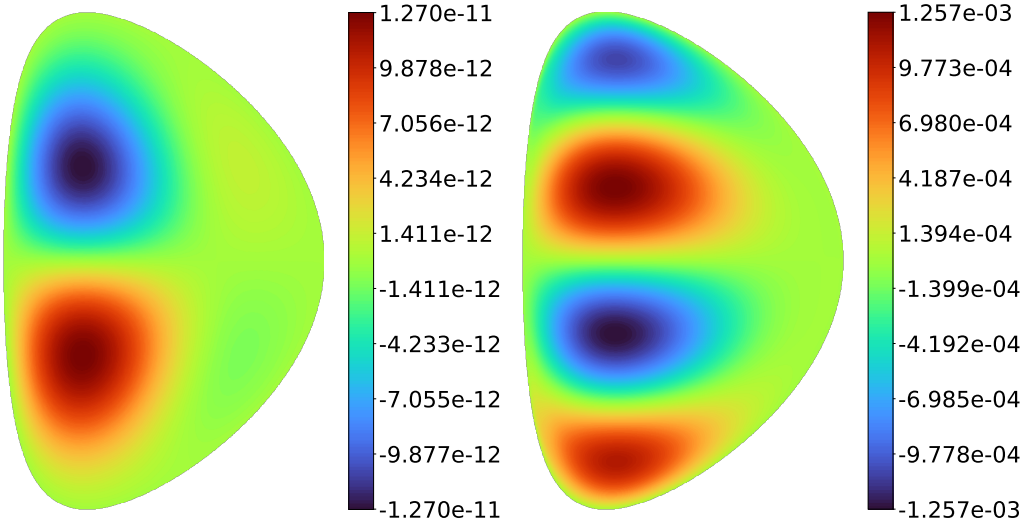

Figure 5.2: Toroidal velocity field for $H = 10$ (on the left) and $H = 10^5$ (on the right) computed with fixed toroidal current profiles with $A = 32$ and $B = 0$.

remains constant. It is evident that the velocities gradually increase with the magnitude of A, developing into two distinct regimes with different scaling laws. A comprehensive discussion of plasma velocity regimes, including the derivation of scaling laws for velocities as a function of the Hartmann number, is provided in [Krupka and Firpo, 2024; Kamp et al., 1998; Kamp and Montgomery, 2003] and the Chapter 3. In the limit $H \ll 1$, we observe that the first regime matches the no-drive case, and the inter-regime is maintained. However, instead of transitioning to the boundary layer regime in the limit $H \gg 1$, the boundary layer does not form, and a new regime emerges.

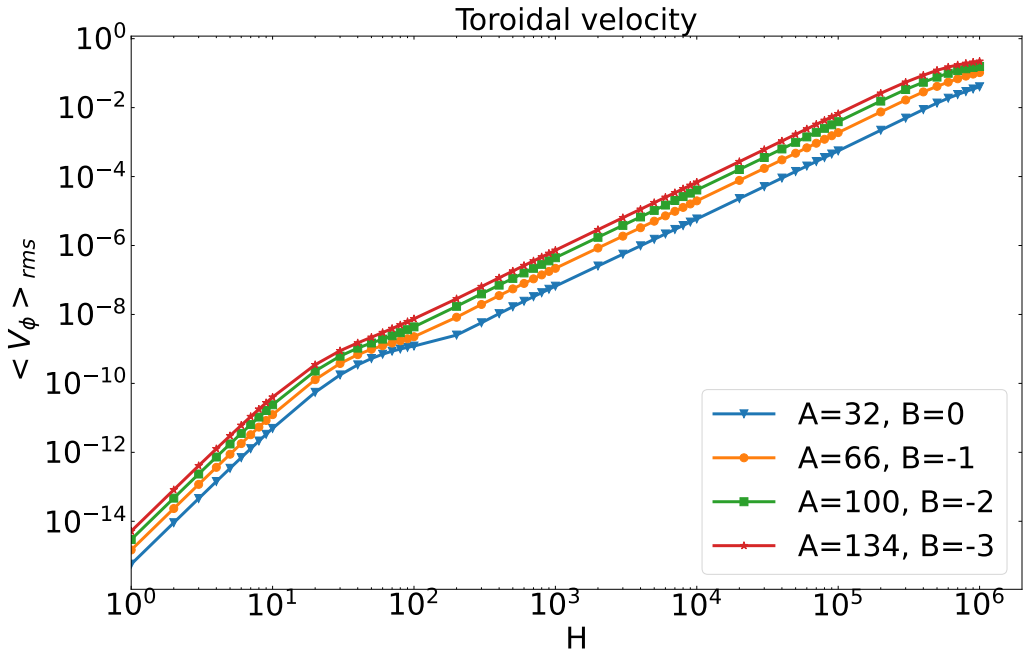

Figure 5.3: Root-mean-square of toroidal velocity in Alfvèn velocity units as a function of the Hartmann number, with fixed toroidal current profiles for different values of positive magnitude A and B.

Let us also investigate the root-mean-square of the toroidal and poloidal velocities with different numbers of mesh triangles to demonstrate the numerical robustness of these results, as shown in Figure 5.4. It can be seen that the results are highly stable, showing no discrepancy based on the number of triangles. This stability is attributed to the absence of the boundary layer, which previously posed significant challenges in resolving thin boundary layers in our earlier works.

We need to estimate the scaling law for the newly emerged second regime to understand the velocity behaviour.

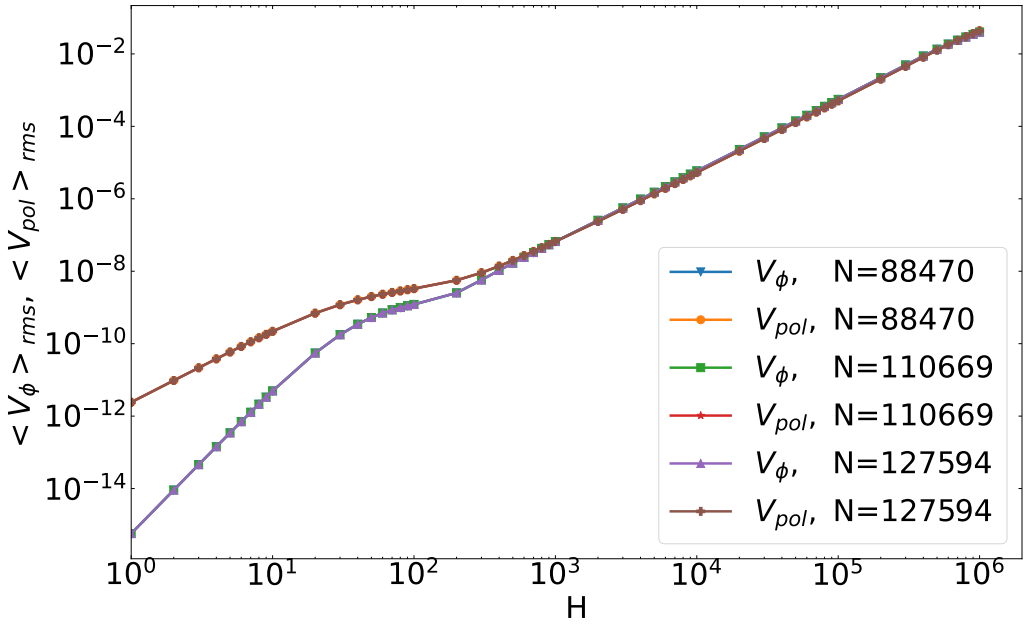

Figure 5.4: Root-mean-square of toroidal and poloidal velocities as a function of the Hartmann number in Alfvén velocity units with fixed toroidal current profiles with $A = 32$, and $B = 0$ for different numbers of triangles.

5.3 Scaling law in the limit $H \gg 1$ without the boundary layer

5.3.1 Prediction of the scaling law

As the velocities in the second regime appear to scale with the Hartmann number, we aim to estimate the scaling law by drawing an analogy with the works of Kamp and Montgomery [Kamp and Montgomery, 2003; Montgomery et al., 1997]. We can identify two regimes: the scaling of the first regime was already predicted in [Kamp and Montgomery, 2003], where the toroidal velocities scale with the Hartmann number as H^4 and the poloidal velocities as H^2. They considered the "slow-flow" equations in the high-viscosity limit ($H \ll 1$), leading to the following system of equations derived from (2.44)-(2.49):

$$\triangle^* u_1 = -u_2, \tag{5.8}$$

$$\nu \triangle^* u_2 = -\frac{E_0}{\eta} \frac{2}{x^2} \frac{\partial u_5}{\partial y}, \tag{5.9}$$

$$\triangle^* u_5 = -u_6. \tag{5.10}$$

$$\tag{5.11}$$

In this limit, the viscous term dominates over the non-linear term in the Navier-Stokes equation, and the term E_0/η is much larger than the $\boldsymbol{v} \times \boldsymbol{B}$ term in Ohm's law. We also direct the Reader to Appendix C for a full derivation of the velocities in the first regime. The prediction and confirmation of the second regime scaling with ($H \gg 1$) was already made in Chapter 3, which showed that in the boundary layer regime, the toroidal and poloidal velocities scale as $H^{1/4}$.

Since, in the case of fixed toroidal current, the boundary layer regime does not appear, a new scaling derivation is necessary to understand the behaviour of the velocities. We make several assumptions: we do not consider the low-viscosity limit, as it is impossible to scale velocity with viscosity or the Hartmann number. However, the non-linear term remains small compared to the other terms in the Navier-Stokes equation, so we will diminish it. Additionally, the $\boldsymbol{v} \times \boldsymbol{B}$ term is no longer retained in the sixth equation since the shape of the toroidal current is prescribed to be independent of the Hartmann number and other system parameters. However, it is retained in the third equation, where we take the curl of Ohm's law. Consequently, the system of equations now takes the form:

$$\triangle^* u_1 = -u_2, \tag{5.12}$$

$$\nu \triangle^* u_2 = \frac{1}{x^2}\frac{\partial}{\partial y}(u_3^2) + \frac{1}{x}\{u_6, u_5\} - \frac{2u_6}{x^2}\frac{\partial u_5}{\partial y}, \tag{5.13}$$

$$0 = \frac{1}{x}\{u_1, u_3\} + \frac{1}{x}\{u_4, u_5\} + \frac{2u_3}{x^2}\frac{\partial u_1}{\partial y} - \frac{2u_4}{x^2}\frac{\partial u_5}{\partial y}, \tag{5.14}$$

$$\nu \triangle^* u_4 = \frac{1}{x}\{u_3, u_5\}, \tag{5.15}$$

$$\triangle^* u_5 = -u_6, \tag{5.16}$$

$$\tag{5.17}$$

with

$$u_6 = j_{fixed}. \tag{5.18}$$

Since u_6 does not scale with the Hartmann number, according to Equation (5.16), neither does u_5. From Equation (5.15), u_3 scales as νu_4. Substituting this into Equation (5.14) reveals that u_1 scales as $1/\nu$, meaning that the scaling for the poloidal velocity is H^2. From Equation (5.12), u_1 scales as u_2, and from Equation (5.13), we find that u_3 does not scale with the Hartmann number. Finally, using Equation (5.15), we estimate that u_4 scales as $1/\nu$. Therefore, we conclude that the poloidal and toroidal velocity scaling in this approximation is H^2.

5.3.2 Numerical estimation of the scaling laws

Let us estimate the scaling laws of the velocity in two regimes by using a power-law fitting. In Figure 5.5, it can be seen that in the limit, as the Hartmann number H approaches zero for the first regime, the velocity follows the pattern $f(H)$, with

f approximately equal to H^4 for toroidal velocity and H^2 for poloidal velocity. The velocities scale as H^2 in the second regime. It corresponds to the analytical predictions made above.

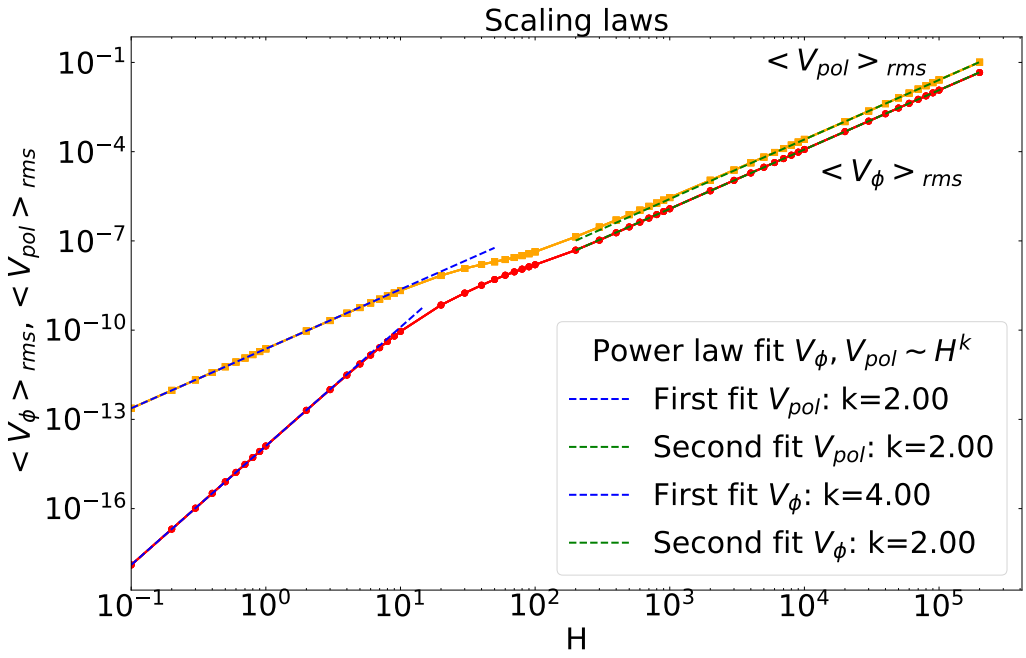

Figure 5.5: Root-mean-square of toroidal and poloidal velocities in Alfvén velocity units as a function of the Hartmann number in log-log scale with power-law fitting curves.

5.4 Non-nested magnetic field lines

Let us further explore how velocity distributes within the tokamak plasma domain under various current profiles. We will consider slightly different magnitudes and drives, ensuring the magnitude is negative while the offset remains positive. This approach will allow us to maintain a constant total current. Figure 5.6 presents results similar to Figure 5.3, but with different values of A and B. It can be seen that as the negative magnitude increases, the transition between the first and second regimes becomes smoother.

This transition between the first and second regimes can be explained by examining the magnetic flux surfaces for three specific cases: a fixed toroidal current with a) $A = -2$, $B = 1$; b) $A = -36$, $B = 2$; and c) $A = -70$, $B = 3$. These configurations are illustrated in Figure 5.7. As we increase the negative magnitude A and the positive offset B, the nested magnetic flux surfaces transform

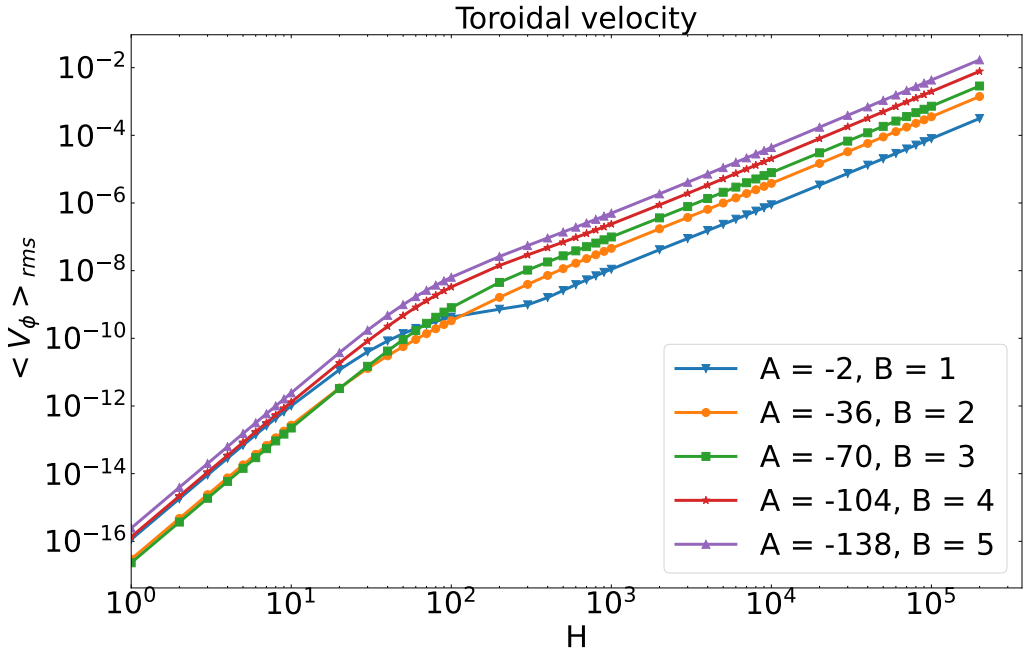

Figure 5.6: Root-mean-square of toroidal velocity in Alfvèn velocity units as a function of the Hartmann number, with fixed toroidal current profiles for different values of negative magnitude A and B.

into non-nested surfaces. In the final case, this transformation leads to the gradual appearance of magnetic islands.

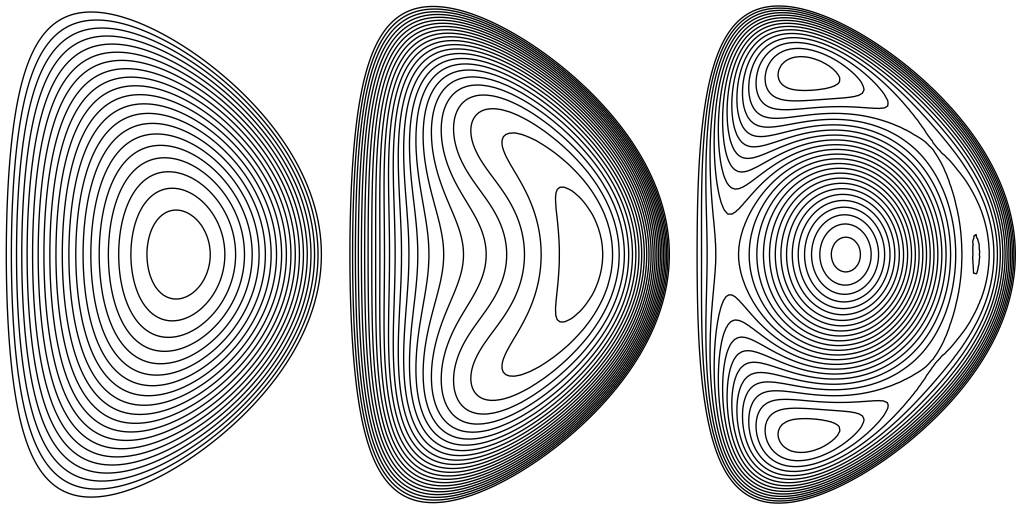

Figure 5.7: Magnetic flux surfaces with internal separatrices computed with fixed toroidal current profiles with a) $A = -2$, $B = 1$ (on the left), b)$A = -36$, $B = 2$ (in the middle) and c) $A = -70$, $B = 3$ (on the right) for $H = 10^5$.

Now, let us examine the toroidal velocity field with fixed current profiles for the case of $A = -104$ and $B = 4$, as shown in Figure 5.8. It can be seen that the non-nested magnetic field lines generated by these toroidal current profiles begin to alter the toroidal velocity distribution even at small Hartmann numbers of $H = 10$. As the Hartmann number increases to $H = 10^5$, the velocity profile evolves further, developing three distinct vortices.

5.5 Non-linear effects

In Section 3.3, we confirmed that the non-linear term did not contribute to the toroidal velocity, and the discrepancy observed in Figure 3.4 was not caused by the dominance of the inertial effect. However, with the new system of equations (5.12-5.18), where the boundary layer does not form, it is necessary to examine the behaviour of the $(\mathbf{j} \times \mathbf{b}) \cdot \mathbf{i}_\varphi$ term and the non-linear $(\boldsymbol{\omega} \times \mathbf{v}) \cdot \mathbf{i}_\varphi$ term.

Now we will depict the contribution of the $(\mathbf{j} \times \mathbf{b}) \cdot \mathbf{i}_\varphi$ terms to the total toroidal velocity for $H = 10$ and $H = 10^5$. Figure 5.9 presents this result.

Next, let us consider the non-linear term contribution: Figure 5.10 shows the $(\boldsymbol{\omega} \times \mathbf{v}) \cdot \mathbf{i}_\varphi$ term contribution to the total toroidal velocity for $H = 10$ and $H = 10^5$.

It can be seen that at the small Hartmann number $H = 10$, the velocities are driven by the $(\mathbf{j} \times \mathbf{b}) \cdot \mathbf{i}_\varphi$ term, which is consistent with the previous results

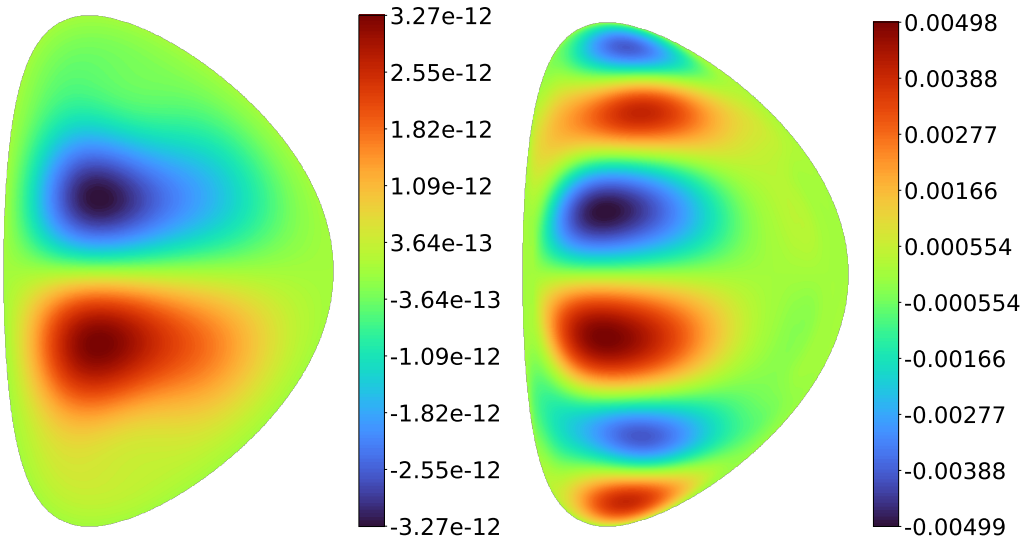

Figure 5.8: Toroidal velocity field for $H = 10$ (on the left) and $H = 10^5$ (on the right) computed with fixed toroidal current profiles with $A = -104$ and $B = 4$.

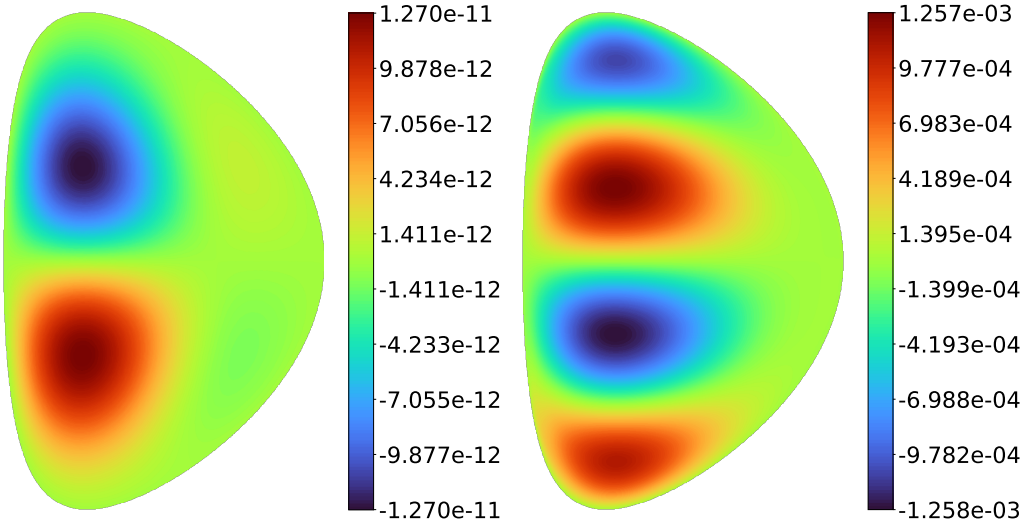

Figure 5.9: Contribution of the $(\mathbf{j} \times \mathbf{b}) \cdot \mathbf{i}_\varphi$ term to the total toroidal velocity for $H = 10$ (on the left) and $H = 10^5$ (on the right).

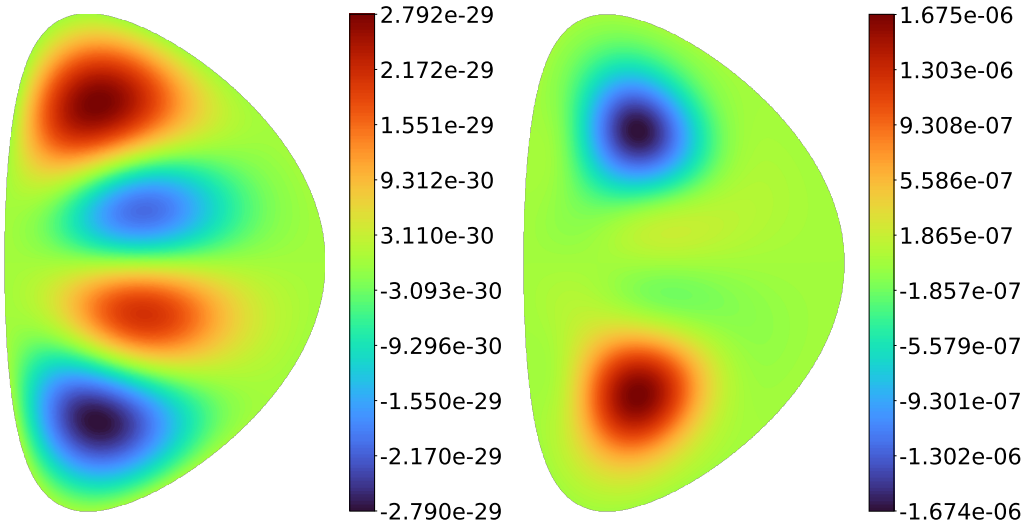

Figure 5.10: Contribution of the $(\boldsymbol{\omega} \times \mathbf{v}) \cdot \mathbf{i}_\varphi$ term to the total toroidal velocity for $H = 10$ (on the left) and $H = 10^5$ (on the right).

obtained in Chapter 3. However, the non-linear term becomes significantly larger at higher Hartmann numbers. To further understand the inertial and magnetic components, we examine the root-mean-square of the toroidal and poloidal parts of the $\boldsymbol{\omega} \times \mathbf{v}$ and $\mathbf{j} \times \mathbf{b}$ terms as a function of the Hartmann number. These results are shown in Figure 5.11.

We can see here that with fixed current profiles and the development of the new scaling regime, the non-linear term grows faster than the magnetic term. The point at which the non-linear term starts to dominate is a point when the simulations crash. Let us finally look at the $\boldsymbol{\omega} \times \mathbf{v}$ and $\mathbf{j} \times \mathbf{b}$ terms at the point where their root-mean-square values intersect. Figure 5.12 presents this information. It can be seen that velocities at Hartmann number $H = 10^6$ are driven by some non-linear behaviour, making it difficult to distinguish between magnetic and inertial effects. This suggests that the results presented here may be unstable and unreliable.

The absence of boundary layers and the dominance of the non-linear term suggest that the simulation is entering a regime where inertial effects are significant, potentially leading to turbulence. In such regimes, where the non-linear term dominates, the simulation might require even finer spatial resolution to capture the dynamics accurately. As this work does not aim to investigate the formation of the instabilities or turbulence in the tokamak plasma, we will not go into detail about the nature of this phenomenon. Further research is needed to investigate the effect of the non-linear term and adapt the simulations and code to study this problem in more detail. In summary, under the assumption of fixed current profiles, a new regime emerges in the limit of large Hartmann numbers, where non-linear effects grow much faster than in the boundary layer regime, even reaching the magnitude

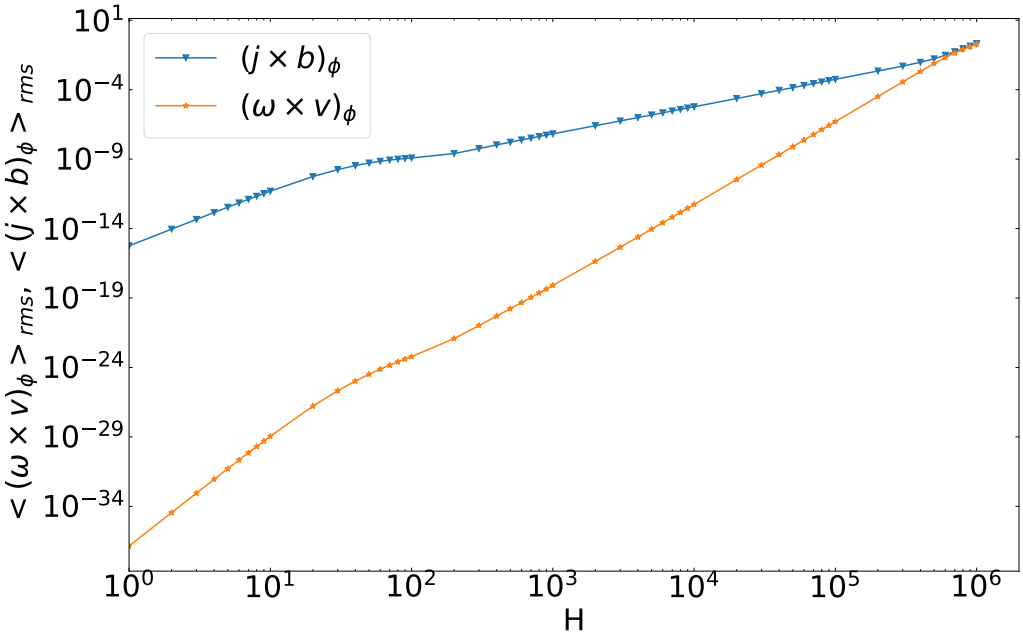

Figure 5.11: Root-mean-square of toroidal part of $\boldsymbol{\omega} \times \mathbf{v}$ and $\mathbf{j} \times \mathbf{b}$ terms as a function of the Hartmann number in Alfvén velocity v_{A0}.

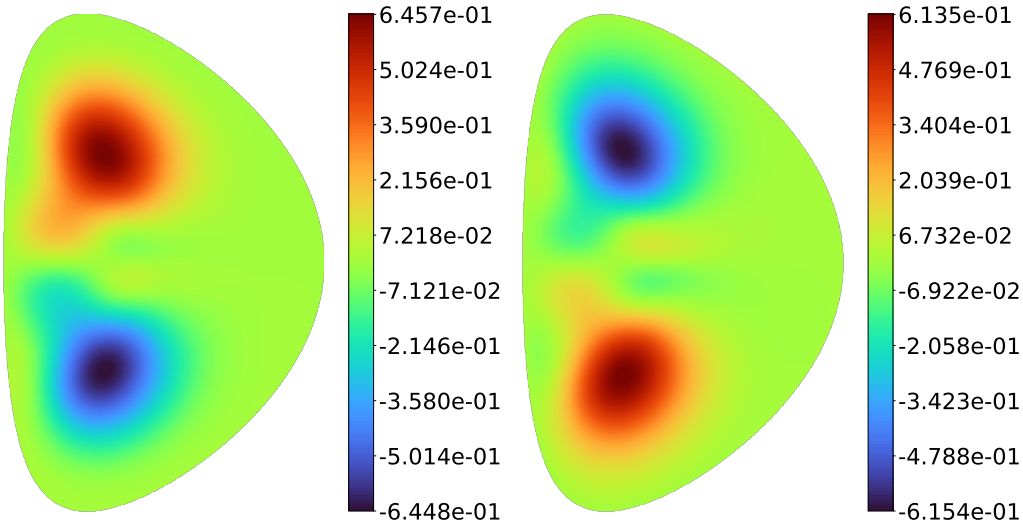

Figure 5.12: Contribution of the $\mathbf{j} \times \mathbf{b}$ term (on the left) and $\boldsymbol{\omega} \times \mathbf{v}$ term (on the right) to the total toroidal velocity for $H = 10^6$.

of the magnetic term.

5.6 Conclusions

This chapter investigates a new approach where the toroidal current profiles are fixed and independent of other system parameters. This assumption was introduced to eliminate the feedback effect presented in Chapter 4. With this assumption, a new scaling regime emerges in the limit of large Hartmann numbers, $H \gg 1$, which cannot be scaled with the previous scaling derived in Chapter 3. As no boundary layer forms in the toroidal velocity, we predict a new scaling law. This chapter reveals that the new scaling law for the toroidal and poloidal velocities should follow an H^2 pattern in this new regime, confirmed through numerical simulations. Additionally, we examined the effect of the magnitude and offset of the drive on the toroidal velocity distribution while maintaining the same total current.

The transition to non-nested magnetic field lines was also investigated, revealing that the appearance of magnetic islands does not affect the scaling of the first and second regimes but does impact the transition between them. This transition becomes smoother, potentially allowing for even higher plasma rotation. Furthermore, the non-linear effect was investigated, concluding that our simulation stopped calculating when the inertial terms began to dominate over the magnetic term. The overall velocity reaches the desirable levels of 1 % of Alfvén Mach number needed to stabilize external modes according to [Bondeson and Ward, 1994; Takechi et al., 2007; Sabbagh et al., 2006].

Bibliography

Bondeson, A. and Ward, D. J. (1994). Stabilization of external modes in tokamaks by resistive walls and plasma rotation. *Physical Review Letters*, 72(17):2709–2712, DOI: 10.1103/PhysRevLett.72.2709.

Forest, C. B., Kupfer, K., Luce, T. C., Politzer, P. A., Lao, L. L., Wade, M. R., Whyte, D. G., and Wròblewski, D. (1994). Determination of the noninductive current profile in tokamak plasmas. *Physical Review Letters*, 73(18):2444–2447, DOI: 10.1103/PhysRevLett.73.2444.

Kamp, L. P. and Montgomery, D. C. (2003). Toroidal flows in resistive magnetohydrodynamic steady states. *Physics of Plasmas*, 10:157–167, DOI: 10.1063/1.1524629.

Kamp, L. P. and Montgomery, D. C. (2004). Toroidal steady states in visco-resistive magnetohydrodynamics. *Journal of Plasma Physics*, 70(2):113–142, DOI: 10.1017/S0022377803002629.

Kamp, L. P., Montgomery, D. C., and Bates, J. W. (1998). Toroidal flows in resistive magnetohydrodynamic steady states. *Physics of Fluids*, 10(7):1757–1766, ISSN: 1070-6631, DOI: 10.1063/1.869692.

Krupka, A. and Firpo, M.-C. (2024). Scaling laws of the plasma velocity in visco-resistive magnetohydrodynamic systems. *Fundamental Plasma Physics*, 10:100044, ISSN: 2772-8285, DOI: 10.1016/j.fpp.2024.100044.

Lister, J. B. (2003). The evolution of feedback control in tokamaks. https://cds.cern.ch/record/924869.

Montgomery, D., Bates, J. W., and Li, S. (1997). Toroidal vortices in resistive magnetohydrodynamic equilibria. *Physics of Fluids*, 9(4):1188–1193, ISSN: 1070-6631, DOI: 10.1063/1.869206.

Ou, Y., Luce, T., Schuster, E., Ferron, J., Walker, M., Xu, C., and Humphreys, D. (2007). Towards model-based current profile control at diii-d. *Fusion Engineering and Design*, 82(5):1153–1160, ISSN: 0920-3796, DOI: https://doi.org/10.1016/j.fusengdes.2007.04.016, https://www.sciencedirect.com/science/article/pii/S0920379607001755. Proceedings of the 24th Symposium on Fusion Technology.

Ravensbergen, T., van Berkel, M., Perek, A., Galperti, C., Duval, B. P., Février, O., van Kampen, R. J. R., Felici, F., Lammers, J. T., Theiler, C., Schoukens, J., Linehan, B., Komm, M., Henderson, S., Brida, D., and de Baar, M. R. (2021). Real-time feedback control of the impurity emission front in tokamak divertor plasmas. *Nature Communications*, 12(1):1105, DOI: 10.1038/s41467-021-21268-3.

Romero, J., de la Cruz, J., Dobbing, T., Ellis, J., Fisher, B., King, Q., Söldner, F., and Zornig, N. (1998). Real time current profile control at jet. *Fusion Engineering and Design*, 43(1):37–58, ISSN: 0920-3796, DOI: https://doi.org/10.1016/S0920-3796(98)00261-0, https://www.sciencedirect.com/science/article/pii/S0920379698002610.

Sabbagh, S. A., Bell, R. E., Menard, J. E., Gates, D. A., Sontag, A. C., Bialek, J. M., LeBlanc, B. P., Levinton, F. M., Tritz, K., and Yuh, H. (2006). Active stabilization of the resistive-wall mode in high-beta, low-rotation plasmas. *Physical Review Letters*, 97(4):045004, DOI: 10.1103/PhysRevLett.97.045004.

Takechi, M., Matsunaga, G., Aiba, N., Fujita, T., Ozeki, T., Koide, Y., Sakamoto, Y., Kurita, G., Isayama, A., and Kamada, Y. (2007). Identification of a low plasma-rotation threshold for stabilization of the resistive-wall mode. *Physical Review Letters*, 98(5):055002, DOI: 10.1103/PhysRevLett.98.055002.

Taylor, T. S. (1997). Physics of advanced tokamaks. *Plasma Physics and Controlled Fusion*, 39(12B):B47, DOI: 10.1088/0741-3335/39/12B/005, https://dx.doi.org/10.1088/0741-3335/39/12B/005.

Wesson, J. A. (2011). *Tokamaks*. Oxford University Press, Oxford, 4th edition, ISBN: 9780199592234.

Wu, K., Yuan, Q., Eldon, D., Li, K., Duan, Y., Meng, L., Wang, L., Wang, H., Huang, J., Zhang, L., Luo, Z., Liu, X., Cao, B., Liu, J., Ding, F., Xu, G., Hu, J., Xiao, B., Calabrò, G., and Innocente, P. (2023). The first achievement of the double feedback control of the detachment in the long-pulse plasma on east. *Nuclear Materials and Energy*, 34:101398, ISSN: 2352-1791, DOI: https://doi.org/10.1016/j.nme.2023.101398, https://www.sciencedirect.com/science/article/pii/S2352179123000376.

Chapter 6

General conclusions and perspectives

Science is not finished until it is communictated.

Sir Mark Walport

Magnetic confinement is a complex problem due to plasma turbulence and instabilities that can occur inside the tokamak device. Plasma rotation is crucial in stabilizing the plasma and mitigating these instabilities. The main goal of this work is to understand and enhance plasma rotation in a tokamak device to improve confinement and overall performance. To achieve this, we develop a visco-resistive magnetohydrodynamic model that allows us to study steady-state plasma behavior without assuming zero plasma velocity.

6.1 Key findings

In this work, we have explored the scaling laws governing plasma velocity in a tokamak device. Using a visco-resistive MHD model applied to a tokamak plasma with a prescribed toroidal current drive, we successfully predicted and numerically confirmed a scaling law for the plasma velocity. This scaling law depends on the resistivity, η, and the Hartmann number, H, where H is defined as $H \equiv (\eta\nu)^{-1/2}$, with ν representing viscosity. Our results show that the velocity scales as $\eta f(H)$, where f is a specific function. Notably, this scaling law holds as long as the inertial term $\boldsymbol{\omega} \times \mathbf{v}$ remains negligible, which is true for the highest numerically accessible Hartmann number values.

Within this general scaling law, two limiting regimes were identified for low and high H, where the function f follows a power-law behaviour. Various boundary conditions applied to the toroidal velocity and vorticity did not affect the scaling laws. By varying the drive of the system, E_0/η, a new scaling law in H emerged for small E_0/η values. This new scaling regime is an intermediate case between the low and high H regimes and does not involve a boundary layer. The critical influence of the E_0/η ratio on the toroidal velocity regimes, scaling laws, and boundary layer formation was highlighted.

However, the plasma velocity predicted by our model remains relatively low compared to both experimental observations and the velocities required to suppress instabilities. Several factors could explain this. First, our model may lack turbulence due to its axisymmetric and 2D nature and the absence of symmetry-breaking effects. Furthermore, a limiting factor may be using an MHD model instead of a kinetic one. Additionally, there may be limitations in how we describe the plasma heating drive. It is important to note that we focused intentionally on axisymmetric scenarios to investigate plasma rotation and its potential to mitigate 3D instabilities.

A tokamak's accurate representation of drives is essential in pursuing a minimal model. Earlier models have only considered the ratio $\hat{E}_0/\eta$ as the driving force and the external vacuum magnetic field. However, this method has proven insufficient in achieving realistic plasma pressure levels. We introduced additional non-inductive current drives to overcome this limitation by adjusting the toroidal current and incorporating Poisson's equation for the pressure profile. Our numerical simulations show that these added drives allow us to achieve more realistic plasma pressure profiles.

We explored two families of functions to model the tokamak drives, but further investigation is required to optimize the distribution of non-inductive current drives and enhance their effectiveness in boosting plasma velocity and achieving fusion-relevant pressure profiles. This may involve reconsidering the application of the drive as a modification to the toroidal current, given the observed feedback effects. We found that the toroidal current profiles vary with the Hartmann number, indicating that future implementations should use fixed toroidal current density profiles that do not depend on other system parameters.

We explored a novel approach where the toroidal current profiles are fixed and independent of other system parameters. This assumption was introduced to eliminate the feedback effect. Under this assumption, a new scaling regime emerges for large Hartmann numbers, $H \gg 1$, which the previous scaling laws cannot describe. Since no boundary layer forms in the toroidal velocity, we predict a new scaling law based on a few new assumptions. In this new regime, we demonstrated that the scaling law for toroidal and poloidal velocities should follow an H^2 pattern, a result confirmed by numerical simulations. Additionally, we analyzed the impact of the drive's magnitude and offset on the toroidal velocity distribution while keeping the total current constant.

We also investigated the transition to non-nested magnetic field lines, finding that while the formation of magnetic islands does not affect the scaling of the first and second regimes, it does influence the transition between them. This transition becomes smoother, potentially allowing for even higher plasma rotation. Furthermore, we examined non-linear effects, concluding that our simulations terminated when the inertial terms began to dominate over the magnetic ones. The overall velocity reaches the desirable levels of about 1 % of Alfvén Mach number, as required to stabilize external modes according to [Bondeson and Ward, 1994; Takechi et al., 2007; Sabbagh et al., 2006].

6.2 Comparison of assumptions

With these key findings of this thesis, I will now provide a final comparison of the assumptions made. Figure 6.1 illustrates the root-mean-square of the toroidal velocity as a function of the Hartmann number for these three different assumptions.

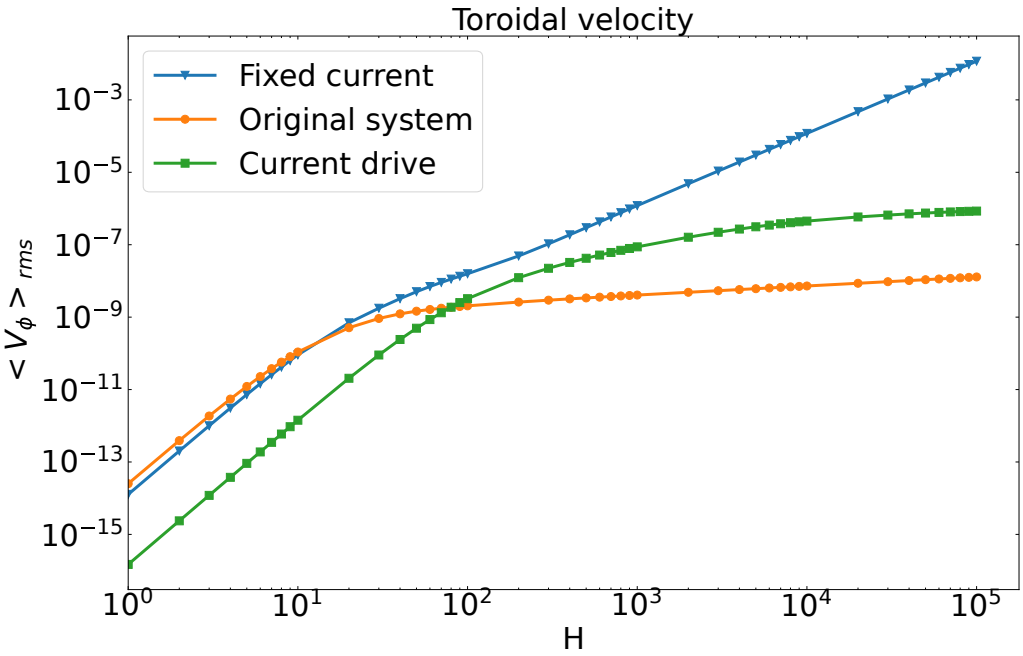

Figure 6.1: Root-mean-square of toroidal velocity in Alfvén velocity units as a function of the Hartmann number, plotted on a log-log scale, for three assumptions: no toroidal current drive, with toroidal current drive, and fixed current profiles.

The "Original system" case represents the scenario where the toroidal current field is derived purely from Ohm's law. This classical assumption results in forming a boundary layer but does not produce realistic plasma pressure levels. The "Current drive" assumption incorporates an additional toroidal current drive,

modifying the toroidal current and making the model more complex. This approach yields more realistic plasma pressure levels. Finally, the "Fixed current" assumption involves setting fixed toroidal current profiles independent of other system parameters. This approach results in the highest plasma rotation levels.

The findings suggest that the fixed toroidal current profiles assumption is the most effective for enhancing plasma rotation and producing fusion-relevant pressure profiles.

6.3 Implications and impact

This thesis can potentially impact the field of magnetic confinement fusion by offering a fresh perspective on plasma rotation and its critical role in stabilizing plasmas. Most theoretical magnetic plasma confinement communities use a kinetic approach to describe tokamak plasmas. This method has the drawback of potentially overlooking intrinsic plasma rotation. In contrast, this work does not assume that plasma rotation comes from turbulence, thus avoiding the assumption of zero plasma velocity. Instead, it introduces an alternative description of the plasma using the visco-resistive MHD framework.

The foundational model, initially developed by [Kamp and Montgomery, 2003, 2004; Kamp et al., 1998], has been extended in this work by addressing two significant issues: the lack of a current drive and the unrealistically small pressure profiles in the system. One of the key contributions of this thesis is the analytical prediction and numerical validation of scaling laws for plasma velocity. Understanding scaling laws is essential for optimizing tokamak performance and enhancing plasma stability. These laws allow us to predict how changes in system parameters will affect plasma behaviour, ensuring that reactors can achieve the conditions for sustained nuclear fusion.

Additionally, this thesis derives Poisson's equation for the pressure of the system. This is a novel development within the visco-resistive framework. Knowing pressure provides valuable insight into the system, enabling a more comprehensive understanding of plasma behaviour beyond just plasma velocity.

Another significant contribution is the introduction of the fixed toroidal current profiles assumption, which leads to higher plasma rotation levels. While controlling feedback effects in toroidal current profiles is not entirely new, this work highlights the significance of fixed current profiles from an MHD perspective. The fixed current profiles assumption could be a game-changer in magnetic confinement fusion, offering a new approach to enhancing plasma rotation and achieving fusion-relevant pressure profiles.

6.4 Future research directions

Given the rapid growth of non-linear effects observed with fixed current profiles, a more detailed investigation into these effects is essential. Our simulations stopped when the non-linear terms became dominant over the magnetic ones. Extending simulations to higher values of the Hartmann number would help better understand plasma behaviour in this regime. This could be achieved through more detailed meshing or by conducting more precise calculations, particularly in the high Hartmann number zone. This would involve smaller iteration steps or improved accuracy in the Newton-Raphson method.

Another promising direction for research would be a deeper exploration of the inter-regime between low and high Hartmann numbers. The new scaling law identified in this region could be further studied to understand plasma dynamics better. This transitional regime, discussed in Chapter 3, was found to be responsible for the boundary layer formation in the toroidal velocity. The drive of the system E_0/η plays a crucial role in forming the boundary layer. By varying this parameter, the inter-regime can be extended, and it may be possible to predict another scaling law in this region. However, extensive numerical investigations will be required to fully understand the underlying processes at work in this intermediate regime.

In Chapter 5, we also discovered that the magnetic configuration of the system influences this inter-regime. The formation of magnetic islands smooths the transition between low and high Hartmann number regimes, impacting plasma rotation. Further research should focus on how these magnetic islands affect plasma behaviour in the inter-regime. The scaling law may change based on the configuration of the magnetic islands or the magnetic field distribution. Exploring these aspects could offer valuable insights and lead to more precise predictions of the scaling laws in this region.

There is also potential to make the system more realistic. It can be achieved by incorporating more accurate heating techniques, current drives, and temperature effects. Furthermore, expanding the model to a three-dimensional configuration with temporal dependency would significantly enhance the accuracy of future simulations.

From a computational perspective, there is room for improvement as well. Since current simulations were performed on a CPU, transitioning to graphics processing unit (GPU)-based simulations could lead to faster computations, enabling simulations at higher Hartmann numbers. GPUs are also more efficient for parallel computations, as parallelizing the code would further accelerate calculations and allow for more complex simulations in the future. The transition to cluster simulation is also an alternative to improve computational performance.

6.5 Concluding remarks

Plasma rotation can stabilize the plasma and improve its confinement properties, making it a key area of research in magnetic confinement fusion. Plasma rotation can be an answer in trying to avoid or quench instabilities. Instabilities are one of the most problematic issues that can disrupt the plasma and prevent the sustained fusion reactions needed for a viable power plant. Magnetic confinement is still a desirable and unachieved goal. The quest for nuclear fusion as a clean and sustainable energy source has been ongoing for decades. The potential benefits of fusion energy are immense, offering a virtually limitless supply of clean, safe, and abundant energy. However, achieving controlled nuclear fusion remains a significant scientific and engineering challenge. The complexity of the plasma physics involved, the high temperatures and pressures required, and the need to sustain fusion reactions over long periods are some obstacles that must be overcome.

The results of this work can inform the design and operation of future fusion devices, helping to bring us one step closer to achieving controlled nuclear fusion as a clean and sustainable energy source.

Bibliography

Bondeson, A. and Ward, D. J. (1994). Stabilization of external modes in tokamaks by resistive walls and plasma rotation. *Physical Review Letters*, 72(17):2709–2712, DOI: 10.1103/PhysRevLett.72.2709.

Kamp, L. P. and Montgomery, D. C. (2003). Toroidal flows in resistive magnetohydrodynamic steady states. *Physics of Plasmas*, 10:157–167, DOI: 10.1063/1.1524629.

Kamp, L. P. and Montgomery, D. C. (2004). Toroidal steady states in visco-resistive magnetohydrodynamics. *Journal of Plasma Physics*, 70(2):113–142, DOI: 10.1017/S0022377803002629.

Kamp, L. P., Montgomery, D. C., and Bates, J. W. (1998). Toroidal flows in resistive magnetohydrodynamic steady states. *Physics of Fluids*, 10(7):1757–1766, ISSN: 1070-6631, DOI: 10.1063/1.869692.

Sabbagh, S. A., Bell, R. E., Menard, J. E., Gates, D. A., Sontag, A. C., Bialek, J. M., LeBlanc, B. P., Levinton, F. M., Tritz, K., and Yuh, H. (2006). Active stabilization of the resistive-wall mode in high-beta, low-rotation plasmas. *Physical Review Letters*, 97(4):045004, DOI: 10.1103/PhysRevLett.97.045004.

Takechi, M., Matsunaga, G., Aiba, N., Fujita, T., Ozeki, T., Koide, Y., Sakamoto, Y., Kurita, G., Isayama, A., and Kamada, Y. (2007). Identification of a low

plasma-rotation threshold for stabilization of the resistive-wall mode. *Physical Review Letters*, 98(5):055002, DOI: 10.1103/PhysRevLett.98.055002.

Appendices

Appendix A

Neumann boundary conditions in FreeFem++

To correctly enforce Neumann boundary conditions on the boundary of the domain using FreeFem++, we consider the following methods and corresponding boundary conditions:

A. In FreeFem++, a prebuilt option exists to impose Neumann boundary conditions. If we consider the simple Neumann condition $\partial_n u_4 = 0$, it implies removing the constraint of w_4 being equal to zero (which is a derivative of u_4):

```
+on(2, w1=0, w2=0, w3=0, w5=0);
```

B. However, if we have a more complex boundary condition, such as the free-slip boundary condition $\partial_n(u_4/r^2) = 0$, we can include the following lines in the numerical solver:

```
+ int1d(Th,2)(v4*((dx(w4)-2*(x-r0)*w4/x/r0)*N.x+dy(w4)*N.y));
+ int1d(Th,2)(v4*((dx(u4)-2*(x-r0)*u4/x/r0)*N.x+dy(u4)*N.y));
+ on(2, w1=0, w2=0, w3=0, w5=0);
```

In the above expressions, v_4 is the test function, N_x and N_y represent the components of the normal vector $\mathbf{n}$.

C. For the final boundary condition, $\partial_n(u_4/x) = \partial_n(u_2/x) = 0$, we can follow a similar approach as in **B** by including additional lines in the solver:

```
+ int1d(Th,2)(v2*((dx(w2)-w2/x)*N.x+dy(w2)*N.y));
+ int1d(Th,2)(v2*((dx(u2)-u2/x)*N.x+dy(u2)*N.y));
+ int1d(Th,2)(v4*((dx(w4)-w4/x)*N.x+dy(w4)*N.y));
+ int1d(Th,2)(v4*((dx(u4)-u4/x)*N.x+dy(u4)*N.y));
+ on(2, w1=0, w3=0, w5=0);
```

This condition indicates that the normal derivative of the toroidal velocity and vorticity must be zero at the boundary. The other option is quite direct, but this approach may be more accurate. To apply this, we need to substitute $\tilde{u}_4 = u_4/x = v_\varphi$ directly and $\tilde{u}_2 = u_2/x = \omega_\varphi$ into the system of equations, which now reads as follows:

$$\triangle^* u_1 = -x\tilde{u}_2, \tag{A.1}$$

$$\hat{\nu}\triangle^* \tilde{u}_2 = \frac{1}{x^3}\frac{\partial}{\partial y}(u_3^2) - \frac{1}{x}\frac{\partial}{\partial y}(\tilde{u}_4^2) + \frac{1}{x^2}\{u_6, u_5\} + \frac{1}{x}\{u_1, \tilde{u}_2\} \tag{A.2}$$

$$+ \frac{\tilde{u}_2}{x^2}\frac{\partial u_1}{\partial y} - \frac{2u_6}{x^3}\frac{\partial u_5}{\partial y} + \hat{\nu}\frac{\tilde{u}_2}{x^2} - \hat{\nu}\frac{2}{x}\frac{\partial \tilde{u}_2}{\partial x}, \tag{A.3}$$

$$\hat{\eta}\triangle^* u_3 = \frac{1}{x}\{u_1, u_3\} + \{\tilde{u}_4, u_5\} + \frac{2u_3}{x^2}\frac{\partial u_1}{\partial y} - \frac{\tilde{u}_4}{x}\frac{\partial u_5}{\partial y}, \tag{A.4}$$

$$\hat{\nu}\triangle^* \tilde{u}_4 = \frac{1}{x}\{u_1, \tilde{u}_4\} + \frac{1}{x^2}\{u_3, u_5\} - \frac{\tilde{u}_4}{x^2}\frac{\partial u_1}{\partial y} + \hat{\nu}\frac{\tilde{u}_4}{x^2} - \hat{\nu}\frac{2}{x}\frac{\partial \tilde{u}_4}{\partial x}, \tag{A.5}$$

$$\triangle^* u_5 = -u_6, \tag{A.6}$$

with

$$\hat{\eta}u_6 = \hat{E}_0 + \frac{1}{x}\{u_5, u_1\},$$

and then apply the Neumann boundary condition $\partial_n \tilde{u}_4 = \partial_n \tilde{u}_2 = 0$, so that we simply remove the constraint of $\tilde{u}_4$ and $\tilde{u}_2$ being equal to zero as in **A**.

Interestingly, imposing the boundary condition $\partial_n(u_4/x) = \partial_n(u_2/x) = 0$ using method **B** and method **C** yields slightly different results. This discrepancy can be observed in the comparison shown in the Figure below.

I believe that method **C** is more accurate, although it requires more derivation beforehand. On the other hand, method **B** is more straightforward and easier to implement, but it generally demands more computational time. The results presented in the thesis are obtained using method **C**.

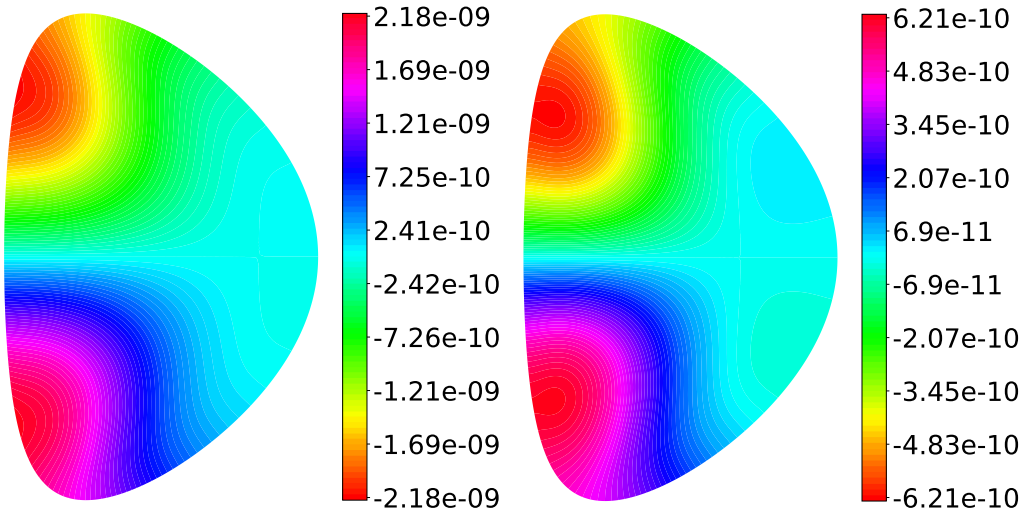

Figure A.1: Toroidal velocity field computed for $H = 10$ with boundary condition $\partial_n(u_4/x) = \partial_n(u_2/x) = 0$ using method **B** (on the left) and method **C** (on the right).

Appendix B

Detailed derivation of pressure

To introduce the pressure of the system, we need to consider the Navier-Stokes equation (the force balance equation):

$$\hat{\omega} \times \hat{\mathbf{v}} = -\hat{\nabla}\left(\frac{p^*}{b_0^2 \rho_m}\right) + \hat{\jmath} \times \hat{\mathbf{b}} + \hat{\nu}\hat{\nabla}^2\hat{\mathbf{v}}$$

with

$$p^* = p + \rho_m \frac{v^2}{2}$$

Previously, we dropped the pressure in deriving the system of equations by taking the curl and the toroidal part of the force balance equation. Now, to get the pressure of the system, we take the divergence $\hat{\nabla}\cdot$ of the Navier-Stokes equation.

$$\hat{\nabla} \cdot \hat{\nabla}\left(\frac{p^*}{b_0^2 \rho_m}\right) = \hat{\nabla} \cdot \left[-\hat{\omega} \times \hat{\mathbf{v}} + \hat{\jmath} \times \hat{\mathbf{b}} + \hat{\nu}\hat{\nabla}^2\hat{\mathbf{v}}\right]$$

Let us consider normalized pressure $\hat{p}$ to be:

$$\hat{p} = \frac{p^*}{b_0^2 \rho_m}$$

So the left-hand-side (LHS) will be a Laplacian of pressure $\triangle\hat{p}$.
The first term of the right-hand-side (RHS) would be

$$\begin{aligned}
\hat{\nabla} \cdot (\hat{\omega} \times \hat{\mathbf{v}}) &= \hat{\mathbf{v}} \cdot (\hat{\nabla} \times \hat{\omega}) - \hat{\omega} \cdot (\hat{\nabla} \times \hat{\mathbf{v}}) = \\
&= \hat{\mathbf{v}} \cdot (\hat{\nabla} \times (\hat{\nabla} \times \hat{\mathbf{v}})) - \hat{\omega} \cdot \hat{\omega} = \\
&= \hat{\mathbf{v}} \cdot (\hat{\nabla}(\hat{\nabla} \cdot \hat{\mathbf{v}}) - \hat{\nabla}^{\mathbf{2}}\hat{\mathbf{v}}) - \hat{\omega}^{\mathbf{2}} = \wr \hat{\nabla} \cdot \hat{v} = 0 \wr \\
&= -\hat{\mathbf{v}} \cdot \hat{\nabla}^{\mathbf{2}}\hat{\mathbf{v}} - \hat{\omega}^{\mathbf{2}}
\end{aligned}$$

We can treat the $\hat{\jmath} \times \hat{\mathbf{b}}$ term on the same manner:

$$\hat{\nabla} \cdot (\hat{\jmath} \times \hat{\mathbf{b}}) \quad = \quad -\hat{\mathbf{b}} \cdot \hat{\nabla}^{\mathbf{2}} \hat{\mathbf{b}} - \hat{\jmath}^{\mathbf{2}}$$

And finally, the last term is

$$\hat{\nu}\hat{\nabla}^2\hat{\mathbf{v}} = -\hat{\nu}(\hat{\nabla} \times (\hat{\nabla} \times \hat{\mathbf{v}})) \Rightarrow \hat{\nabla}\cdot(\hat{\nu}\hat{\nabla}^2\hat{\mathbf{v}}) = 0$$

Therefore, the Poisson's equation for pressure now reads:

$$\triangle\hat{p} = \hat{\mathbf{v}} \cdot \hat{\nabla}^{\mathbf{2}} \hat{\mathbf{v}} + \hat{\omega}^{\mathbf{2}} - \hat{\mathbf{b}} \cdot \hat{\nabla}^2 \hat{\mathbf{b}} - \hat{\jmath}^2$$

Dimensionless vorticity reads

$$\hat{\omega} = \frac{1}{x}\hat{\nabla}\left(x\hat{v}_\varphi\right) \times \mathbf{i}_\varphi - \frac{1}{x}\left(\hat{\triangle}^*\hat{\psi}\right)\mathbf{i}_\varphi$$

So that

$$\hat{\omega}^2 = \left[\frac{1}{x}\hat{\nabla}\left(x\hat{v}_\varphi\right) \times \mathbf{i}_\varphi - \frac{1}{x}\left(\hat{\triangle}^*\hat{\psi}\right)\mathbf{i}_\varphi\right] \cdot \left[\frac{1}{x}\hat{\nabla}\left(x\hat{v}_\varphi\right) \times \mathbf{i}_\varphi - \frac{1}{x}\left(\hat{\triangle}^*\hat{\psi}\right)\mathbf{i}_\varphi\right] =$$

$$= \left(\frac{\hat{\nabla}\left(x\hat{v}_\varphi\right)}{x}\right)^2 + \left(\frac{\left(\hat{\triangle}^*\hat{\psi}\right)}{x}\right)^2 = -\frac{u_2}{x^2}\triangle^* u_1 + \frac{1}{x^2}\frac{\partial u_4}{\partial x}\frac{\partial u_4}{\partial x} + \frac{1}{x^2}\frac{\partial u_4}{\partial y}\frac{\partial u_4}{\partial y}$$

Dimensionless current reads

$$\hat{\jmath} = \frac{1}{x}\hat{\nabla}\left(x\hat{b}_\varphi\right) \times \mathbf{i}_\varphi - \frac{1}{x}\left(\hat{\triangle}^*\hat{\chi}\right)\mathbf{i}_\varphi$$

Similarly, the fourth term now

$$-\hat{\jmath}^2 = -\left[\frac{1}{x}\hat{\nabla}\left(x\hat{b}_\varphi\right) \times \mathbf{i}_\varphi - \frac{1}{x}\left(\hat{\triangle}^*\hat{\chi}\right)\mathbf{i}_\varphi\right] \cdot \left[\frac{1}{x}\hat{\nabla}\left(x\hat{b}_\varphi\right) \times \mathbf{i}_\varphi - \frac{1}{x}\left(\hat{\triangle}^*\hat{\chi}\right)\mathbf{i}_\varphi\right] =$$

$$= -\left(\frac{\hat{\nabla}\left(x\hat{b}_\varphi\right)}{x}\right)^2 - \left(\frac{\left(\hat{\triangle}^*\hat{\chi}\right)}{x}\right)^2 = -\frac{1}{x^2}\frac{\partial u_3}{\partial x}\frac{\partial u_3}{\partial x} - \frac{1}{x^2}\frac{\partial u_3}{\partial y}\frac{\partial u_3}{\partial y} + \frac{u_6}{x^2}\triangle^* u_5$$

Finally, let us look at the term $-\hat{\mathbf{b}} \cdot \hat{\nabla}^{\mathbf{2}}\hat{\mathbf{b}}$:

$$-\hat{\mathbf{b}} \cdot \hat{\nabla}^{\mathbf{2}}\hat{\mathbf{b}} = \hat{\mathbf{b}} \cdot (\hat{\nabla} \times \hat{\jmath})$$

$$\hat{\nabla} \times \hat{\jmath} = -\frac{1}{x}\hat{\triangle}^*\left(x\hat{b}_\varphi\right)\mathbf{i}_\varphi - \frac{1}{x}\hat{\nabla}\left(\hat{\triangle}^*\hat{\chi}\right) \times \mathbf{i}_\varphi$$

Therefore, with

$$\hat{\mathbf{b}} = \frac{1}{x}\hat{\nabla}\hat{\chi} \times \mathbf{i}_\varphi + \left(\frac{1}{x} + \hat{b}_\varphi\right)\mathbf{i}_\varphi,$$

The third term of the RHS

$$\hat{\mathbf{b}} \cdot (\hat{\nabla} \times \hat{j}) = -\left(\frac{1}{x} + \hat{b}_\varphi\right) \frac{1}{x} \hat{\triangle}^* \left(x \hat{b}_\varphi\right) - \frac{1}{x} \hat{\nabla} \hat{\chi} \cdot \frac{1}{x} \hat{\nabla} \left(\hat{\triangle}^* \hat{\chi}\right) =$$

$$= -\frac{u_3}{x^2} \triangle^* u_3 + \frac{1}{x^2} \frac{\partial u_5}{\partial x} \frac{\partial u_6}{\partial x} + \frac{1}{x^2} \frac{\partial u_5}{\partial y} \frac{\partial u_6}{\partial y}$$

Similarly

$$\hat{\mathbf{v}} \cdot \hat{\nabla}^{\mathbf{2}} \hat{\mathbf{v}} = -\hat{\mathbf{v}} \cdot (\hat{\nabla} \times \hat{\omega})$$

$$\hat{\nabla} \times \hat{\omega} = -\frac{1}{x} \hat{\triangle}^* \left(x \hat{v}_\varphi\right) \mathbf{i}_\varphi - \frac{1}{x} \hat{\nabla} \left(\hat{\triangle}^* \hat{\psi}\right) \times \mathbf{i}_\varphi$$

Therefore, with

$$\hat{\mathbf{v}} = \frac{1}{x} \hat{\nabla} \hat{\psi} \times \mathbf{i}_\varphi + \hat{v}_\varphi \mathbf{i}_\varphi,$$

And the last term of the RHS is

$$-\hat{\mathbf{v}} \cdot (\hat{\nabla} \times \hat{\omega}) = \hat{v}_\varphi \frac{1}{x} \hat{\triangle}^* \left(x \hat{v}_\varphi\right) + \frac{1}{x} \hat{\nabla} \hat{\psi} \cdot \frac{1}{x} \hat{\nabla} \left(\hat{\triangle}^* \hat{\psi}\right) =$$

$$= \frac{u_4}{x^2} \triangle^* u_4 - \frac{1}{x^2} \frac{\partial u_2}{\partial x} \frac{\partial u_1}{\partial x} - \frac{1}{x^2} \frac{\partial u_2}{\partial y} \frac{\partial u_1}{\partial y}$$

The full Poisson's equation for pressure finally reads:

$$\begin{aligned}
\triangle \hat{p} = {} & \hat{v}_\varphi \frac{1}{x} \hat{\triangle}^* \left(x \hat{v}_\varphi\right) + \frac{1}{x} \hat{\nabla} \hat{\psi} \cdot \frac{1}{x} \hat{\nabla} \left(\hat{\triangle}^* \hat{\psi}\right) \\
& - \left(\frac{1}{x} + \hat{b}_\varphi\right) \frac{1}{x} \hat{\triangle}^* \left(x \hat{b}_\varphi\right) - \frac{1}{x} \hat{\nabla} \hat{\chi} \cdot \frac{1}{x} \hat{\nabla} \left(\hat{\triangle}^* \hat{\chi}\right) \\
& + \left(\frac{\hat{\nabla} \left(x \hat{v}_\varphi\right)}{x}\right)^2 + \left(\frac{\left(\hat{\triangle}^* \hat{\psi}\right)}{x}\right)^2 \\
& - \left(\frac{\hat{\nabla} \left(x \hat{b}_\varphi\right)}{x}\right)^2 - \left(\frac{\left(\hat{\triangle}^* \hat{\chi}\right)}{x}\right)^2
\end{aligned}$$

We now have all parts of Poisson's equation written as magnetic flux function χ and velocity stream function ψ. The final step is to go to the dimensionless variables $u_1, u_2 ... u_6$.

Let us introduce a new variable u_0, which is

$$u_0 = \hat{p} = \frac{p}{b_0^2 \rho_m}$$

So the Poisson's equation for the pressure of the system now reads:

$$\begin{aligned}\triangle u_0 = &\frac{u_4}{x^2}\triangle^* u_4 - \frac{1}{x^2}\frac{\partial u_2}{\partial x}\frac{\partial u_1}{\partial x} - \frac{1}{x^2}\frac{\partial u_2}{\partial y}\frac{\partial u_1}{\partial y}\\ &- \frac{u_2}{x^2}\triangle^* u_1 + \frac{1}{x^2}\frac{\partial u_4}{\partial x}\frac{\partial u_4}{\partial x} + \frac{1}{x^2}\frac{\partial u_4}{\partial y}\frac{\partial u_4}{\partial y}\\ &- \frac{u_3}{x^2}\triangle^* u_3 + \frac{1}{x^2}\frac{\partial u_5}{\partial x}\frac{\partial u_6}{\partial x} + \frac{1}{x^2}\frac{\partial u_5}{\partial y}\frac{\partial u_6}{\partial y}\\ &+ \frac{u_6}{x^2}\triangle^* u_5 - \frac{1}{x^2}\frac{\partial u_3}{\partial x}\frac{\partial u_3}{\partial x} - \frac{1}{x^2}\frac{\partial u_3}{\partial y}\frac{\partial u_3}{\partial y}\end{aligned}$$

where

$$\triangle = \frac{\partial^2}{\partial x^2} + \frac{1}{x}\frac{\partial}{\partial x} + \frac{\partial^2}{\partial y^2}.$$

Boundary conditions

According to [Kress and Montgomery, 2000], the standard component of ∇p is enough to determine p through the Neumann boundary condition. It means that we need once again to get back to the Navier-Stokes equation:

$$\hat{\omega} \times \hat{\mathbf{v}} = -\hat{\nabla}\hat{p} + \hat{\jmath} \times \hat{\mathbf{b}} + \hat{\nu}\hat{\nabla}^2\hat{\mathbf{v}}$$

Now, to get ∇p, we are interested in the poloidal part of the equation:

$$\hat{\nabla}\hat{p} = -\hat{\omega} \times \hat{\mathbf{v}} + \hat{\jmath} \times \hat{\mathbf{b}} + \hat{\nu}\hat{\nabla}^2\hat{\mathbf{v}}$$

Let us start from $\hat{\jmath} \times \hat{\mathbf{b}}$ term:

$$\hat{\jmath} \times \hat{\mathbf{b}} = \left[\frac{1}{x}\hat{\nabla}\left(x\hat{b}_\varphi\right) \times \mathbf{i}_\varphi - \frac{1}{x}\left(\hat{\triangle}^*\hat{\chi}\right)\mathbf{i}_\varphi\right] \cdot \left[\frac{1}{x}\hat{\nabla}\hat{\chi} \times \mathbf{i}_\varphi + \left(\frac{1}{x} + \hat{b}_\varphi\right)\mathbf{i}_\varphi\right] =$$

$$= -\left(\frac{1}{x} + \hat{b}_\varphi\right)\frac{1}{x}\hat{\nabla}\left(x\hat{b}_\varphi\right) - \frac{1}{x}\hat{\nabla}\hat{\chi}\frac{1}{x}\left(\hat{\triangle}^*\hat{\chi}\right)$$

Similarly

$$\hat{\omega} \times \hat{\mathbf{v}} = -\hat{v}_\varphi\frac{1}{x}\hat{\nabla}\left(x\hat{v}_\varphi\right) - \frac{1}{x}\hat{\nabla}\hat{\psi}\frac{1}{x}\left(\hat{\triangle}^*\hat{\psi}\right)$$

Finally, we can combine all terms already in the new variables:

$$\hat{\nabla}u_0 = \underbrace{-\frac{u_3}{x^2}\hat{\nabla}u_3 + \frac{u_6}{x^2}\hat{\nabla}u_5}_{\hat{\jmath} \times \hat{\mathbf{b}}} + \underbrace{\frac{u_4}{x^2}\hat{\nabla}u_4 - \frac{u_2}{x^2}\hat{\nabla}u_1}_{\hat{\omega} \times \hat{\mathbf{v}}}$$

Neumann boundary condition for the pressure of the system reads as:

$$\frac{\partial p}{\partial n} = \frac{\partial p}{\partial x}N.x + \frac{\partial p}{\partial y}N.y = h$$

$$\frac{\partial p}{\partial x} = -\frac{u_3}{x^2}\frac{\partial u_3}{\partial x} + \frac{u_6}{x^2}\frac{\partial u_5}{\partial x} - \frac{u_2}{x^2}\frac{\partial u_1}{\partial x} + \frac{u_4}{x^2}\frac{\partial u_4}{\partial x}$$
$$\frac{\partial p}{\partial y} = -\frac{u_3}{x^2}\frac{\partial u_3}{\partial y} + \frac{u_6}{x^2}\frac{\partial u_5}{\partial y} - \frac{u_2}{x^2}\frac{\partial u_1}{\partial y} + \frac{u_4}{x^2}\frac{\partial u_4}{\partial y}$$

Weak formulation

Finally, we propose the weak formulations of Poisson's equation for the system's pressure. Let's put v_0 as a regular test function, null on $\partial\Omega$. Then the Poisson's equation reads:

$$\begin{aligned}
&\int_\Omega \left(\frac{\partial u_0}{\partial x}\frac{\partial v_0}{\partial x} + \frac{\partial u_0}{\partial y}\frac{\partial v_0}{\partial y}\right) dw - \int_\Omega \frac{1}{x}\frac{\partial u_0}{\partial x} v_0\, dw + \int_\Omega \frac{u_2^2}{x^2} v_0\, dw \\
&+ \int_\Omega \left(\frac{\partial u_4}{\partial x}\frac{\partial u_4}{\partial x} + \frac{\partial u_4}{\partial y}\frac{\partial u_4}{\partial y}\right) \frac{v_0}{x^2}\, dw + \int_\Omega \left(\frac{\partial u_3}{\partial x}\frac{\partial v_0}{\partial x} + \frac{\partial u_3}{\partial y}\frac{\partial v_0}{\partial y}\right) \frac{u_3}{x^2}\, dw \\
&+ \int_\Omega \frac{u_3}{x^3}\frac{\partial u_3}{\partial x} v_0\, dw + \int_\Omega \left(\frac{\partial u_5}{\partial x}\frac{\partial u_6}{\partial x} + \frac{\partial u_5}{\partial y}\frac{\partial u_6}{\partial y}\right) \frac{v_0}{x^2}\, dw \\
&- \int_\Omega \left(\frac{\partial u_3}{\partial x}\frac{\partial u_3}{\partial x} + \frac{\partial u_3}{\partial y}\frac{\partial u_3}{\partial y}\right) \frac{v_0}{x^2}\, dw - \int_\Omega \frac{u_6^2}{x^2} v_0\, dw + \int_\Gamma h v_0\, d\gamma = 0
\end{aligned}$$

With this equation, we can compute the system's pressure by correctly enforcing the Neumann boundary conditions. In the thesis, we compute pressure profiles by assuming the pressure to be zero at the border. This derivation presents more realistic pressure calculations.

Appendix C

Velocity scaling law in the limit $H \ll 1$

The basic set of equations consists of the Navier-Stokes equation, the Ohm's law, and the Maxwell equations. The dimensionless form of these equations reads as follows:

$$
\begin{aligned}
&(\boldsymbol{v} \cdot \nabla)\boldsymbol{v} = \boldsymbol{J} \times \boldsymbol{B} - \nabla p + \nu \nabla^2 \boldsymbol{v} \\
&\boldsymbol{E} + \boldsymbol{v} \times \boldsymbol{B} = \eta \boldsymbol{J} \\
&\nabla \times \boldsymbol{B} = \boldsymbol{J} \\
&\nabla \times \boldsymbol{E} = 0
\end{aligned}
$$

Here, p is the pressure, ν is the kinematic viscosity, and η is the reciprocal of the electrical conductivity. In the dimensionless units used, ν is the reciprocal of the viscous Lundquist number, M and η is the reciprocal of the resistive Lundquist number S.

The first regime in the limit of small Hartmann numbers $H \ll 1$ could be derived analytically with the $\nu \to \infty$ approximation.

$$\nu \to \infty => M \to 0$$

Replacing the fluid velocity $\boldsymbol{v}$ by $M\boldsymbol{u}$ gives:

$$
\begin{aligned}
\boldsymbol{J} \times \boldsymbol{B} - \nabla p + \nabla^2 \boldsymbol{u} = M^2 (\boldsymbol{u} \cdot \nabla)\boldsymbol{u} \approx 0 \\
\boldsymbol{J} - S\boldsymbol{E} = H^2 (\boldsymbol{u} \times \boldsymbol{B}) \approx 0
\end{aligned}
$$

We can neglect the smallest terms so that the set of equations in the first part (approximation $\nu \to \infty$) takes the following form:

$$\begin{aligned} \boldsymbol{J} \times \boldsymbol{B} - \nabla p + \nabla^2 \boldsymbol{u} &= 0 \\ \boldsymbol{J} - S\boldsymbol{E} &= 0 \\ \nabla \times \boldsymbol{B} &= \boldsymbol{J} \\ \nabla \times \boldsymbol{E} &= 0 \end{aligned}$$

In our system of equations in variables $u_1, u_2 ... u_6$, this leads to the following system:

$$\triangle^* u_1 = -u_2, \tag{C.1}$$

$$\nu \triangle^* u_2 = -\frac{E_0}{\eta} \frac{2}{x^2} \frac{\partial u_5}{\partial y}, \tag{C.2}$$

$$\triangle^* u_5 = -\frac{E_0}{\eta}. \tag{C.3}$$

$$\tag{C.4}$$

In this approximation, we neglect the toroidal flow, meaning the variable u_4 is dropped, as it is smaller than the poloidal flow variables u_1 and u_2 by a factor of H^2. Similarly, the toroidal magnetic field dropped since $u_3 - 1$ is H^2 smaller than the poloidal magnetic field u_5. The $\mathbf{v} \times \mathbf{B}$ term in Ohm's law is also neglected, implying that u_6 is dropped as it is H^2 smaller than the driving term E_0/η.

From this approximation, we can derive the scaling laws for the plasma velocities in the limit $H \ll 1$. The poloidal velocity scales as H^2, while the toroidal velocity, being two orders smaller, scales as H^4.

ECOLE
DOCTORALE

Titre : Optimisation de la vitesse du plasma pour l'amélioration du confinement des tokamaks

Mots clés : Simulations numériques, fusion thermonucléaire par confinement magnétique, MHD, physique des plasmas, tokamaks, modélisation

Résumé : Il est essentiel pour rendre performants les futurs réacteurs à fusion par confinement magnétique de maximiser le confinement du plasma. Jouer sur la vitesse du plasma peut être un moyen de stabiliser d'éventuelles instabilités et de contrôler la turbulence avec des effets très bénéfiques sur les performances fusion. Il est donc crucial de comprendre comment on peut mettre en rotation un plasma de tokamak. Idéalement on souhaite que le tokamak, en tant que réacteur à fusion, travaille en régime permanent. Il est donc raisonnable de déterminer les états stationnaires d'un plasma de tokamak en toute généralité, sans imposer la nullité du champ de vitesse du plasma. Dans le cadre de la magnétohydrodynamique (MHD) visco-résistive, cela revient à conserver notamment le terme non-linéaire (v.grad)v dans l'équation stationnaire de Navier-Stokes. En utilisant FreeFem++, nous avons déterminé numériquement les états stationnaires axisymmétriques d'un plasma de tokamak dans des géométries réalistes de type JET, en appliquant un modèle magnétohydrodynamique (MHD) visco-résistif avec une résistivité η et une viscosité ν constantes. On montre que la vitesse moyenne quadratique du plasma se comporte comme $\eta f(H)$ tant que le terme inertiel reste négligeable, où H représente le nombre de Hartmann $H \equiv (\eta\nu)^{-1/2}$, et que $f(H)$ présente des comportements de loi de puissance dans les limites $H \ll 1$ et $H \gg 1$. Dans cette limite, nous établissons que $f(H)$ s'échelonne comme $H^{1/4}$, ce qui est cohérent avec les résultats numériques. De plus, nous avons établi une équation de Poisson pour le profil de pression. Il a été démontré que l'hypothèse simplificatrice d'une densité de courant toroïdale purement inductive ne génère pas des niveaux de pression réalistes. Pour remédier à cela, des entraînements de courant non inductifs supplémentaires, similaires à l'injection de faisceaux neutres, ont été introduits. Les simulations numériques validant ce modèle montrent des améliorations du profil de pression. Enfin, l'étude des profils de densité de courant fixes révèle un nouveau régime, où les vitesses toroïdales et poloïdales s'échelonnent comme H^2.

Title : Plasma speed optimization for improved tokamak plasma confinement

Keywords : MHD, plasma physics, tokamaks, numerical simulations, magnetic confinement fusion, modelling

Abstract : Maximizing plasma confinement is essential to the performance of future magnetic fusion reactors. Playing with plasma speed can be a way to stabilize possible instabilities and control turbulence with a very beneficial impact on fusion yield. It is, therefore, essential to understand how a tokamak plasma can be rotated. Ideally, the tokamak should work in a stationary state as a fusion reactor. It is, therefore, reasonable to determine the steady states of a tokamak plasma in full generality without imposing the nullity of the plasma velocity field. In the visco-resistive magnetohydrodynamics (MHD) framework, this amounts in particular to retaining the non-linear term (v.grad)v in the stationary Navier-Stokes equation. Using the FreeFem++ open-source software for solving partial differential equations using the finite element method, we numerically determined the axisymmetric stationary states of a tokamak plasma in realistic JET. This thesis shows that the plasma velocity root-mean-square behaves as $\eta f(H)$ as long as the inertial term remains negligible, where H stands for the Hartmann number $H \equiv (\eta\nu)^{-1/2}$, and that $f(H)$ exhibits power-law behaviours in the limits $H \ll 1$ and $H \gg 1$. In the latter limit, we establish that $f(H)$ scales as $H^{1/4}$, which is consistent with numerical results. Additionally, this work establishes Poisson's equation governing the pressure profile. It is shown that the simplifying assumption of a toroidal current density component arising solely from Ohm's law in response to a time-independent, curl-free toroidal electric field fails to produce realistic pressure levels. We introduce additional non-inductive current drives, comparable to those from neutral beam injection, modeled as modifications to the toroidal current. The new model is validated using numerical simulations, showing significant pressure profile improvements. For the examples considered, the effect of these current drives on the velocity profiles is moderate except in the case where the drives induce some reversals in the total toroidal current density, producing non-nested flux surfaces with internal separatrices. Finally, the effect of fixed current density profiles is examined, revealing a new second regime, where toroidal and poloidal velocities scale with Hartmann number as H^2.

Institut Polytechnique de Paris
91120 Palaiseau, France